RICE UNIVERSITY

Modeling the Plasma Convection in Saturn's Inner Magnetosphere

by

Xin Liu

A THESIS SUBMITTED
IN PARTIAL FULFILLMENT OF THE
REQUIREMENTS FOR THE DEGREE

Doctor of Philosophy

APPROVED, THESIS COMMITTEE

Thomas W. Hill, Chair
Professor,
Physics and Astronomy Department

Frank R. Toffoletto
Professor,
Physics and Astronomy Department

Adrian Lenardic
Professor,
Department of Earth Science

HOUSTON, TEXAS
March 2013

ABSTRACT

Modeling the Plasma Convection in Saturn's Inner Magnetosphere

by

Xin Liu

Saturn's magnetosphere is unique in the solar system. The rotation-driven convection consists of alternating channels of cool plasma from an interior source moving outward and hot plasma from outside moving inward, making Saturn's inner magnetosphere a dynamical region. This thesis describes work on developing numerical models to simulate the plasma convection pattern in Saturn's inner magnetosphere. Chapter 2 introduces the numerical Rice Convection Model (RCM), a multi-fluid model that was originally developed for Earth's magnetosphere. We adapt it for Saturn's conditions in this thesis. In Chapter 3, we show results of initial RCM simulation runs, in which only cool plasma from the interior source is considered. We also include the Coriolis force and the pickup effect. Because the cool plasma is much denser than the hot plasma and always dominant in determining the convection pattern, it is important and necessary to investigate it first. Chapter 4 compares several cool plasma source models and determines the one that produces the best simulation results when compared to Cassini spacecraft observations. In Chapter 5, we add the finite temperature and associated plasma pressure of the cool plasma. The effect of ionospheric Pedersen conductance is also investigated. Finally in Chapter 6, we add hot plasma at the outer boundary, and simulate the V-shape signatures of the injection-dispersion events, which are considered the most definitive evidence of rotation-driven convection in Saturn's

inner magnetosphere. Our simulations conform to the observed fact that wider, slower outflow channels of cooler, denser plasma alternate with narrower, faster inflow channels of hotter, more tenuous plasma. Comparisons between simulated and observed results show great consistency.

Acknowledgments

Ph. D study could be the most special period of one's life. During the time at Rice University, the most important person to me and the first person I want to thank is my advisor Dr. Tom Hill. When I joined the space physics group, I almost started from scratch. I had so many classes to catch up, such as classes in space physics and numerical modeling. Dr. Hill is very patient, not only in answering my novice questions, but also in teaching me how to analyze and solve scientific problems. In my research, he helps me a lot in the theoretical deduction and results analysis. In the meanwhile, he lets me handle the code, with trust and patience. I have learned a lot under his supervision and I really enjoy myself during the Ph. D study.

I also want to thank Dr. Richard Wolf and Dr. Frank Toffoletto for their precious help and suggestions, specially thank Dr. Wolf for deriving the implicit method to include the Coriolis current. My appreciation also goes to Dr. Stan Sazykin and Dr. Bob Spiro for their help in the code. I also gain a lot of help from my colleagues. Jian Yang, Bei Hu, Asher Pembroke, Yi Chen, Xuhui Chen, Yang Song, Yaxue Dong, Liheng Zheng, Yifei Wan and Chunming Zhu.

At last, my sincere gratitude belongs to my parents. They have been supporting me all the time, in every decision I make and every option I choose. It takes forever to requite the endless love of parents.

Contents

List of Figures

Chapter 1

Introductions

1.1. Saturn's magnetosphere

Saturn is the sixth planet from the Sun and the second largest planet in the solar system, after Jupiter. Saturn's equatorial radius is ~60,268 km, about 9 times that of Earth. Saturn is classified as a gas giant planet. It is the least dense of all the planets. But due to its large volume, Saturn has a mass $\sim 5.68 \times 10^{26}$ kg, about 95 times that of Earth. The average distance between Saturn and the Sun is over 1.4 billion km, about 9 AU (Astronomical Unit, the average Earth-Sun distance). Saturn rotates faster than Earth, with a period ~10.8 hours. Saturn's intrinsic magnetic field nearly aligns with the spin axis, and the inner part is almost a pure dipole field.

1.1.1. Structure of Saturn's magnetosphere

Saturn is visually unique because of its prominent particulate rings. Figure 1.1 shows the planet Saturn and the visible rings. The space beyond these visible rings

appears empty. However it is not vacuum. Instead, it contains many kinds of plasma of varying compositions, densities, and temperatures. Although the densities of the plasma are very low, the structure of this region is quite complicated and the dynamics is very important. The region we are interested in is called Saturn's magnetosphere. Specifically, my research work focuses on dynamic processes in Saturn's inner magnetosphere.

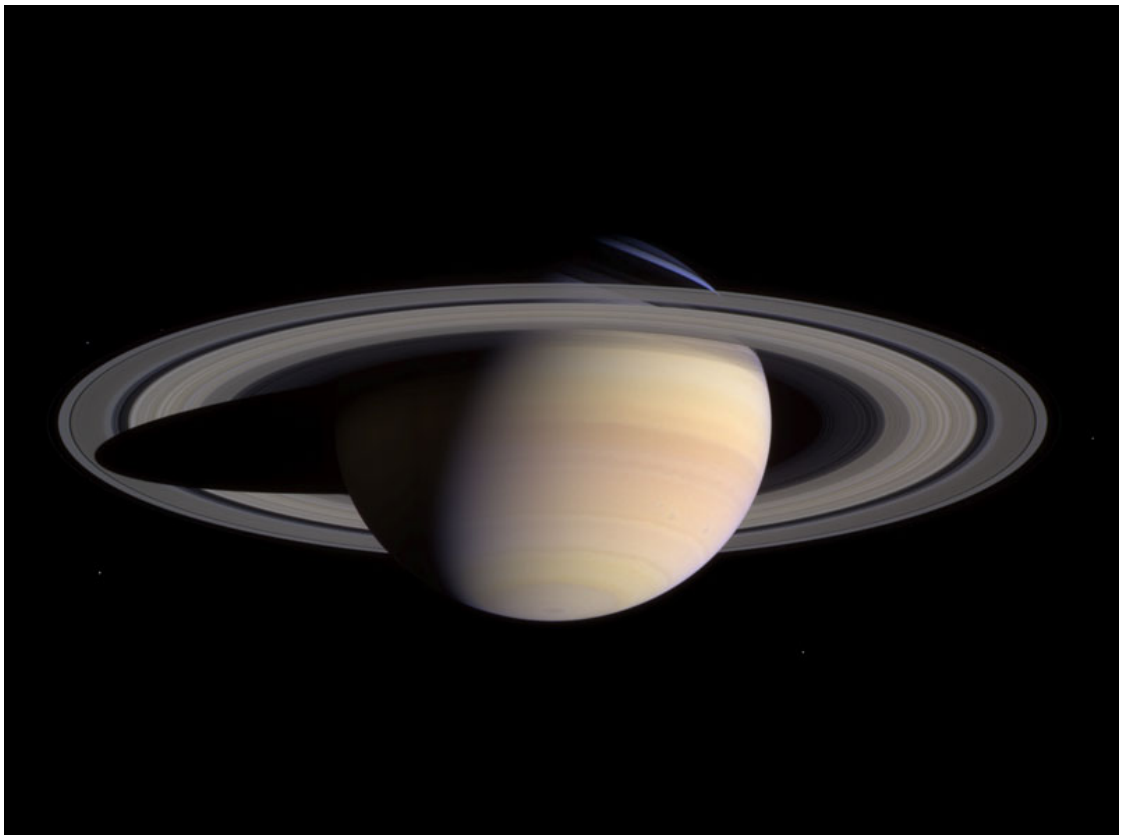

Figure 1.1 The planet Saturn, photographed by the spacecraft Cassini's Imaging Science Subsystem. [http://upload.wikimedia.org/wikipedia/commons/0/09/Saturn-cassini-March-27-2004.jpg]

Saturn's magnetosphere is the cavity created in the flow of the solar wind by the planet's intrinsic magnetic field. It is a region dominated by Saturn's magnetic field. The

solar wind is a magnetized plasma that flows supersonically outward from the Sun. When the solar wind reaches Saturn, the intrinsic magnetic field of Saturn serves as an obstacle, and a shock wave called the bow shock forms to deflect the supersonic flow. Figure 1.2 shows the basic structure of Saturn's magnetosphere, including some important regions such as the magnetosheath, magnetopause, magnetotail and inner magnetosphere.

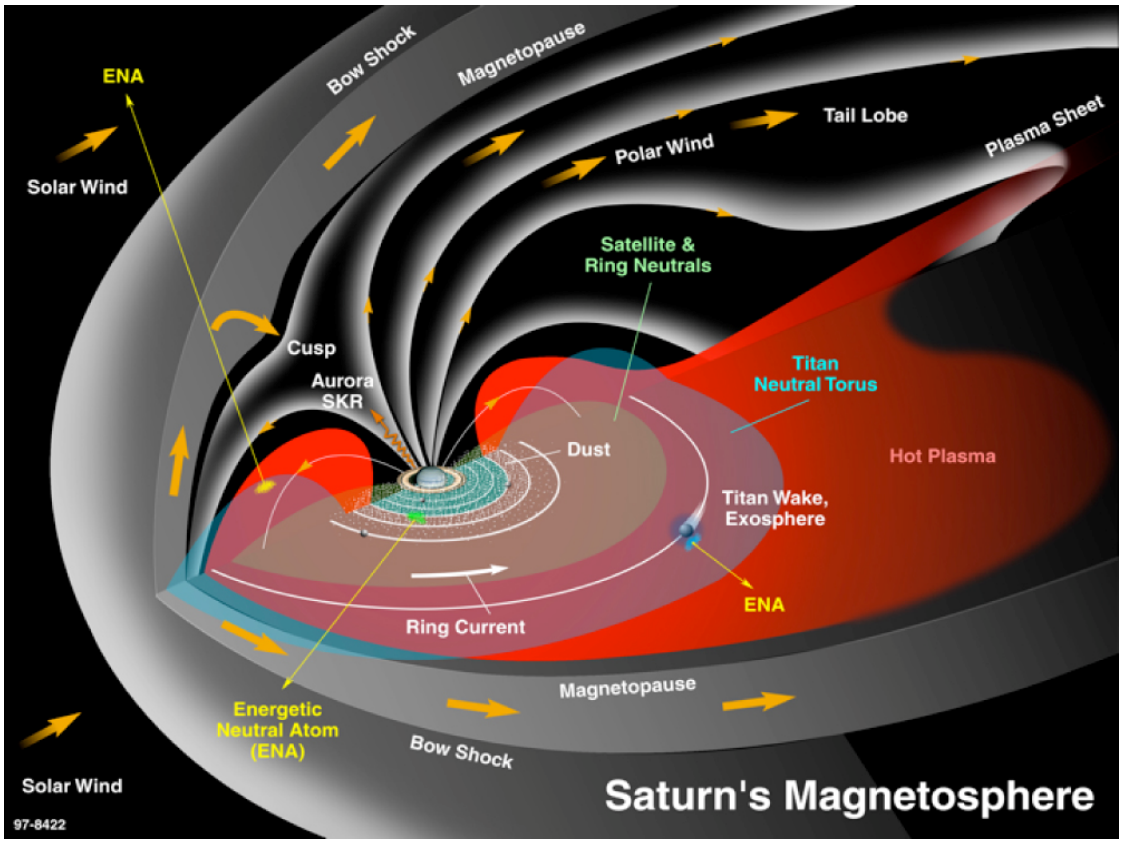

Figure 1.2 Global structure of Saturn's magnetosphere. The thick yellow arrows represent plasma flows. Gray lines with yellow arrowheads represent magnetic field lines. Adapted from NASA website. [http://opfm.jpl.nasa.gov/files/satmagno1K.jpg]

The supersonic solar-wind plasma that has passed through the bow shock slows down and becomes subsonic, and forms the day side portion of the magnetosheath. In

Figure 1.2 the magnetosheath is the region between the bow shock and the magnetopause. The magnetopause is the boundary of Saturn's magnetosphere. Its location is determined by the balance between the pressure of Saturn's intrinsic magnetic field and the pressure of the solar wind. Because the solar wind pressure is not a constant, but varies in time, the magnetopause moves inward and outward correspondingly. The region inside the magnetopause is dominated by Saturn's magnetic field, which is, however, deformed. On the day side the solar wind compresses Saturn's magnetic field, and on the night side it stretches the magnetic field to form the magnetotail. Saturn's magnetopause near the noon meridian is typically at a distance ~20 Rs (Saturn radii), while the magnetotail on the night side extends to hundreds of Rs. Our research focuses on the region called the inner magnetosphere, extending to about 12 - 15 Rs, where the magnetic field is not seriously deformed and can be treated as a pure dipole field aligned with Saturn's spin axis. In this thesis Saturn's inner magnetosphere means the region 2 Rs < L < 12 Rs, where L is the distance between the center of Saturn and the crossing point of the magnetic field line and the equatorial plane.

1.1.2. Satellites and plasma in Saturn's magnetosphere

Saturn's magnetosphere is unique in the solar system in that it contains an extensive ring system and a large collection of icy satellites. Figure 1.3 shows schematically the density distribution of E-ring particles in the meridian plane, and the locations of the major icy satellites. The most important icy satellite for its magnetospheric effects is named Enceladus, located at 3.95 Rs. Enceladus is a relatively small satellite, with a diameter of only ~505 km. (Titan, the largest satellite of Saturn, has a diameter ~5150 km and orbits at about 19.9 Rs.) In spite of its small size, Enceladus is

actively venting both neutral vapor and ice grains, both largely water. The neutral vapor is scattered through charge exchange and neutral-neutral collisions to produce a wide torus, which provides a widely distributed plasma source [*Johnson et al.*, 2006]. The complicated and extended plasma source makes plasma circulation (convection) in Saturn's inner magnetosphere a very interesting process. We will talk more about the plasma source in Chapters 3 and 4.

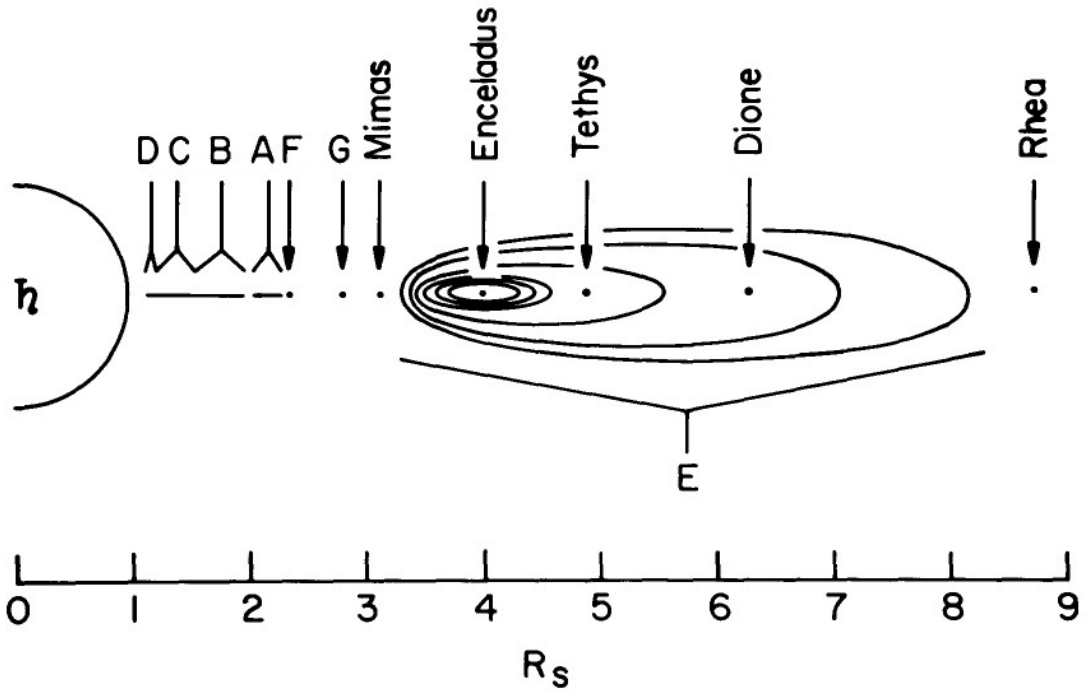

Figure 1.3 Illustration of the mass density distribution of the E-ring and the locations of the major icy satellites, from Hill [1984].

The plasma composition in Saturn's magnetosphere has been studied for years, since the beginning of the Cassini Orbiter mission at Saturn in June 2004. Based on data measured by the Cassini Plasma Spectrometer (CAPS), *Young et al.* [2005] investigated

Saturn's magnetospheric plasma properties and composition in different regions. (1) The outer magnetosphere just inside the magnetopause (~20 Rs near the noon meridian, and ~30 Rs near the dawn meridian) is dominated by hot tenuous plasma, mainly H^+. (2) The inner magnetosphere inside of ~15 Rs is dominated by cooler denser plasma that is partially corotating with Saturn, composed mainly of water-group ions W^+ (including O^+, OH^+, H_2O^+, and H_3O^+). (3) The layer of plasma over the A and B rings (~2 Rs) is made up of O^+ and O_2^+. Because this thesis is limited to the inner magnetosphere 2 – 12 Rs, we focus on the water-group ions W^+, which dominate this region.

1.2. Dynamics in Saturn's magnetosphere

The dynamics of planetary magnetospheres can be divided into two types driven by different effects: solar-wind-driven convection and rotation-driven convection. It has been confirmed that the former mechanism dominates Earth's magnetosphere, while the later mechanism dominates Jupiter's and Saturn's magnetospheres. Earth's magnetosphere was the first to be observed and remains the most studied. It is appropriate to introduce both convection mechanisms.

1.2.1. Solar-wind-driven convection

Earth's magnetosphere has a cavity shape similar to that of Saturn. The direction of its magnetic dipole moment is opposite to that of Saturn: the north pole of the magnetic axis is the south pole of the spin axis, with a ~11^o tilt angle at Earth and <1 ^{o} at Saturn. The solar wind plays a critical role in convection in Earth's magnetosphere. It serves as both the driving force and the primary plasma source.

Dungey [1961] proposed the open magnetosphere model, which uses magnetic reconnection to describe magnetospheric convection at Earth (see Figure 1.4). The solar wind compresses the Earth's magnetic field on the day side. When the interplanetary magnetic field (IMF) is southward, it can reconnect with the Earth's intrinsic magnetic field which is predominantly northward near the equatorial plane (see Figure 1.4, panels A and B). A field line after reconnection has one end connected to the Earth and the other connected to the IMF, and is called an open field line. Plasma can transfer from the solar wind to the Earth's magnetosphere along open field lines. These lines are then dragged anti-sunward to the magnetotail on the night side by the solar wind. Since the field lines are stretched, magnetic energy and magnetic flux are stored in the tail lobes. Reconnection can (and must) also happen in the tail, in the opposite sense to the process happening on the day side. Two open field lines connect to each other and form a closed field line with both ends connected to the Earth. Reconnection on the night side is accompanied by the release of magnetic energy and plasma injections sunward toward the Earth. The newly formed closed field lines are transported to the day side by the sunward plasma flow, where they are opened and swept back into the tail again. Figure 1.4, panel C shows the anti-sunward flow over the polar cap and the sunward flow in the low latitude region.

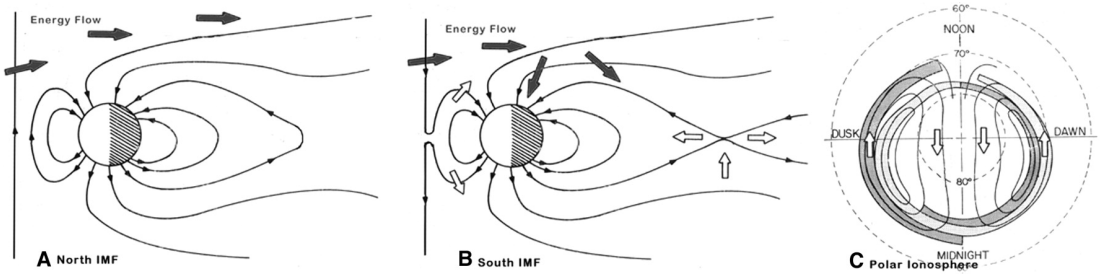

Figure 1.4 Concept of day side reconnection and the resulting plasma flow pattern of solar-wind-driven convection in Earth's magnetosphere. (A) No reconnection and no energy flow into the magnetosphere. Energy flow is indicated by solid arrows. (B) Reconnection opens the magnetosphere and allows entry of plasma, momentum, and energy. Magnetospheric convection is indicated by the open arrows. (C) The resulting currents and motions in the ionosphere for southward IMF. Panels A and B are in the meridian plane, and panel C is looking from the north. Figure from *Lyon* [2000].

This convection system drives several kinds of large-scale currents in Earth's magnetosphere. Figure 1.5 shows the global structure and current systems of Earth's magnetosphere. The magnetopause is defined as a surface where there is a sharp change in the magnetic field. According to Ampère's law, there should be currents flowing on the magnetopause, called magnetopause currents or Chapman-Ferraro currents. Similarly, the stretched magnetic field in the magnetotail implies westward currents through the center of the tail, called tail currents. There are also westward ring currents and partial ring currents in the inner magnetosphere based on observations. In general, the current density perpendicular to the magnetic field is not divergence-free, and currents flow along the magnetic field, to and from the ionosphere, to avoid buildup of charge. These currents are called field aligned currents (FAC, or Birkeland currents). Birkeland currents are essential to magnetosphere-ionosphere coupling (M-I coupling), which will be discussed further in Chapter 2.

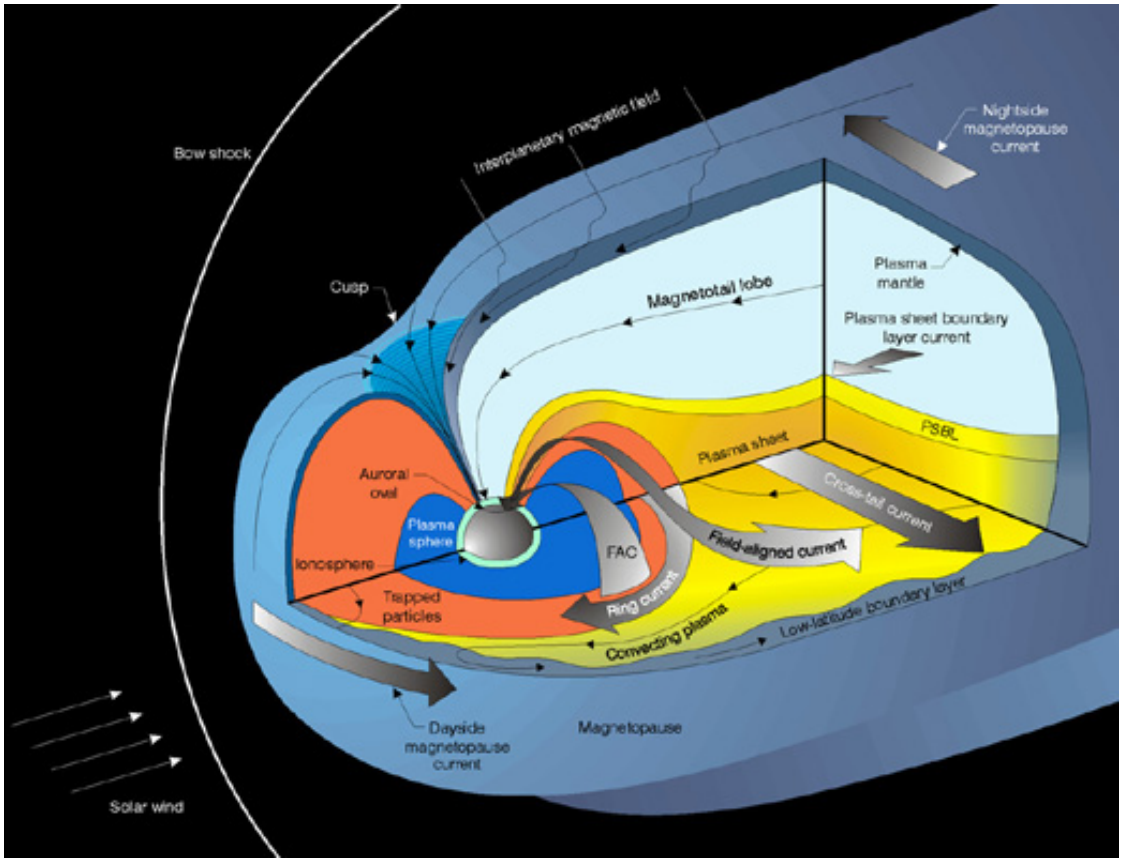

Figure 1.5 Conceptual diagram of the structure and current systems of Earth's magnetosphere. The thick solid arrows represent large-scale currents. The thin solid lines represent magnetic field lines, with the direction opposite to that of Saturn. Figure from Southwest Research Institute website. [http://mms.space.swri.edu/3Dmagnetosphere.jpg]

1.2.2. Rotation-driven convection

Owing to the faster rotation and larger size of Jupiter and Saturn compared to Earth, the centrifugal force is more important at the giant planets. *Brice and Ioannidis* [1970], on the basis of earlier terrestrial studies, defined a boundary called the plasmapause in Jupiter's magnetosphere to separate two regions with different convection mechanisms. The solar-wind-driven convection dominates the region outside the

plasmapause, while rotation-driven convection dominates the inner region [*Hill and Dessler*, 1991]. Recall that the magnetopause is the outer boundary of the magnetosphere. It is instructive to calculate the ratio of the plasmapause radius to the magnetopause radius, R_{PP}/R_{MP}. For typical solar wind conditions, the ratio R_{PP}/R_{MP} is ~0.6, 6.4 and 4.8 for Earth, Jupiter, and Saturn respectively [*Mauk et al*., 2009; Figure 1.6]. Therefore the bulk of Earth's magnetosphere is affected directly by solar-wind-driven convection ($R_{PP}/R_{MP} < 1$). But the bulk of Jupiter's and Saturn's magnetospheres are well inside their theoretical plasmapauses, and dominated by rotation-driven convection ($R_{PP}/R_{MP} >1$). Figure 1.6 shows the scaled magnetopauses and plasmapauses of Earth, Jupiter, and Saturn respectively. The plasma flowlines inside the plasmapause (heavy contour in the left panel) circle the planet; outside, the flowlines are generally sunward and approach the magnetopause.

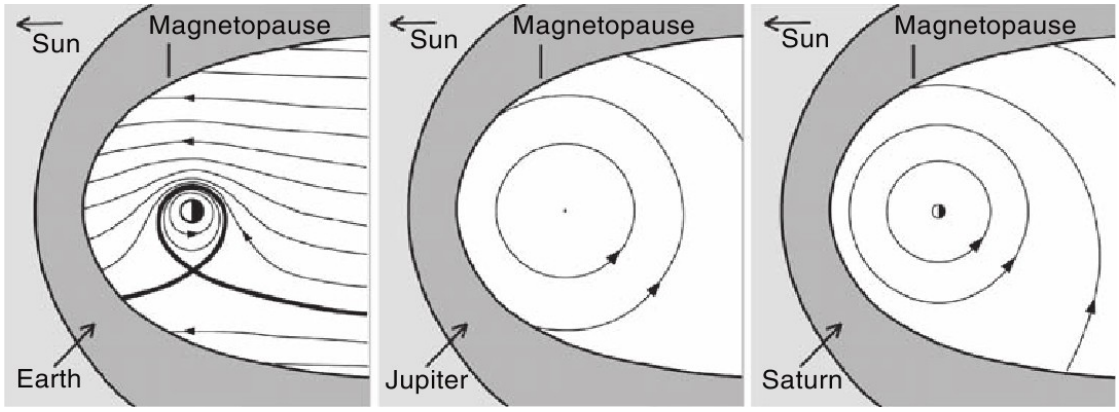

Figure 1.6 Scaled magnetopauses and plasmapauses of Earth, Jupiter and Saturn respectively. The heavy contour in the left panel represents the plasmapause of the Earth. This figure clearly shows that the magnetopause is well outside of the plasmapause in Earth's magnetosphere (left panel) for typical solar-wind conditions. For Jupiter and Saturn (middle and right panels), the magnetopause is well inside of the plasmapause. Figure from *Mauk et al.* [2009].

In their rotation-driven convection systems, both Jupiter and Saturn have interior plasma sources: primarily the inner satellites Io for Jupiter and Enceladus for Saturn. The centrifugal acceleration of corotation exceeds the gravitational acceleration beyond a certain distance ~2 Rj at Jupiter and ~2 Rs at Saturn (this is why we focus on the region 2 - 12 Rs in the Saturn's magnetosphere). The plasma generated by the interior source is then transported outward, ultimately forming a downtail planetary wind on the night side, and lost through reconnection and plasmoid ejection [*Hill et al.*, 1974]. Figure 1.7 illustrates the rotation-driven convection pattern in Jupiter's magnetosphere proposed by *Vasyliūnas* [1983], which is also applicable to Saturn's magnetosphere.

The current system of Saturn's inner magnetosphere is different from that of Earth. Plasma in Saturn's inner magnetosphere is partially corotating with Saturn. Accelerated by different forces, the plasma transport generates different currents, including a centrifugal current, a Coriolis current, and a pickup current. The divergence of these currents is balanced by the divergence of currents in the ionosphere through the connecting Birkeland currents. We will discuss this current system in Chapter 2.

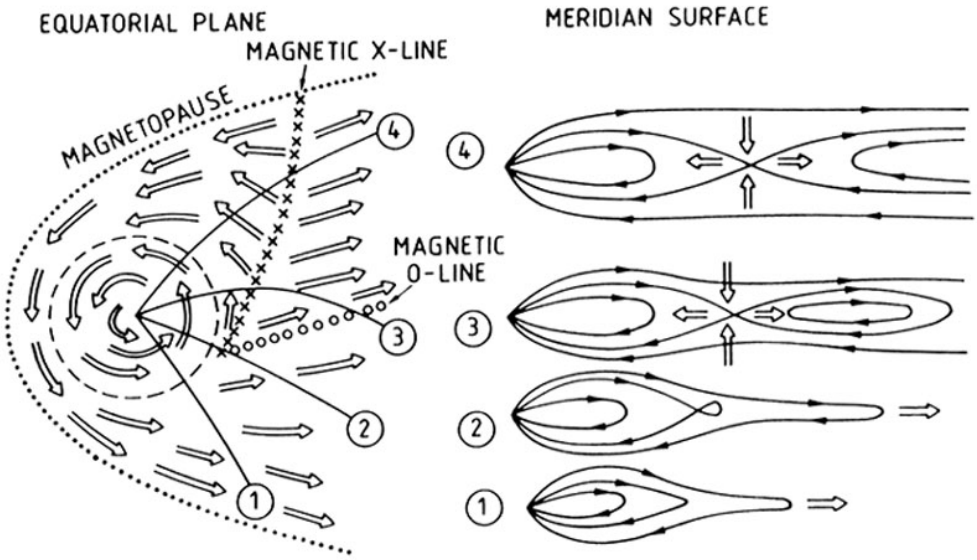

Figure 1.7 Conceptual illustration of the plasma flow pattern of the rotation-driven convection in Jupiter's magnetosphere, proposed by Vasyliūnas [1983]. Open arrows in the equatorial plane (left panel) represent plasma flow. Lines with arrowheads in the meridian plane (right panel) represent magnetic field lines.

1.3. Theories of plasma transport in Saturn's inner magnetosphere

1.3.1. Rayleigh-Taylor instability

As stated above, plasma convection in Saturn's magnetosphere is driven primarily by the centrifugal force from Saturn's rotation, and the plasma source is primarily Enceladus at 3.95 Rs. Here we discuss how the convection initiates and proceeds. First I would like to introduce a theoretical concept called the Rayleigh-Taylor instability.

Consider a container with two different types of liquid, which are insoluble to each other. Initially, the high density liquid is on the top, while the low density liquid is

on the bottom (Figure 1.8 top panel). This system is not stable because the gravitational potential could be reduced by interchanging the two liquids. If a perturbation is provided at the boundary, the two liquids would switch places (Figure 1.8 bottom panel): high density liquid tends to move down and low density liquid tends to move up. Some finger-like structures appear and evolve. Finally the system reaches a stable state when the gravitational energy reaches a stationary point. This is called Rayleigh-Taylor instability [*Rayleigh*, 1883; *Taylor*, 1950].

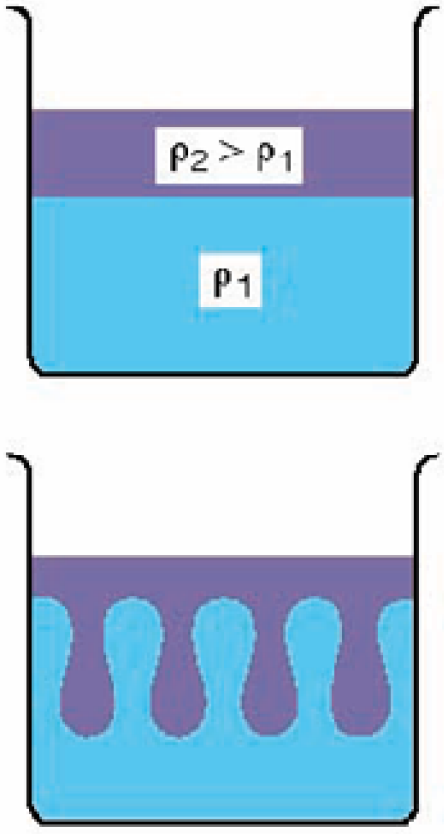

Figure 1.8 Concept of Rayleigh-Taylor instability. Figure courtesy of T. W. Hill.

It is easy to find that there are two requirements for the Rayleigh-Taylor instability. (1) Different types of liquid with different densities. (2) A driving force pointing from the high density liquid to the low density liquid. Here the driving force is gravity.

1.3.2. Centrifugal interchange instability

The Rayleigh-Taylor instability can be applied to Saturn's inner magnetosphere. (1) Saturn has an inner plasma source, Enceladus, located at 3.95 Rs. It ejects cold dense neutrals, which can be ionized to produce cool dense plasma. Outside 12 Rs, the outer boundary of our region of interest, there is hot tenuous plasma. (2) Owing to the fast rotation of Saturn, the centrifugal force of corotation exceeds the gravitational force beyond about 2 Rs, and the direction is radially outward (from the cool dense plasma toward the hot tenuous plasma).

In Saturn's inner magnetosphere, the plasma is often treated as a fluid with perfect conductivity, and is frozen to the magnetic field lines. Therefore magnetic flux tubes containing different plasma populations interchange with each other to transport plasma and energy. *Gold* [1959] first proposed the idea of interchange instability. Figure 1.9 shows the interchange of two magnetic flux tubes.

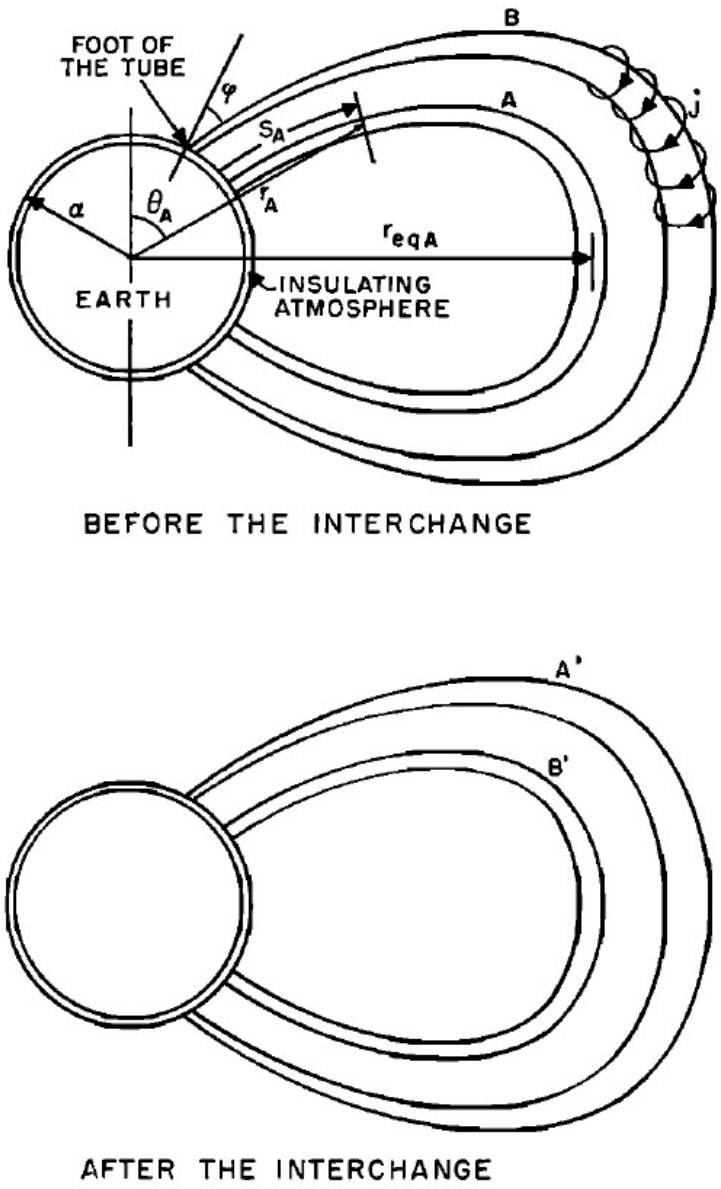

Figure 1.9 Concept of the interchange between two magnetic flux tubes. Figure from Sonnerup and Laird [1963].

Because the centrifugal interchange instability is similar to the Rayleigh-Taylor instability, the finger-like structures (fingers for short) should also appear in Saturn's inner magnetosphere. The first step of my research is to simulate the fingers in Saturn's

inner magnetosphere using a numerical model called the Rice Convection Model (RCM). The second step is to improve the numerical model by including more realistic conditions. The final step is to use the numerical model to simulate the observed fine scale signatures of Saturn's rotation-driven convection system, in particular, the ubiquitous injection/dispersion events.

Chapter 2

Rice Convection Model for Saturn

2.1. Rice Convection Model

The Rice Convection Model (RCM) is a numerical model, which uses a multi-fluid formalism to describe the adiabatically drifting particle distributions in a self-consistently computed electric field (potential distribution) and a specified magnetic field [*Toffoletto et al.*, 2003, and references therein]. Based on the logic scheme proposed by *Vasyliūnas* [1970], RCM was originally applied to the slow-flow region of Earth's inner and middle magnetosphere, especially, the region of closed magnetic field lines on which the plasma flow speed is much smaller than the fast mode speed [*Wolf*, 1983].

In Chapter 1, we noted that the magnetosphere and ionosphere are coupled through field aligned currents. The ionosphere is a part of the upper atmosphere. Generally it can be treated as a conducting spherical shell, because it is ionized by solar radiation. The RCM reduces the three-dimensional magnetosphere-ionosphere system to

a pair of coupled two-dimensional systems, one in the magnetosphere and one in the ionosphere. Figure 2.1 is the flowchart of the essential logical structure of the RCM. Starting from an initial condition, the RCM computes the magnetospheric currents, which are mainly provided by gradient-curvature drifts of plasma in the non-uniform and curved magnetic field lines. Because the divergence of the magnetospheric currents is non-zero, it is balanced by the divergence of the ionospheric currents through field-aligned currents. The ionospheric currents are accompanied by electric field distributions, which are mapped back to the magnetosphere through magnetic field lines (assuming no potential drop along the magnetic field lines). The electric field distributions cause extra $\mathbf{E}\times\mathbf{B}$ drift currents in the magnetosphere. Then the RCM repeats this loop at each time step.

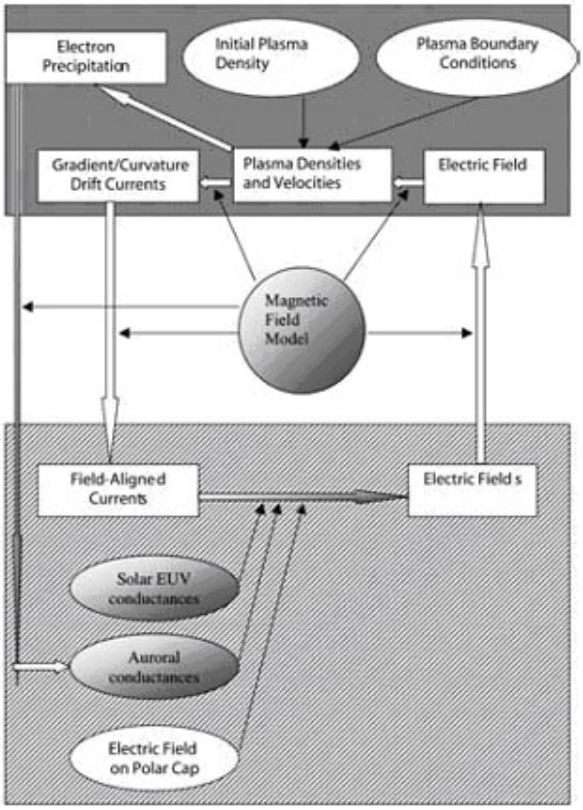

Figure 2.1 Flowchart of the logical structure of the RCM. Figure from Sazykin [2000].

2.2. Applying RCM to Saturn's inner magnetosphere

2.2.1. Logical loop of RCM-S

As noted in Chapter 1, both the plasma convection mechanism and the plasma composition are different at Saturn from those at Earth. To apply RCM to Saturn (RCM-S), we need to modify the magnetospheric currents.

Saturn's inner magnetosphere is dominated by the centrifugal effect of Saturn's rotation. Centrifugal currents are the main driver. In the rotating frame, the plasma is also

under the influence of the Coriolis effect, which causes Coriolis currents in the magnetosphere. Another kind of magnetospheric currents is pickup currents. Both the new ions generated by ionization and the ions resulting from charge exchange interactions, initially have the Keplerian velocity of the neutral gas. They are picked up by the local plasma flow. This process causes pickup currents.

Saturn's magnetosphere contains both cool and hot plasma. The cool plasma from the interior source Enceladus is centrifugally confined near the equatorial plane [*Hill and Michel*, 1976]. The thickness of the plasma sheet is twice the scale height. Figure 2.2 is the radial profile of the scale height [*Chen et al.,* 2010]. The solid curve is a fourth-order polynomial fit. The scale height reaches its minimum and maximum values at ~6 Rs and ~9 Rs respectively. We assume the scale height keeps its minimum and maximum values in the regions closer than ~6 Rs and beyond ~9 Rs, respectively. The cool plasma is not isotropic because it is centrifugally confined close to the equatorial plane. The cool plasma from the inner source has a finite temperature, and the associated gradient-curvature drift contributes extra gradient-curvature drift currents in the magnetosphere.

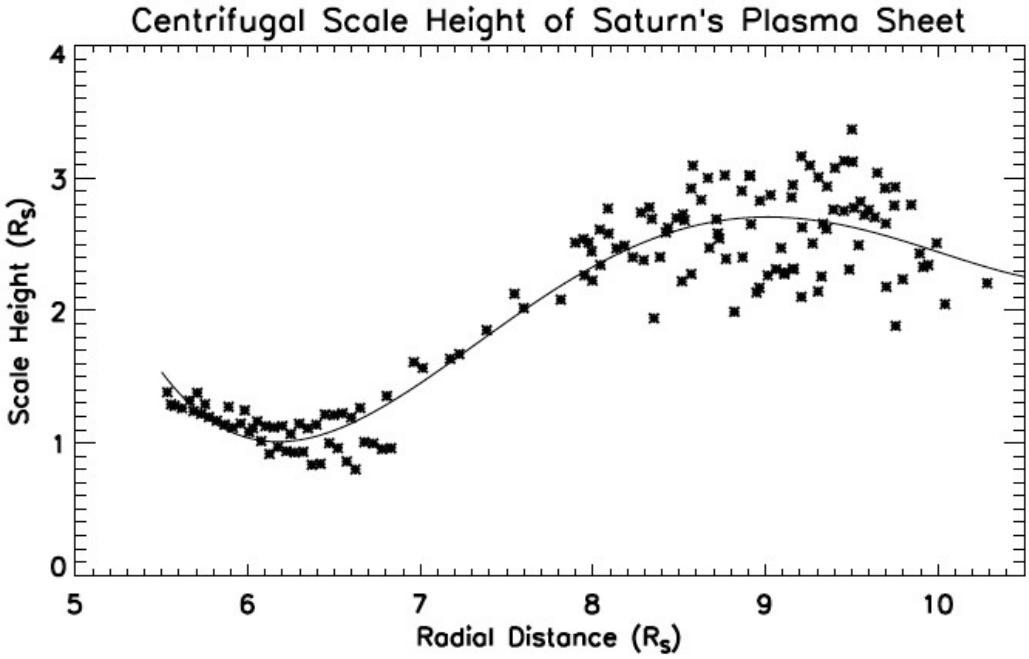

Figure 2.2 Radial profile of centrifugal scale heights derived from Cassini Plasma Spectrometer (CAPS) ion velocity moments. Figure from Chen et al. [2010].

The hot plasma in Saturn's magnetosphere is roughly isotropic, as in Earth's magnetosphere. In the non-uniform and curved magnetic field, the bounce-averaged gradient-curvature drift of hot plasma results in gradient-curvature currents in the magnetosphere.

In this thesis, we use four steps to develop the RCM-S.

(1): In Chapter 3, we include centrifugal, Coriolis, and pickup currents in the RCM-S to simulate the convection pattern in the magnetosphere *[Liu et al.*, 2010]. In this first step, only cool plasma from the interior source is considered, and the temperature is assumed to be zero. Hot plasma is ignored temporarily.

(2): In Chapter 4, we discuss the interior plasma source and try three available source models.

(3): In Chapter 5, we include gradient-curvature drift currents of the cool plasma to investigate the effects of finite temperature and associated plasma pressure [*Liu and Hill*, 2012].

(4): In Chapter 6, the hot plasma and its bounce-averaged gradient-curvature drift currents are added. We use RCM-S to simulate the observed V-shape signatures of injection/dispersion events of hot plasma.

Figure 2.3 shows the logical structure of RCM-S. Starting from the plasma density and velocity distributions in the magnetosphere, RCM-S computes the perpendicular current density in the magnetosphere

$$\mathbf{J}_{\perp e} = \frac{\mathbf{B}_e}{B_e} \times \left[-\eta \Omega^2 \mathbf{r}_e + 2\eta \boldsymbol{\Omega} \times \mathbf{v} + \dot{\eta}_s \left(\boldsymbol{\Omega} \times \mathbf{r}_e + \mathbf{v} - \mathbf{v}_n \right) \right] \tag{2.1}$$

(see Appendix A) where $\mathbf{J}_{\perp e}$ is the magnetospheric perpendicular current density integrated along the magnetic field line across the plasma sheet thickness, subscript e means in the equatorial plane, $\eta = \int \rho ds / B$ is the flux tube plasma mass content, $\dot{\eta}_s = \int \dot{\rho} ds / B$ is the sum of charge-exchange and new ionization rates of the plasma source model in units of $d\eta/dt$, and $\mathbf{v}_n$ is the neutral gas Keplerian velocity before

ionization. The three terms on the right side of (2.1) are the centrifugal, Coriolis, and pickup currents, respectively, all associated with planetary rotation. The gradient-curvature drift currents of cool plasma from the inner source and hot plasma from the outer boundary are not included in the first step.

The divergence of $\mathbf{J}_{\perp e}$ is not zero, and is related to the ionosphere through the field-aligned Birkeland current by

$$\frac{j_{\parallel i}}{B_i} = \frac{j_{\parallel e}}{B_e} \tag{2.2}$$

with

$$j_{\parallel e} = \nabla_e \cdot \mathbf{J}_{\perp e} \tag{2.3}$$

Where $j_{\parallel i}$ is the field-aligned Birkeland current density just above the ionosphere, defined to be positive when upward from the ionosphere, subscript i means in the ionosphere, $j_{\parallel e}$ is the field-aligned Birkeland current density near the equatorial plane, including currents connecting to both the northern and southern hemispheres of Saturn, and ∇_e is the two-dimensional gradient operator in the equatorial plane. The RCM-S code used here combines the conductances of the northern and southern ionospheres (in

parallel) in a single northern-hemisphere ionospheric shell. Thus our adopted values for the physical ionospheric conductances (for example, Σ_P = 0.3 S, Σ_H = 0 in the first step simulations) represent the sum of the conductances of both hemispheres.

Because the ionosphere is represented as a conducting spherical shell, the RCM-S solves for the ionospheric distribution of the electrostatic potential Φ from the current conservation equation

$$\nabla_i \cdot \left[\vec{\Sigma} \cdot \left(-\nabla_i \Phi \right) \right] = -j_{\parallel i} \sin I \tag{2.4}$$

where ∇_i is the horizontal gradient operator in the ionosphere, $\vec{\Sigma}$ is the ionospheric conductance tensor, and I is the magnetic field inclination angle defined by $\sin I = \left| B_r / B \right|$. Combining (2.2)-(2.4) gives

$$\nabla_i \cdot \left[\vec{\Sigma} \cdot \left(\nabla_i \Phi \right) \right] = \frac{B_{ir}}{B_e} \nabla_e \cdot \mathbf{J}_{\perp e} \tag{2.5}$$

With the ideal magnetohydrodynamic (MHD) approximation

$$\mathbf{E} + \mathbf{v} \times \mathbf{B} = 0 \tag{2.6}$$

the potential solution obtained from (2.5) provides the $\mathbf{E}\times\mathbf{B}$ drift of magnetospheric plasma (with $\mathbf{E}=-\nabla\Phi$), which is used to advance the equatorial η distribution at the end of each simulation time step.

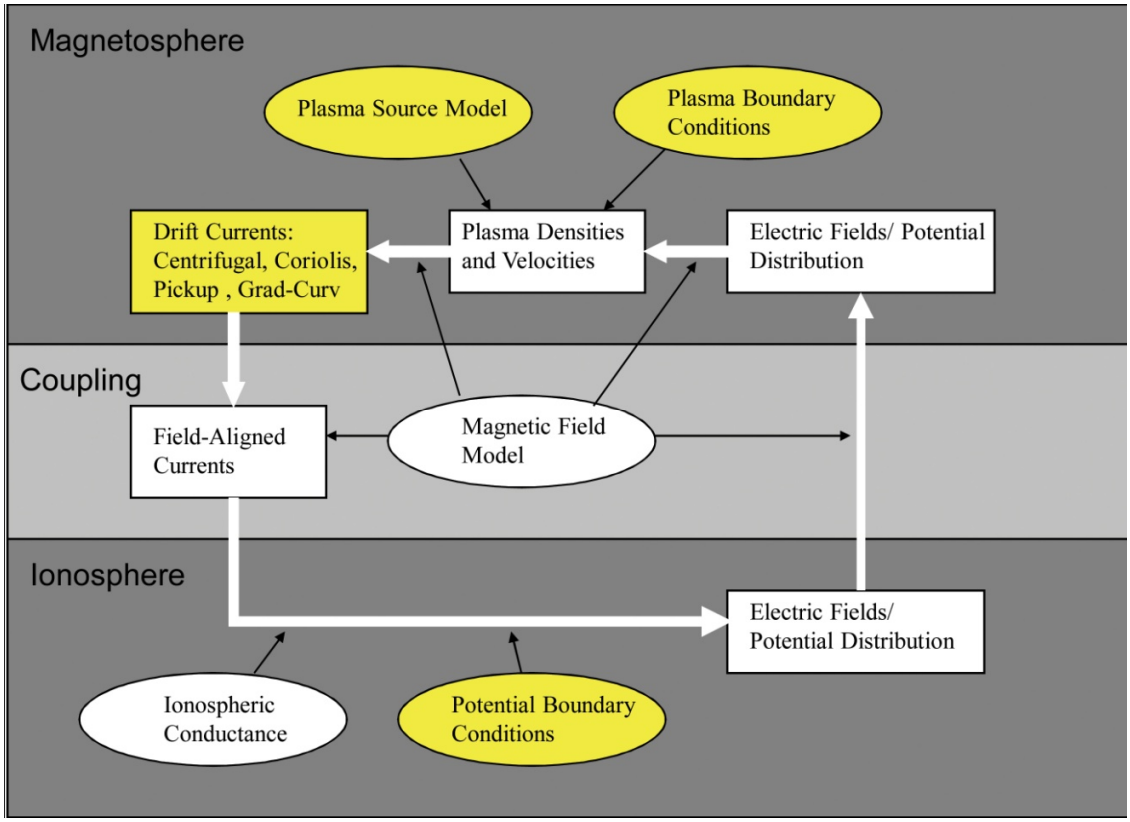

Figure 2.3 Logical structure of RCM-S. In the first step, only centrifugal, Coriolis, and pickup currents are included in the magnetospheric currents. The gradient-curvature drift currents of cool plasma from the interior source and hot plasma from the outer boundary will be included later. Yellow sections highlight the differences between RCM-S and original RCM for Earth.

2.2.2. Implicit method to include the Coriolis current and the v-dependent part of the pickup current

The standard procedure in each simulation time step for RCM-S is first to calculate the magnetospheric currents of (2.1), then solve the potential distribution in (2.5), and at last solve (2.6). However, in (2.1), both the Coriolis term and the pickup current term (second and third terms on the right) contain the plasma velocity $\mathbf{v}$, which is not calculated until the end of the time step in (2.6). For their Jupiter study, *Yang et al.* [1994] used $\mathbf{v}(t-\Delta t)$ from the previous time step to evaluate the Coriolis term on the right side of (2.1). Their results showed that this approach worked well only when the Coriolis term was small, but became numerically unstable when that term became large. For the Saturn case, both the Coriolis and pickup terms have significant effects. Therefore we need a new approach to evaluate (2.1) and avoid this numerical instability.

The ionospheric conductance tensor can be expanded as

$$\vec{\vec{\Sigma}} = \begin{pmatrix} \Sigma_{\alpha\alpha} & \Sigma_{\alpha\beta} \\ \Sigma_{\beta\alpha} & \Sigma_{\beta\beta} \end{pmatrix} = \begin{pmatrix} \Sigma_{\theta\theta} & \Sigma_{\theta\varphi} \\ \Sigma_{\varphi\theta} & \Sigma_{\varphi\varphi} \end{pmatrix} \tag{2.7}$$

where (θ, φ) are spherical angular coordinates on the ionospheric shell $r = R_S$, and

$$\alpha = \frac{M\sin^2\theta}{r} \qquad \beta = \varphi \tag{2.8}$$

are the Euler potentials of the spin-aligned dipole field with dipole moment *M*, such that **B** = $\nabla\alpha\times\nabla\beta$. If we define the Hall and Pedersen conductance as

$$\Sigma_H = \int \sigma_H ds \tag{2.9a}$$

$$\Sigma_P = \int \sigma_P ds \tag{2.9b}$$

where σ_H and σ_P are Hall and Pedersen conductivity (S/m) of the ionosphere, respectively, then we have

$$\Sigma_{\theta\theta} SinI = \Sigma_{\varphi\varphi} / SinI = \Sigma_P \tag{2.10a}$$

$$\Sigma_{\varphi\theta} = -\Sigma_{\theta\varphi} = \Sigma_H \tag{2.10b}$$

[*Wolf et al*., 2006]. In (2.1) because the Coriolis current term is parallel to $\mathbf{v}$, and thus perpendicular to $\mathbf{E}$, it turns out that the Coriolis term can be included implicitly by adding an effective (negative) contribution

$$\Sigma_H^* = -\frac{2\Omega\eta}{B_e} \tag{2.11}$$

to the physical ionospheric Hall conductance Σ_H. We show in Appendix B that this device is mathematically equivalent to the effect of including the Coriolis term in (2.1) with the (yet to be calculated) value of **v** appropriate to the present time step.

Similarly, the **v**-dependent part of the pickup current term in (2.1) is parallel to **E**, and we show in Appendix C that this term can be included implicitly, using the instantaneous value of **v,** by adding an effective contribution

$$\vec{\Sigma}_P^* = \begin{pmatrix} \Sigma_{\alpha\alpha}^* & \Sigma_{\alpha\beta}^* \\ \Sigma_{\beta\alpha}^* & \Sigma_{\beta\beta}^* \end{pmatrix} = \begin{pmatrix} \Sigma_{\theta\theta}^* & \Sigma_{\theta\varphi}^* \\ \Sigma_{\varphi\theta}^* & \Sigma_{\varphi\varphi}^* \end{pmatrix} = \frac{\dot{\eta}_s}{B_e} \begin{pmatrix} \dfrac{\sin I}{2\cos\theta} & 0 \\ 0 & \dfrac{2\cos\theta}{\sin I} \end{pmatrix} \tag{2.12}$$

to the physical Pedersen conductance Σ_P of the ionosphere.

The source term $\dot{\eta}_s$ in (2.1) and (2.12) includes both the rate of electron-impact ionization of neutral molecules and the rate of charge-exchange reactions between ions and neutral molecules. Both processes contribute equally to the rate of momentum loading of a given convecting flux tube as represented in (2.1). (Newly created ions, from

either process, must be accelerated from their former Keplerian velocity up to the local plasma velocity.) However, only the former process (electron-impact ionization) contributes a net addition to the plasma mass content of a convecting flux tube, and only that fraction of $\dot{\eta}_s$ is used to update the η values in the simulation.

The equations for the first step of RCM-S are

$$\mathbf{J}_{\perp e} = \frac{\mathbf{B}_e}{B_e} \times \left[-\eta \Omega^2 \mathbf{r}_e + \dot{\eta}_s \left(\boldsymbol{\Omega} \times \mathbf{r}_e - \mathbf{v}_n \right) \right] \tag{2.13a}$$

$$\nabla_i \cdot \left[\vec{\Sigma}^* \cdot \left(\nabla_i \Phi \right) \right] = \frac{B_{ir}}{B_e} \nabla_e \cdot \mathbf{J}_{\perp e} \tag{2.13b}$$

$$\mathbf{E} + \mathbf{v} \times \mathbf{B} = 0 \tag{2.13c}$$

with

$$\vec{\Sigma}^* = \begin{pmatrix} (\Sigma_P + \Sigma^*_{\theta\theta}) / \sin I & -(\Sigma_H + \Sigma^*_H) \\ \Sigma_H + \Sigma^*_H & (\Sigma_P + \Sigma^*_{\varphi\varphi}) \sin I \end{pmatrix} \tag{2.13d}$$

$$\Sigma^*_H = -\frac{2\Omega\eta}{B_e} \tag{2.13e}$$

$$\Sigma^*_{\theta\theta} = \frac{\dot{\eta}_s}{B_e} \frac{\sin I}{2\cos\theta} \tag{2.13f}$$

$$\Sigma^{*}_{\varphi\varphi} = \frac{\dot{\eta}_s}{B_e}\frac{2\cos\theta}{\sin I} \tag{2.13g}$$

Chapter 3

Initial simulation of plasma transport using RCM-S

3.1. Introduction

As stated in Chapter 1, Saturn's rapidly rotating magnetosphere exhibits centrifugally driven radial transport from an internal plasma source associated with the icy satellite Enceladus. As at Jupiter, the fast rotation of Saturn makes solar-wind-driven convection unimportant compared with centrifugally driven convection, at least in the region of closed magnetic field lines (L <~ 20). However, Saturn's magnetosphere, unlike Jupiter's, is dominated by a broad distribution of neutral water-group molecules, first detected in OH emission by the Hubble Space Telescope (HST) [*Shemansky et al.*, 1993]. *Johnson et al.* [2006] and *Cassidy and Johnson* [2010] argue that the Enceladus neutral gas torus, produced directly from the south-pole Enceladus plume, is scattered through charge exchange and neutral-neutral collisions to produce the wider OH torus observed by HST.

This neutral gas cloud produces a broadly distributed plasma source in Saturn's inner magnetosphere which drives a centrifugally driven convection system between the inner and outer magnetosphere. (The distinction between "inner" and "outer" magnetosphere, for our purposes, is based on the location ($L \sim 12$) beyond which the magnetic field becomes significantly non-dipolar.) The most definitive observational signatures of this convection process are the injection and drift dispersion signatures of hot, low-density plasma that moves inward to replace the magnetic flux lost by cool dense plasma moving outward [*André et al*., 2005; *Burch et al*., 2005; *Hill et al.,* 2005; *Mauk et al*., 2005]. *Chen and Hill* [2008] reported that the injection/dispersion structures occupy only about 5-10% of the available longitude space, indicating a picture of Saturn's centrifugally driven magnetospheric convection in which narrow, fast inflow channels alternate with wider, slower outflow channels. This is a previously unexplained feature of the CAPS plasma observations.

Goldreich and Farmer [2007] and *Gurnett et al.* [2007] proposed a rotating two-cell plasma convection pattern to explain the observed spin periodicities in Saturn's magnetosphere (see Figure 3.1). This idea was proposed for Jupiter by *Vasyliūnas* [1978] and formulated mathematically by *Hill et al*. [1981]. For both Jupiter and Saturn the idea was first motivated by observed spin periodicities of various magnetospheric phenomena. At Jupiter, there is an obvious physical cause of the persistent longitude asymmetry, namely, the strong azimuthal asymmetry of the planet's intrinsic magnetic field. At Saturn, no such asymmetry has yet been identified.

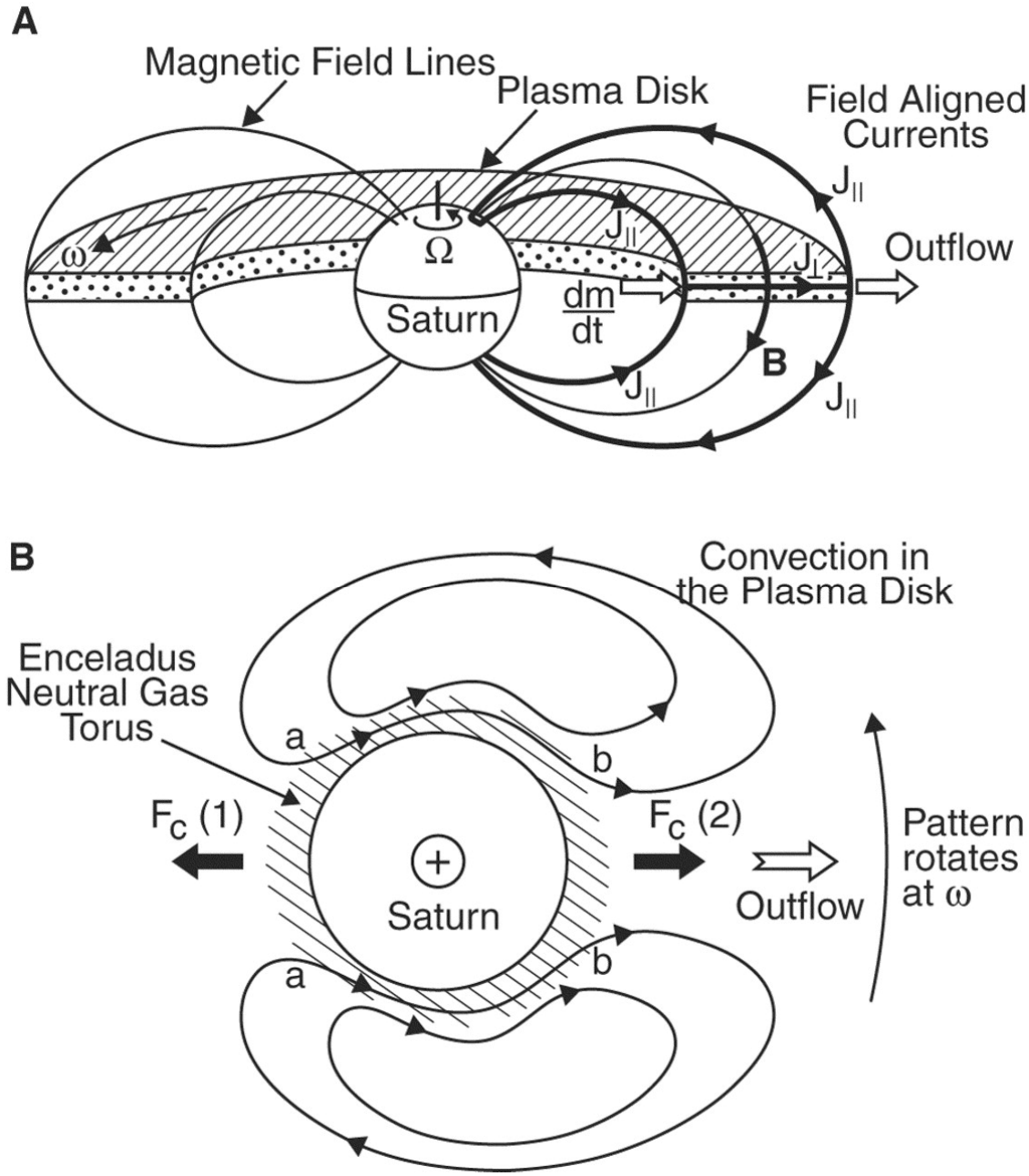

Figure 3.1 Rotating two-cell plasma convection pattern in Saturn's magnetosphere. (A) The mechanism by which the plasma disk (shaded area) is coupled to the ionosphere through field aligned currents. (B) Rotating two-cell plasma convection pattern driven by the centrifugal instability. Figure from *Gurnett et al.* [2007].

Another feature of Saturn's inner magnetosphere is the deviation from rigid corotation of the magnetospheric plasma. Both radial plasma transport and the associated Coriolis acceleration, and plasma mass loading including charge exchange and ionization, and the associated pick-up current, lead to changes in the plasma's rotation rate. Coupling between magnetosphere and ionosphere opposes the departure from corotation. *Hill* [1979, 1980] developed a model to describe the azimuthal velocity variation in Jupiter's magnetosphere under the influence of outward plasma transport alone, while *Pontius and Hill* [1982] investigated the effect of mass loading alone on the plasma azimuthal velocity in the Io plasma torus. In Saturn's case, however, because of the widely distributed plasma source, both outward transport and local mass loading are expected to contribute significantly in the same region, so both need to be considered together. Two theoretical models have been proposed to include both mechanisms simultaneously [*Saur et al.*, 2004; *Pontius and Hill,* 2009].

In this chapter, we use the numerical model RCM-S, described in Chapter 2, to investigate the relationship between the distributed plasma source and the longitudinal spacing and width of plasma flow channels. The simulation results conform to the observed pattern of convection in Saturn's inner magnetosphere: broad channels of cold dense plasma flowing slowly outward, interspersed with narrow channels of hot tenuous plasma flowing rapidly inward. We also investigate the combined roles of the Coriolis acceleration and the pickup process in producing the observed corotation lag.

3.2. Model setup

3.2.1. Boundary conditions

We attempt to simulate plasma motion in Saturn's "inner magnetosphere" defined here by the radial range $2 < L < 12$. The inner boundary location $L = 2$ is chosen to be well inside the region of significant plasma sources (see below) but still outside the region affected by Saturn's dense particulate rings. Analytical calculations [*Huang and Hill*, 1991; *Yang et al.*, 1994] show that the inner boundary condition has little effect on the interchange instability development provided that boundary is located well inside the region of significant plasma sources. At this inner boundary we impose the Dirichlet boundary condition $\Phi = 0$, where Φ is the electrostatic potential, corresponding to zero radial flow across that boundary. We place our outer computational boundary at $L = 40$, far outside the region of interest (and far outside the region where our assumptions are valid), in order to suppress the effects of this outer boundary within our region of interest ($2 < L < 12$). At this outer boundary we impose the Neumann boundary condition $\partial\Phi/\partial L = 0$, corresponding to purely radial but otherwise free flow through that boundary. The free outflow condition is required by the physics of the problem, but the purely radial direction of that outflow is not; this is why we place the outer boundary well outside our region of interest, so that the radial direction of the outflow is not reflected in the flow pattern within $L < 12$. By trial and error we found that this required an outer boundary location $L > \sim 20$. To err on the safe side, we doubled this.

3.2.2. Magnetic field model

In our simulation region, the Saturnian magnetic field is assumed to be a dipole aligned with the spin axis:

$$\mathbf{B} = \frac{3(\mathbf{M} \cdot \hat{\mathbf{r}})\hat{\mathbf{r}} - \mathbf{M}}{r^3} \tag{3.1}$$

where **M** is the magnetic moment of Saturn. The magnetic field at Saturn's surface in the equatorial plane is $B_{e0} = 2.11 \times 10^4 nT$, directed southward. A dipole magnetic field line is mapped from the equatorial plane to the ionosphere by

$$L = 1/\sin^2\theta \tag{3.2}$$

where θ_i is the ionospheric co-latitude. The ionosphere is represented as a spherical shell lying 1000 km above Saturn's surface

$$r_i = Rs + 1000 \tag{3.3}$$

with Rs = 60268 km. (Saturn's "surface" [visible cloud tops] is noticeably oblate, but a spherical representation is perfectly adequate for the present purposes.)

3.2.3. Ionospheric conductance

As described in Chapter 2, the physical conductance tensor of Saturn's ionosphere is

$$\vec{\vec{\Sigma}}_S = \begin{pmatrix} \Sigma_{\theta\theta} & \Sigma_{\theta\varphi} \\ \Sigma_{\varphi\theta} & \Sigma_{\varphi\varphi} \end{pmatrix} = \begin{pmatrix} \Sigma_P / \sin I & -\Sigma_H \\ \Sigma_H & \Sigma_P \sin I \end{pmatrix} \tag{3.4}$$

Notice that it is different from that of Earth

$$\vec{\vec{\Sigma}}_E = \begin{pmatrix} \Sigma_P / \sin I & \Sigma_H \\ -\Sigma_H & \Sigma_P \sin I \end{pmatrix} \tag{3.5}$$

because the magnetic dipole moment of Earth is (roughly) anti-aligned with the spin axis, while Saturn's is (almost exactly) aligned.

We assume a uniform (physical) Pedersen conductance Σ_P of 0.3 S for Saturn's ionosphere (N/S hemispheres in parallel). This value is physically plausible but poorly constrained empirically [*Moore et al.*, 2010]. The Pedersen conductance controls the

growth rate of the convection pattern. A larger (smaller) Pedersen conductance would produce a proportionally slower (faster) development of the same basic flow pattern, as implied by (2.5). In Chapters 4 and 5, we will modify the physical Pedersen conductance with an effective conductance term when different plasma source models are incorporated, and new mechanisms are included such as the gradient-curvature drift of plasma. The physical Hall conductance Σ_H is always assumed to be 0.

3.2.4. Plasma composition

For the first step, only cold ions from Enceladus are considered. The mean ion mass is taken to be 17 amu, representing a "water-group" mixture of H_3O^+, H_2O^+, OH^+, and O^+ [*Young et al.*, 2005]. The ion temperature is set to zero, which means that the gradient-curvature drift of magnetospheric plasma is neglected temporarily. The finite temperature of the cold plasma is included in Chapter 5, and the hot plasma is included in Chapter 6.

3.2.5. Inner plasma source model

Our plasma source model is based on the neutral cloud model of *Johnson et al.* [2006] (we call it the J06 model), which has a much broader radial distribution than that of the assumed neutral gas source at $L = 4$. *R. E. Johnson* [private communication, 2008] divided the neutral densities of that model by appropriate neutral-particle lifetimes estimated from CAPS plasma data [*Sittler et al*., 2005] to produce the plasma source rate model shown in Figure 3.2. This includes both the charge exchange rate (solid curve), which contributes to $\dot{\eta}_s$ in (2.1) and (2.12) but not to the net η source, and the new

ionization rate (dashed curve), which contributes to both. This plasma source model indicates that charge exchange dominates in the region $L < \sim 5$ and new ionization dominates in the region $L > \sim 5$. Figure 3.3 shows the radial profile of ionization rate in different units: rate per unit equatorial area (solid curve with left Y-axis) and rate per unit magnetic flux (dashed curve with right Y-axis). The dashed curve in Figure 3.2 and the solid curve in Figure 3.3 are exactly in the same shape. Notice the Y-axis is logarithmic in Figure 3.2, but linear in Figure 3.3.

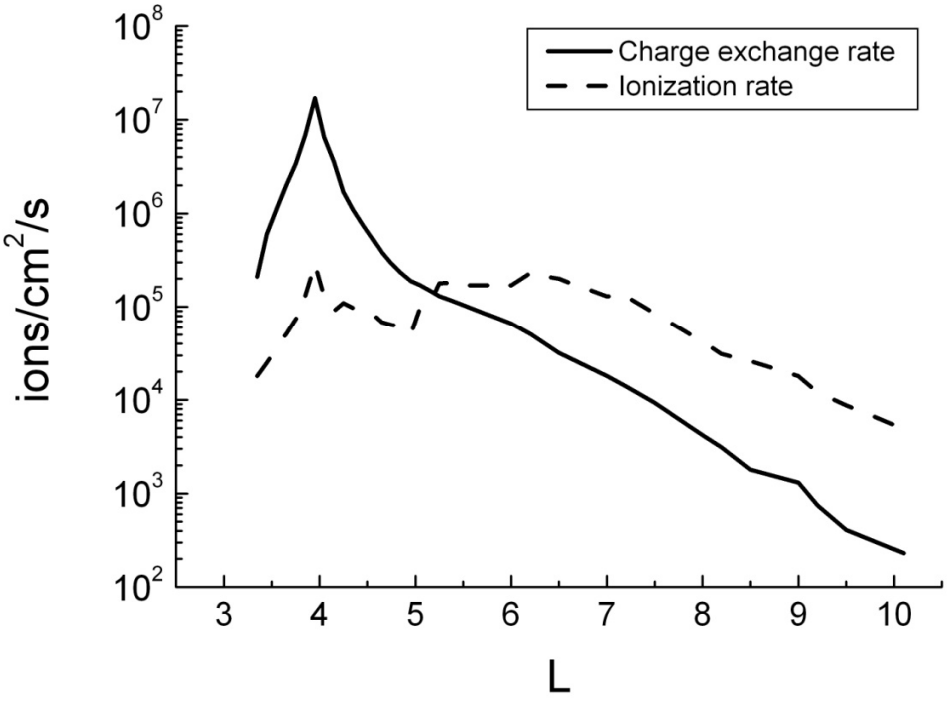

Figure 3.2 Plasma source model (J06) adopted for Saturn's inner magnetosphere, including charge exchange (solid curve) and ionization rates (dashed curve) [Johnson et al., 2006; R. E. Johnson, private communication, 2008]. Charge exchange dominates in the region $L < \sim 5$ and new ionization dominates in the region $L > \sim 5$.

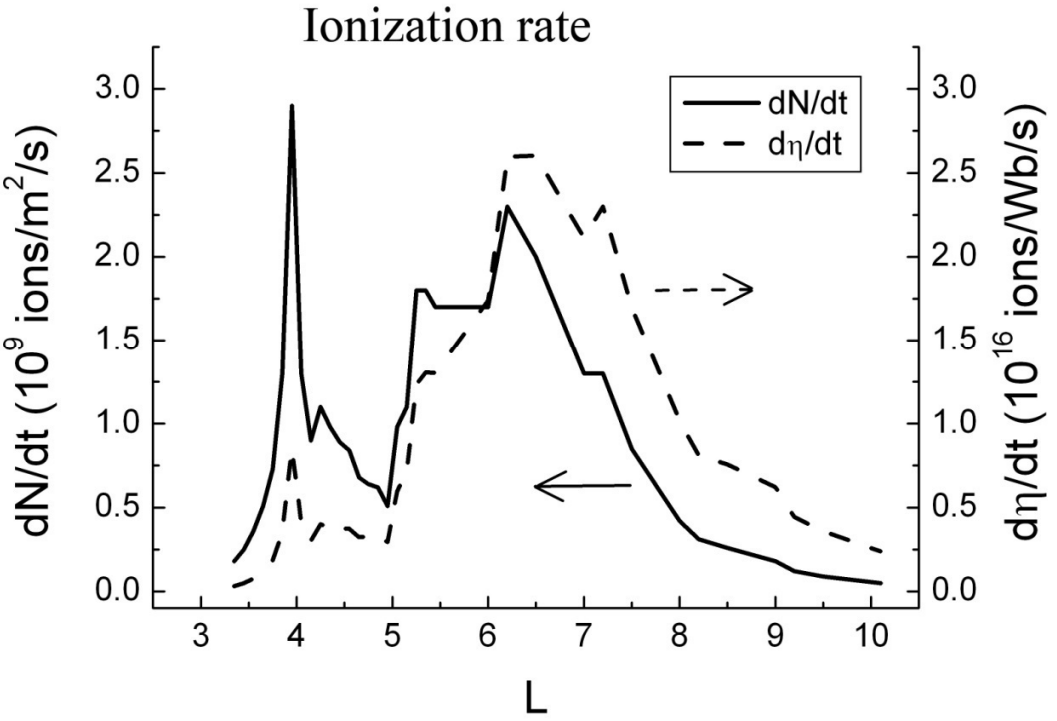

Figure 3.3 Ionization rate of the J06 plasma source model. Solid curve is rate per unit equatorial area. Dashed curve is rate per unit magnetic flux.

3.3. Simulation results

3.3.1. Coriolis effect

Before adding the continuously active plasma source, we first ran a series of initial-value simulations to investigate the consequences of the Coriolis effect in the absence of the pick-up currents associated with the source. Sample results are illustrated in Figure 3.4. Color indicates flux-tube mass content η in the equatorial plane at a

particular simulation time. The two panels show η contours at the same simulation time for two simulations, one without (left panel) and one with (right panel) the Coriolis effect included. The two simulations are otherwise identical in all respects. The simulations were initialized with a toroidal distribution of $\eta(L)$ confined between L = 3.5 and 4.5 with a simple $\cos^2 L$-dependence

$$\eta(r) = \begin{cases} \eta_{\max} \cos^2 \dfrac{(r - r_e)\pi}{2\delta} : |r - r_e| \le \delta \\ 0 : elsewhere \end{cases} \tag{3.6}$$

where r_e = 3.95 R_S is the radius of Enceladus' orbit and δ = 0.5 R_S is the full width at half maximum of this distribution. Two effects are apparent. First, the Coriolis acceleration bends the "fingers" in the retrograde sense as they grow outward, as expected intuitively. Secondly, the Coriolis effect significantly slows the outward growth of the fingers; this effect, while perhaps not so intuitively obvious, was predicted theoretically by *Pontius* [1997].

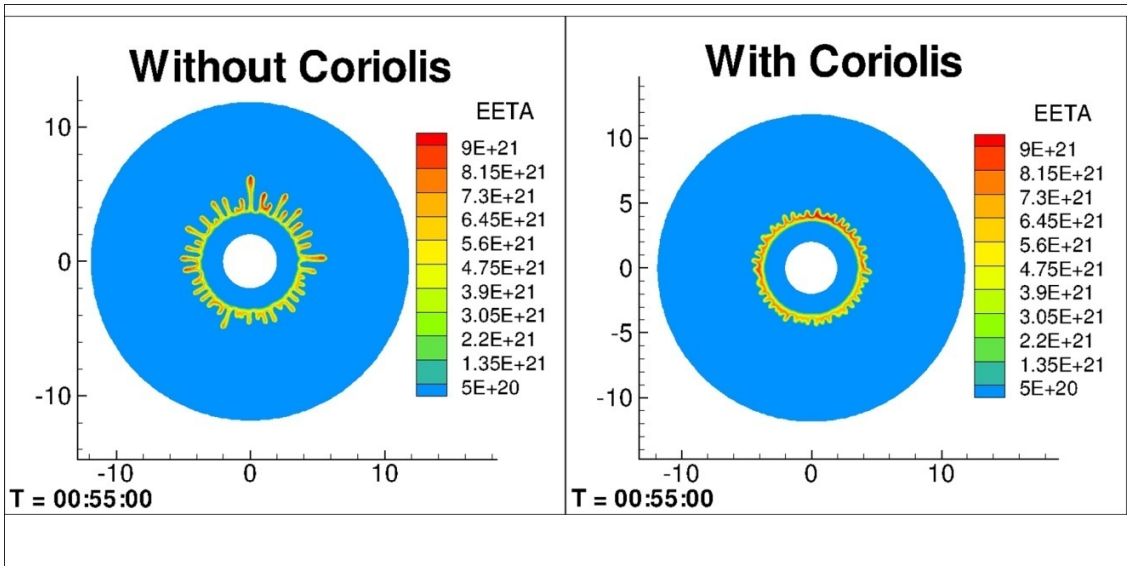

Figure 3.4 Two initial-value simulations at the same simulation time, with identical parameters except without (left) and with (right) the Coriolis effect included. Color indicates flux-tube ion content (ions/Weber) projected on the equatorial plane in the corotating frame of reference.

3.3.2. Simulation results with active plasma source

Figure 3.5 shows the distribution of flux tube mass content in the magnetosphere (in Saturn's rotating frame, looking from the north) at various simulation times during a simulation with the active plasma source included. Panels a to f show representative stages of the evolution: pre-appearance of outflow fingers, appearance of outflow fingers, developing, further developing, pre-mature, and mature.

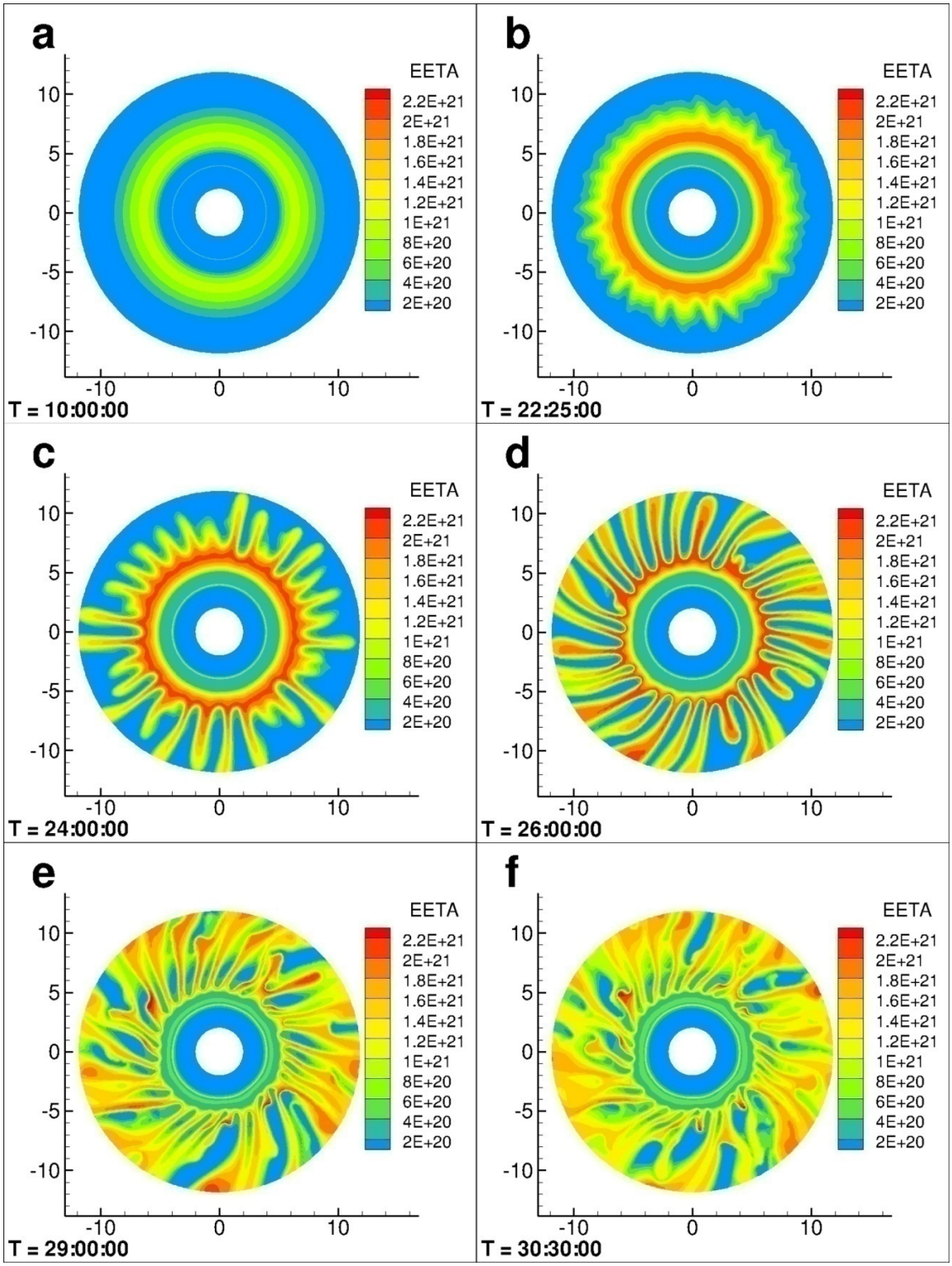

Figure 3.5 Simulation results for the evolution of plasma convection in Saturn's inner magnetosphere, in the same format as Figure 3.4 but with the active plasma source shown

in Figures 3.2 and 3.3. (3a) Plasma accumulates in the region of maximum source rate. (3b) Radial flow fingers are produced by the centrifugal interchange instability. (3c-3d) Outflow fingers grow outward under the influence of the Coriolis force and pickup currents. (3e) Outflow fingers become wider and slower than inflow fingers. (3f) The convection system approaches a quasi-steady state, wherein the detailed pattern continues to change chaotically but the statistical properties approach an asymptotic state.

The simulation begins with an empty magnetosphere. Figure 3.5a shows that, during the first few hours, the plasma accumulates in the region of maximum ionization rate (dashed line in Figure 3.3). Figure 3.5b shows that after sufficient accumulation time, outflow fingers appear as a result of the centrifugal interchange instability. Figures 3.5c and 3.5d show the continued nonlinear growth of the fingers. The outflow fingers are clearly bent in the retrograde direction by the Coriolis acceleration and the pickup effect. Figures 3.5e and 3.5f illustrate the increasing tendency of the inflow channels (blue) to become much narrower than the outflow channels, as discussed further below. Later simulation times, not shown here, suggest that the simulation has reached a quasi-steady state by Figure 3.5f in the sense that, although the instantaneous convection pattern continues to change chaotically with time, its statistical properties, when averaged over fluctuations, become less variable.

Figure 3.6 is a magnified view of Figure 3.5f with equipotential lines included, at 15 kV intervals. The equipotential lines are also instantaneous streamlines of the plasma flow ($\mathbf{E}\times\mathbf{B}$ drift). Figure 3.7 shows the plasma mass flux at the same time step. The blue regions in Figure 3.6 are relatively empty, having spent little time in the source region, and thus do not contribute to the inward mass flux. Both “inward flux” and “outward flux” in figure 3.7 are dominated by streamlines that have encountered the main source region;

plasma on these streamlines sometimes moves inward because of back-and-forth meandering (shown in Figure 3.6). The "total ionization rate" is the integral of ionization rate over the radial distance in the simulation region (2 < L < 12), multiplying by the ion mass, 17 amu. The result is ~24 kg/s. Figure 3.7 indicates a quasi-equilibrium between the net outward plasma mass flux at a given distance and the total ionization rate within that distance.

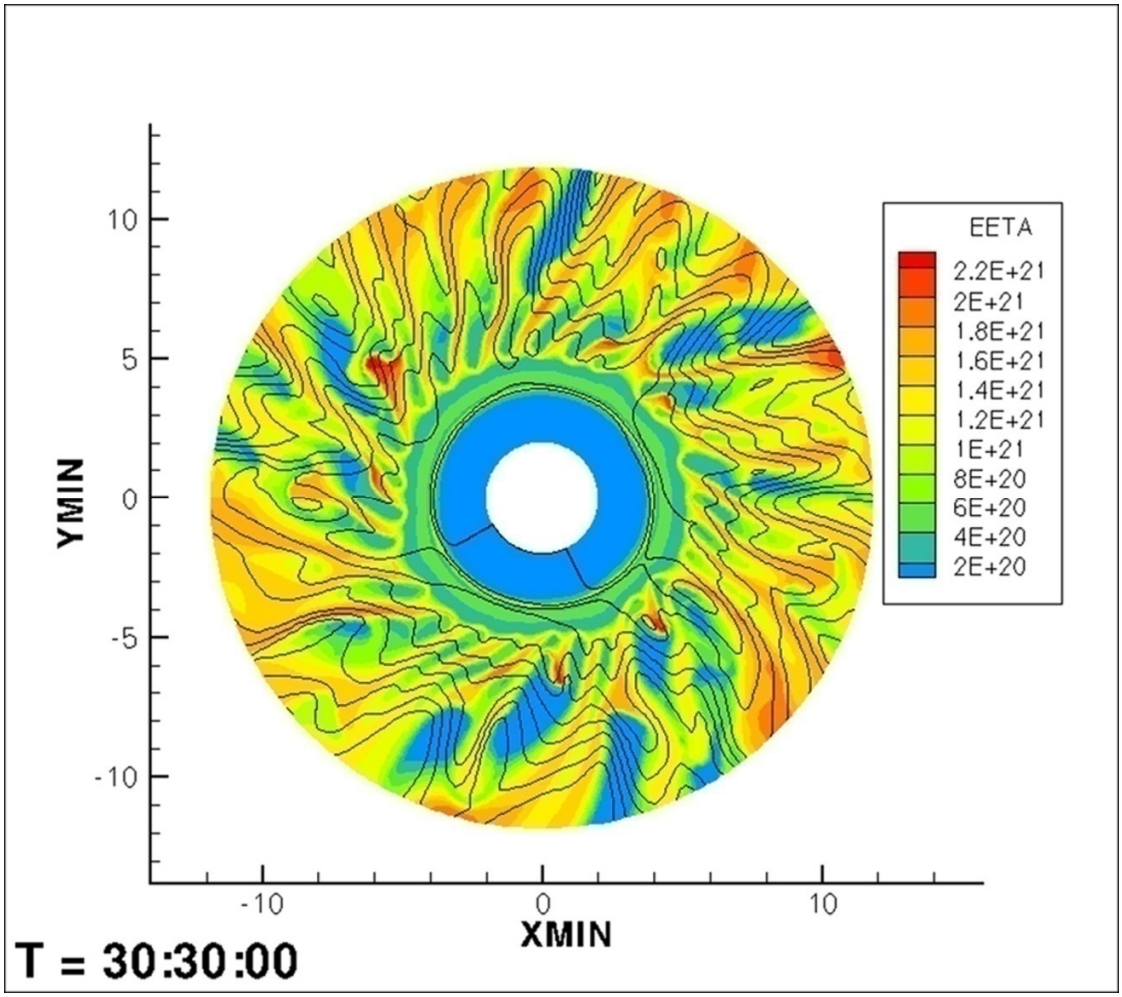

Figure 3.6 Simulated ion content at T = 30.5 hr (same as Figure 3.5f) with equipotential lines (flow streamlines) added at 15 kV intervals.

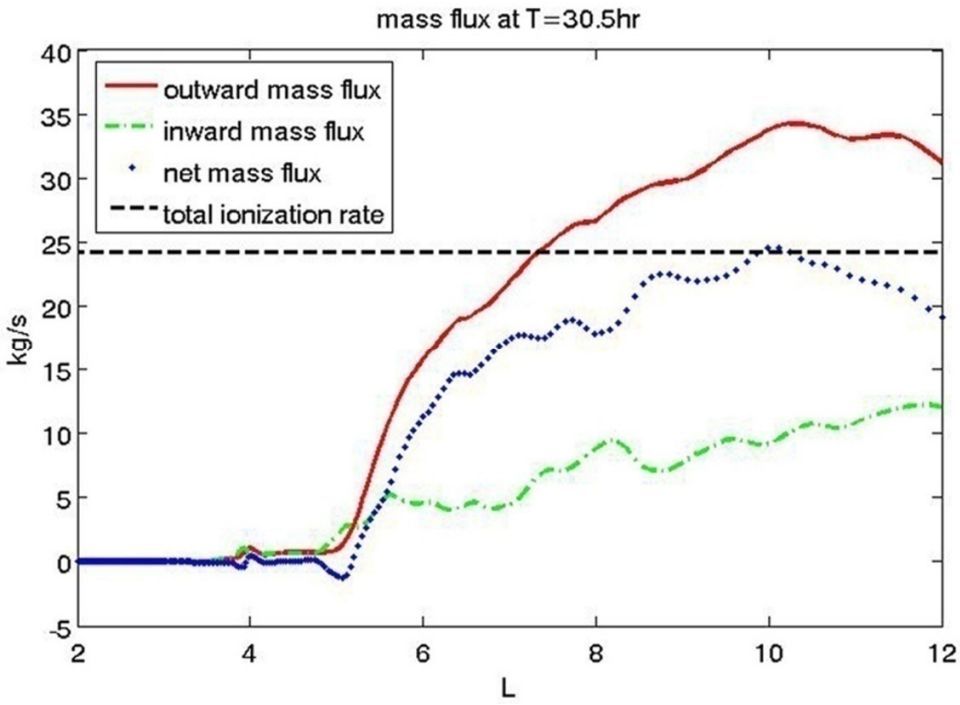

Figure 3.7 Radial plasma mass flux at T = 30.5 hr. The net plasma mass flux almost equals the total ionization rate (24 kg/s).

3.4. Discussion

3.4.1. Longitudinal widths and radial speeds of convection channels

The injection and dispersion events described in the introduction are now widely accepted as direct evidence of plasma radial transport due to the centrifugal interchange instability. Observations indicate that the relatively empty inflow channels occupy only a small fraction (few %) of the available longitude space in the inner magnetosphere [*Chen and Hill*, 2008; *Chen et al.*, 2010]. Figure 3.8 shows a comparison of simulated and observed results regarding the fraction of longitude space occupied by low-density inflow

channels. The three sets of simulation data are averaged from 30.5 to 31 hr, from 31 to 31.5 hr, and from 31.5 to 32 hr, respectively. The simulated and observed curves agree in two important respects: this fraction has a clear peak in the inner magnetosphere, and its average value is clearly less than one half, which is the default value that is assumed for mathematical convenience in most analytic theories [*e.g.*, *Siscoe and Summers*, 1981; *Huang and Hill*, 1991], and also found to be the case in numerical initial-value simulations without an active source [*e.g.*, *Yang et al.*, 1994; Figure 3.4 above]. The shapes of the simulated curves are fairly sensitive to which simulation time is chosen, but there remains a discrepancy in that the simulated curves are more sharply peaked than the observational curve. This discrepancy probably reflects the fact that the source profile adopted in the simulation is too sharply peaked in radial distance, a point to which we return below.

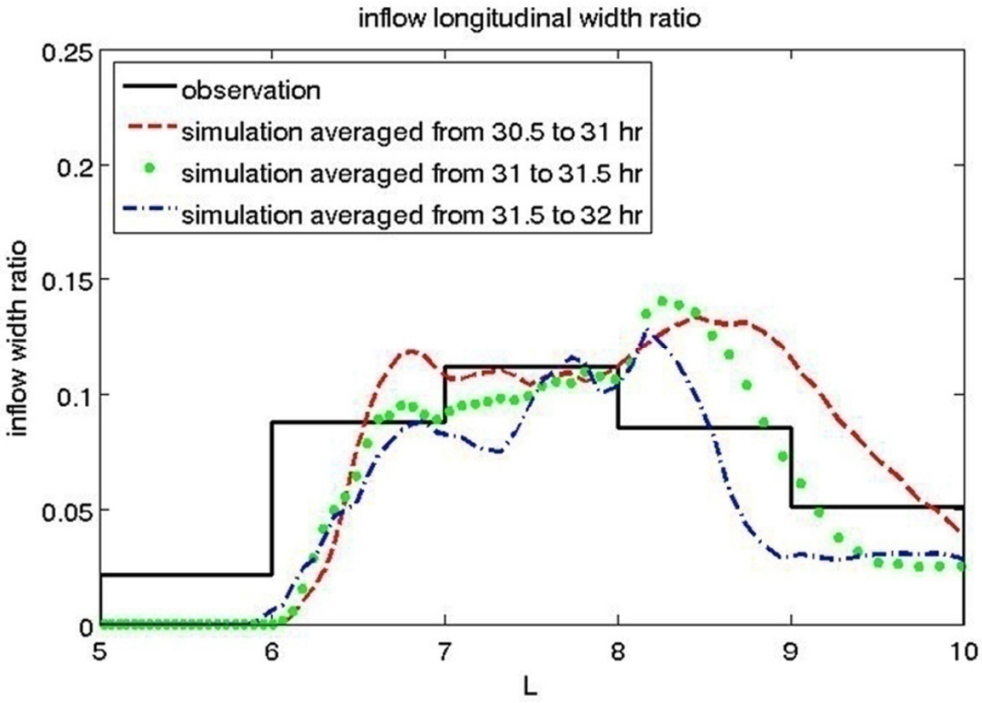

Figure 3.8 Fraction of the available longitude space occupied by inflow channels; simulation results averaged over three late time intervals compared with observed values reported by Chen et al. [2010].

According to Faraday's law, the total potential drop integrated across inflow and outflow channels on a given L shell should be zero in a steady state, or when averaged in time over the time scale of a convection cycle.

$$\nabla \times \mathbf{E} = -\frac{\partial \mathbf{B}}{\partial t} \approx 0 \tag{3.7}$$

with

$$\mathbf{E} + \mathbf{v} \times \mathbf{B} = 0 \tag{3.8}$$

The ratio of average inflow and outflow speeds should thus be the reciprocal of the ratio of inflow and outflow channel widths.

$$\overline{\mathbf{v}}_{\text{inflow}} / \overline{\mathbf{v}}_{\text{outflow}} = w_{\text{outflow}} / w_{\text{inflow}} \tag{3.9}$$

where $\overline{\mathbf{v}}_{\text{inflow}}$ and $\overline{\mathbf{v}}_{\text{outflow}}$ are inflow and outflow radial speeds averaged over longitude, respectively, and w_{outflow} and w_{inflow} are outflow and inflow channel widths, respectively. The average inflow speed should thus be larger than the average outflow speed by a factor ~10. Figure 3.9 shows the longitude-averaged speed within the empty inflow channels in the simulation, compared with the average observationally inferred inflow speed reported by *Chen et al*. [2010]. As in Figure 3.8, the three sets of simulated data are averaged from 30.5 to 31 hr, from 31 to 31.5 hr, and from 31.5 to 32 hr, respectively. Figure 3.10 shows the same comparison for outflow speeds. In all figures, the simulated and observed results have similar shapes and orders of magnitude, and the inflow speed is much larger than the outflow speed.

Vasyliūnas [1994] and *Hill* [2009] have argued theoretically that the radial speed of centrifugally driven magnetospheric convection should not exceed the local corotation speed. This expectation is satisfied by the observational results shown in Figures 3.9 and 3.10 [*Chen et al.*, 2010] and by the simulation results shown there for comparison.

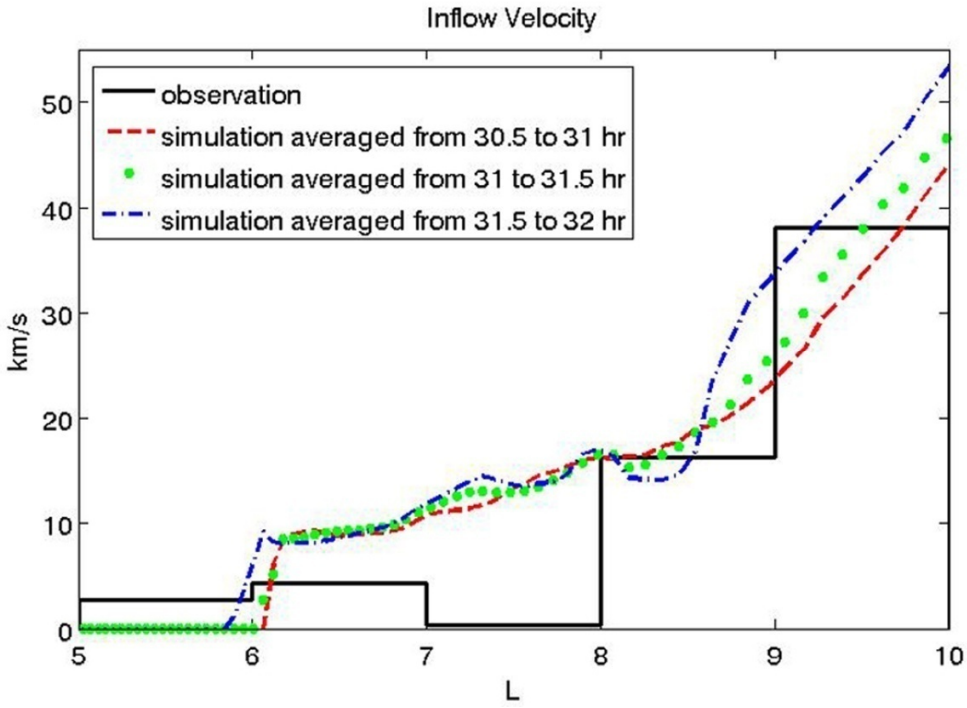

Figure 3.9 Longitudinally averaged inflow velocities; simulation results averaged over three late time intervals compared with values inferred from CAPS observations [Chen et al., 2010].

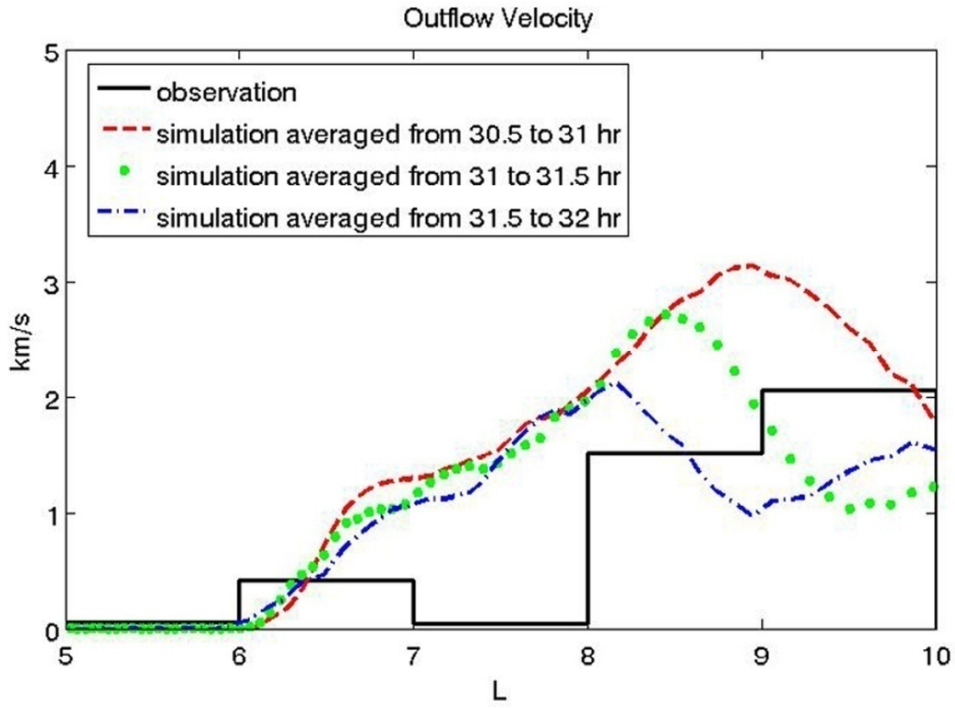

Figure 3.10 Longitudinally averaged outflow velocities; simulation results averaged over three late time intervals compared with observed values reported by Wilson et al. [2008] and averaged within radial bins by Chen et al. [2010].

3.4.2. Corotation lag: relative roles of pickup current and Coriolis acceleration

Saturn's magnetospheric plasma does not corotate rigidly with Saturn's ionosphere. Figure 3.11, reproduced from Figure 1 of *Pontius and Hill* [2009], shows the radial profile of the observed angular velocity of magnetospheric plasma, normalized to rigid corotation, obtained from Cassini CAPS measurements [*Wilson et al.*, 2008, 2009].

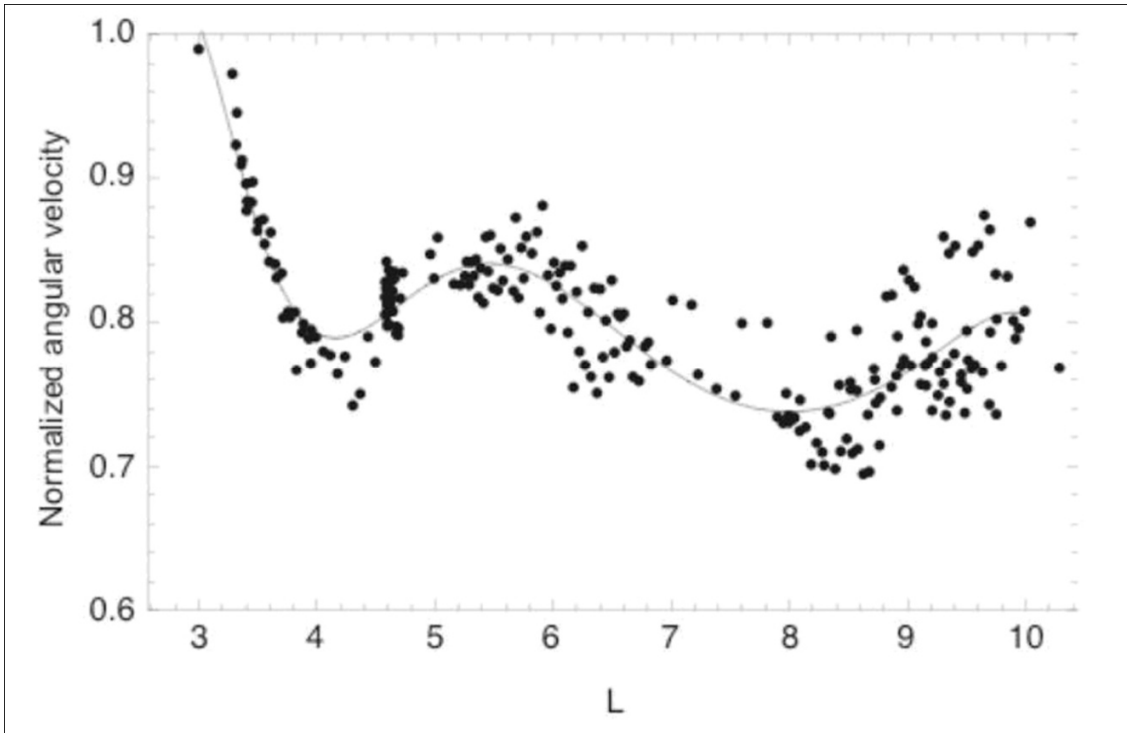

Figure 3.11 Angular velocity versus distance as observed by the Cassini CAPS instrument, normalized to rigid corotation. Data from Wilson et al. [2008, 2009]; figure reproduced from Pontius and Hill [2009].

Because of the widely distributed plasma source in Saturn's inner magnetosphere, the regions wherein the corotation lag is driven by the pickup current and by the Coriolis acceleration are not distinctly separated in radial distance (as they are at Jupiter). However, we can investigate the two effects separately by comparing different simulation times.

The dashed blue line in Figure 3.12 shows the radial profile of the outflow angular velocity, normalized to rigid corotation and averaged over longitude, from the simulation at T = 10 hr. According to Figure 3.5a, no outflow fingers have appeared at this time, which means that the radial velocities are very small and the Coriolis effect is

correspondingly small. Therefore the corotation lag shown by the dashed blue line in Figure 3.12 is primarily caused by the pickup effect. The solid red line in Figure 3.12 is taken from simulation results at T = 30.5 hr, after the outflow fingers are well developed, so that both the pickup effect and the Coriolis acceleration contribute to the corotation lag. The difference between the dashed blue and solid red lines in Figure 3.12 indicates that the corotation lag in the region $L < 5$ is caused almost exclusively by the pickup effect, while in the region $L > 5$, both the pickup effect and the Coriolis acceleration contribute comparably to the corotation lag. The fact that the peak values of corotation lag near $L = 4$ in Figure 3.12 agree with the value ~0.8 in Figure 3.11 (based on observations) indicates that the peak value at $L = 4$ of the charge-exchange rate of the adopted plasma source model (solid line in Figure 3.2) is acceptable near $L = 4$ where charge-exchange dominates the pick-up current.

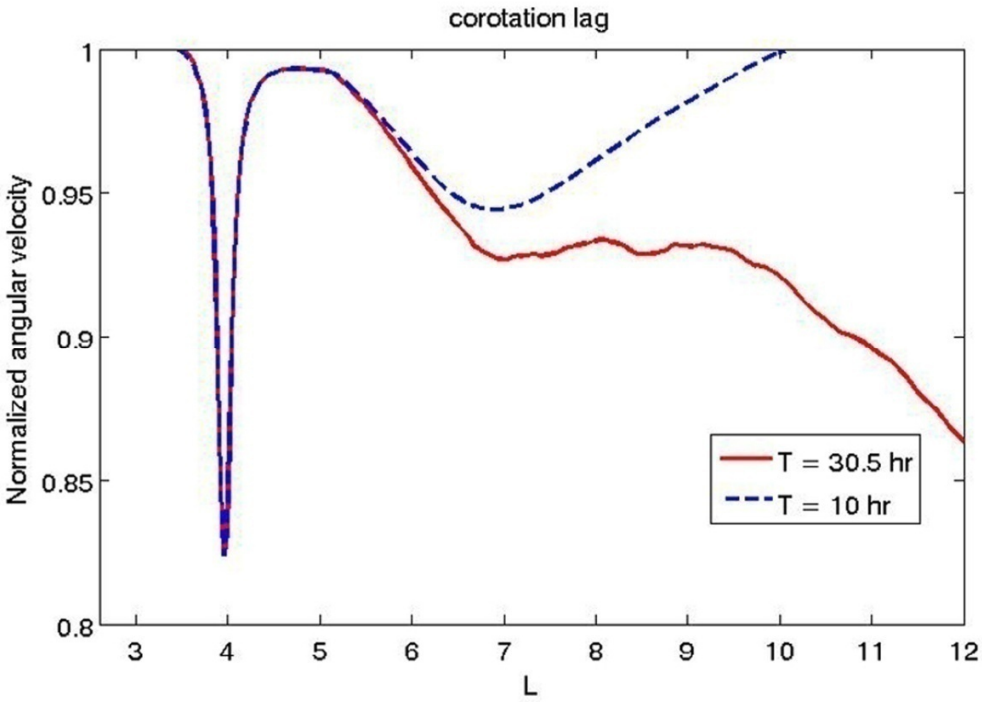

Figure 3.12 Simulated angular velocity at T = 10 hr (before radial flow fingers appear) and T = 30.5 hr (after radial flow fingers are well developed), normalized to rigid corotation and averaged over longitude.

However, the peak at $L = 4$ in Figure 3.12 is narrower than that in Figure 3.11. One possible explanation is that the shape of the charge-exchange peak at $L = 4$ should be wider than in the model we have adopted.

Pontius and Hill [2009] presented an analytical model to derive the plasma source rate from the observed corotation lag shown in Figure 3.11. Their model assumes that the L-dependent ratio of new ionization rate to charge exchange rate is the same as in the *Johnson et al.* [2006] model on which our input model (Figure 3.2) is based. Their resulting plasma source model shows a wider peak of the charge-exchange rate at $L = 4$, consistent with our conclusion above. In the more distant region $L > 5$, the simulated

corotation lag in Figure 3.12 is consistently smaller than that in the observation-based Figure 3.11. Because the new-ionization effect (dashed line in Figure 3.2) dominates in this region, a plausible explanation for this discrepancy is that the new ionization rate we have adopted (Figure 3.2) is too small. Further evidence for this conclusion is provided by the fact that, when we integrate the ionization rate in Figures 3.2 over radial distance, we obtain a global new ionization rate ~24 kg/s between 2 and 12 R_S, which is smaller than the observationally-based inferences ~100 kg/s [*Pontius and Hill*, 2006] and ~280 kg/s [*Chen et al.*, 2010].

3.5. Summary

We have used the numerical model RCM-S to simulate plasma transport in Saturn's inner magnetosphere ($2 < L < 12$), incorporating a continuously active distributed plasma source adopted from neutral-cloud theory, and including the Coriolis acceleration and the pickup current. The simulation results indicate that, after new plasma accumulates for several hours in the radial range of maximum source, outflow fingers appear as a result of the centrifugal interchange instability. As the fingers develop outward, they are bent in the retrograde direction and their growth is regulated by the Coriolis force and the pickup current, in agreement with theoretical predictions. In the later stages of the simulation (T~30.5 hr), the inflow channels become much narrower than the outflow ones, consistent with observational results. After this time, the simulation reaches a quasi-steady state in the sense that, although the details of the flow pattern continue to change chaotically in time, its statistical properties do not.

Post-processing analysis of the simulation results indicates that the radial speeds of the inflow channels become much faster than those of the outflow channels, while both of them remain much smaller than the local partial corotation speed. The ratio of inflow and outflow channels' average longitudinal widths is almost the reciprocal of the ratio of inflow and outflow speeds, as expected from Faraday's law in steady state coupled with ideal MHD. The simulation results thus conform to a key feature of CAPS observations, that convection in Saturn's inner magnetosphere comprises narrow but fast inflow channels interspersed between wider but slower outflow channels.

Comparison of the corotation lags before and after the formation of radial flow channels clarifies the relative roles of the Coriolis force and the pickup current in producing the corotation lag. In the near region $L < 5$, the corotation lag is produced almost exclusively by the pickup effect, while in the more distant region $L > 5$, the corotation lag is produced by a combination of the pickup effect and the Coriolis force. The magnitude and radial profile of the corotation lag are qualitatively similar to those of the observed lag, but the plasma source model, adopted as input, needs refinement in order to improve the fit with the observed lag.

Chapter 4

Interior plasma source models

The initial simulation described in Chapter 3 only considers the cool plasma from the interior source. The numerical model RCM-S by now has only two inputs: ionospheric conductance and interior plasma source. The ionospheric conductance serves to confine the growth rate of the plasma convection, and is simply set to be uniform and constant (Σ_p = 0.3 S, Σ_H = 0). The interior plasma source therefore plays a key role in the plasma convection pattern.

4.1. 10X J06 model

4.1.1. Source model and Pedersen conductance

In Chapter 3, we used an interior plasma source based on the neutral cloud model of *Johnson et al.* [2006] (we called it the J06 source model). The J06 source model, however, has a total mass loading rate of only ~24 kg/s. More recent plasma source

models [*Smith et al.* 2010, *Cassidy and Johnson*, 2010] suggest a larger mass loading rate ~150 kg/s. Moreover, *Chen et al.* [2010] analyzed CAPS observational data and estimated a global plasma mass outflow rate ~280 kg/s from Saturn's inner magnetosphere. We therefore scale the J06 plasma source model upward by a factor 10 to ~240 kg/s to agree with present observational and model estimates. Figure 4.1 shows the interior source model after scaling up 10 times (10X J06 source model). The solid and dashed curves are radial profiles of charge exchange rate and ionization rate per unit equatorial area, respectively. Figure 4.2 shows the ionization rate per unit equatorial area (solid line with left Y-axis) and per unit magnetic flux (dashed line with the right Y-axis).

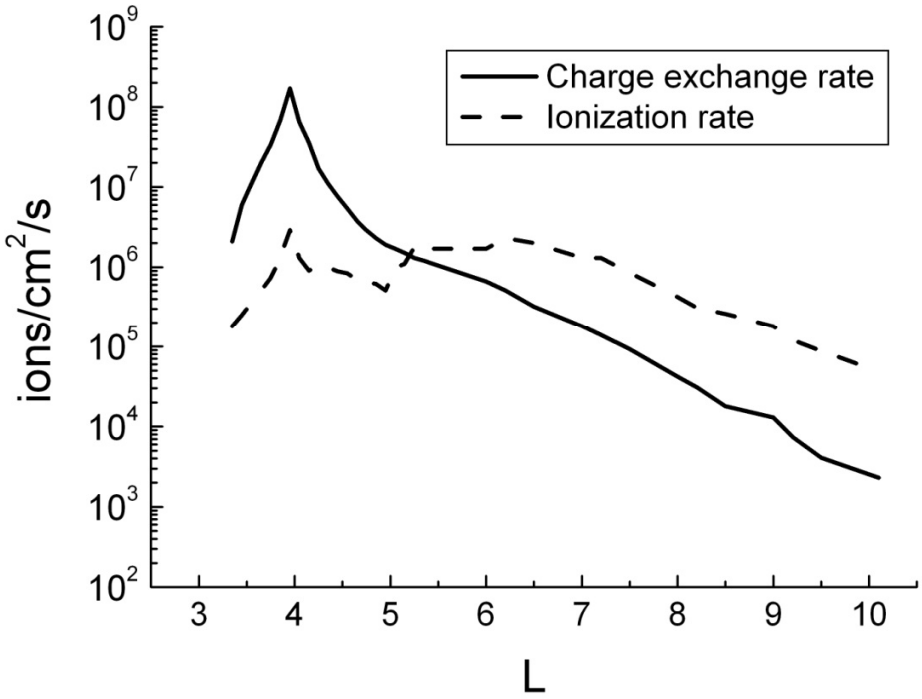

Figure 4.1 Interior plasma source model obtained by scaling the J06 model upward by a factor 10 (10X J06 model). Solid and dashed curves are charge exchange rate and ionization rate per unit equatorial area, respectively.

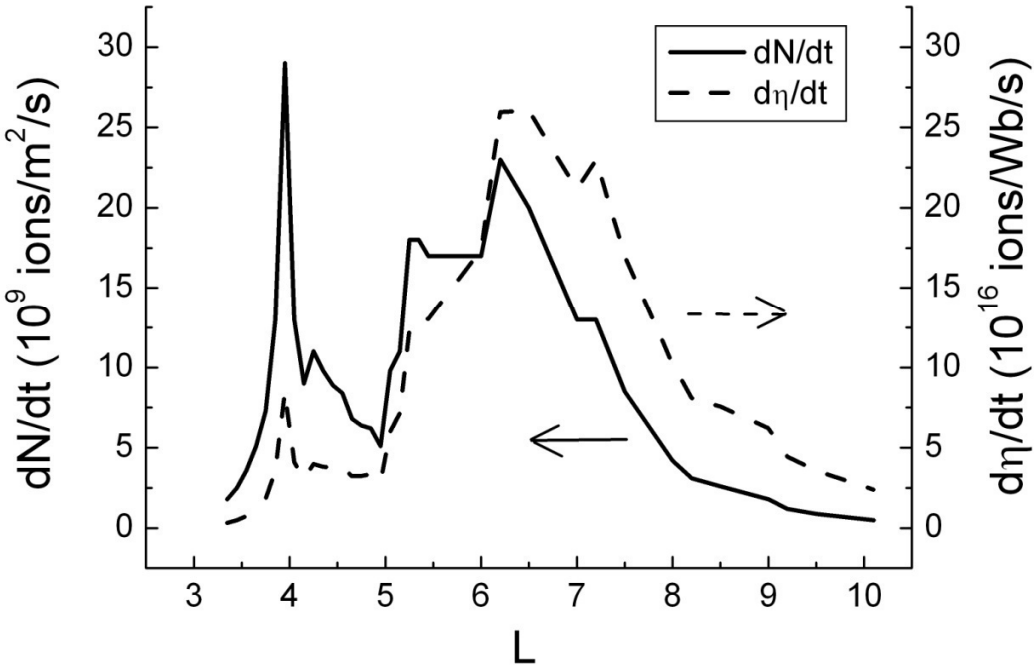

Figure 4.2 Ionization rate of 10X J06 plasma source model. Solid curve is rate per unit equatorial area. Dashed curve is rate per unit magnetic flux.

We also scale the ionospheric Pedersen conductance Σ_p upward by the same factor 10 to keep the simulated radial flow speeds within the observational bounds established by *Chen et al*. [2010]. This increased value of Σ_p is in fact closer to the bounds established by the observation-based aeronomy model results of *Moore et al.* [2010]. On the left side of (2.1), η is updated by the ionization rate every time step, and $\dot{\eta}_s$ is the addition of charge exchange rate and ionization rate. Thus $\mathbf{J}_{\perp e}$ is proportional to the plasma source. In (2.5), Σ_p is proportional to $\mathbf{J}_{\perp e}$, providing Σ_H is assumed to be

zero. Therefore, the impact of changing the plasma source strength is counteracted by changing the ionospheric Pedersen conductance in the same way. Though there are some differences in the details of the convection pattern, which includes an element of chaos, these are not large enough to change the statistical results significantly.

4.1.2. Simulation results

The new simulation with 10X J06 source model and Σ_p = 3.0 S is shown in Figure 4.3. Like Figure 3.5, the six panels here show six representative stages of the evolution: pre-appearance of outflow fingers, appearance of outflow fingers, developing, further developing, pre-mature, and mature. Compared with Figure 3.5, the outflow fingers appear about 1 hour earlier in Figure 4.3 (panels b and c). But in later development, the differences diminish as the convection evolves (panels d and e). Finally, the convection reaches a quasi-steady state at ~30.5 hr (panel f), the same time as in Figure 3.5. Figure 4.4 shows the plasma mass flux at 30.5 hr to verify that the net plasma flux equals the total ionization rate (~240 kg/s) near the outer boundary at L = 12.

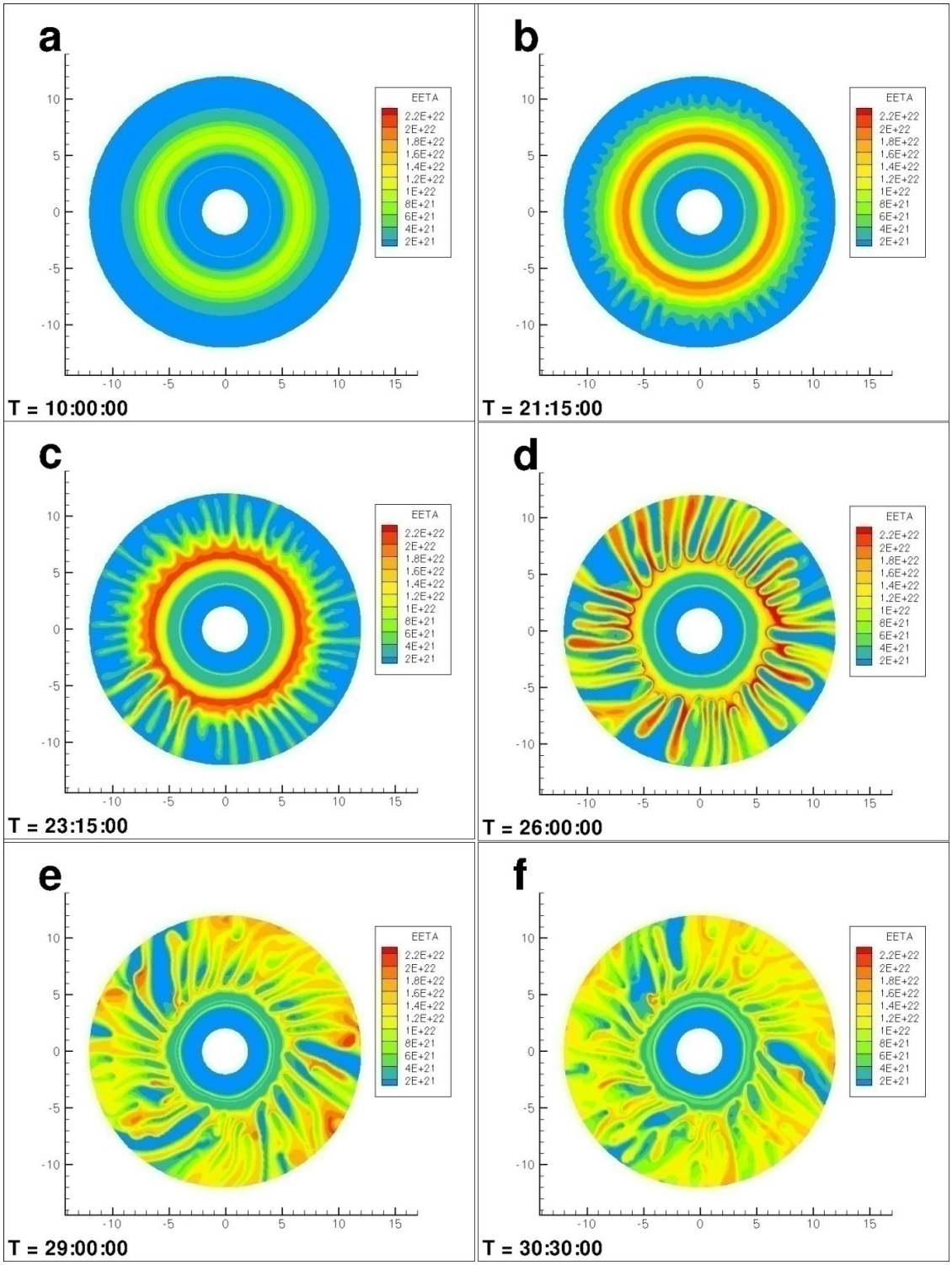

Figure 4.3 Simulation with 10X J06 source model and Σ_P = 3.0 S. Six panels show similar evolution stages as those in Figure 3.5: pre-appearance of outflow fingers,

appearance of outflow fingers, developing, further developing, pre-mature, and mature. The simulation here differs from the previous one (shown in Figure 3.5) in some details, but the convection pattern is basically the same.

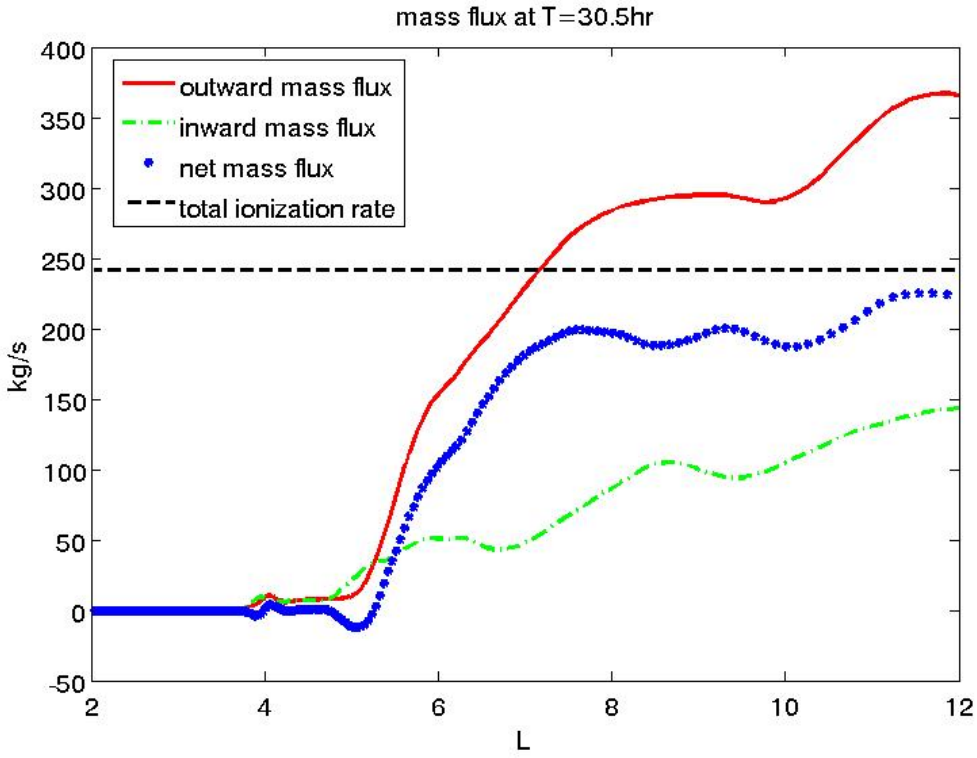

Figure 4.4 Radial plasma mass flux at T = 30.5 hr. The net plasma mass flux almost equals the total ionization rate (240 kg/s). (Simulation with 10X J06 source model and Σ_P = 3.0 S)

Post-processing analysis also confirms the similarity between the two simulations. Figure 4.5 shows the inflow longitudinal width ratio. Figures 4.6 and 4.7 show the inflow and outflow velocities averaged over longitude. In these figures, the three colored lines represent three sets of simulated data averaged from 30.5 to 31 hr, from 31 to 31.5 hr, and

from 31.5 to 32 hr, respectively. The simulated results agree with the observed results [*Chen et al*., 2010]. Figures 4.5, 4.6, and 4.7 also agree with Figures 3.8, 3.9, and 3.10, respectively.

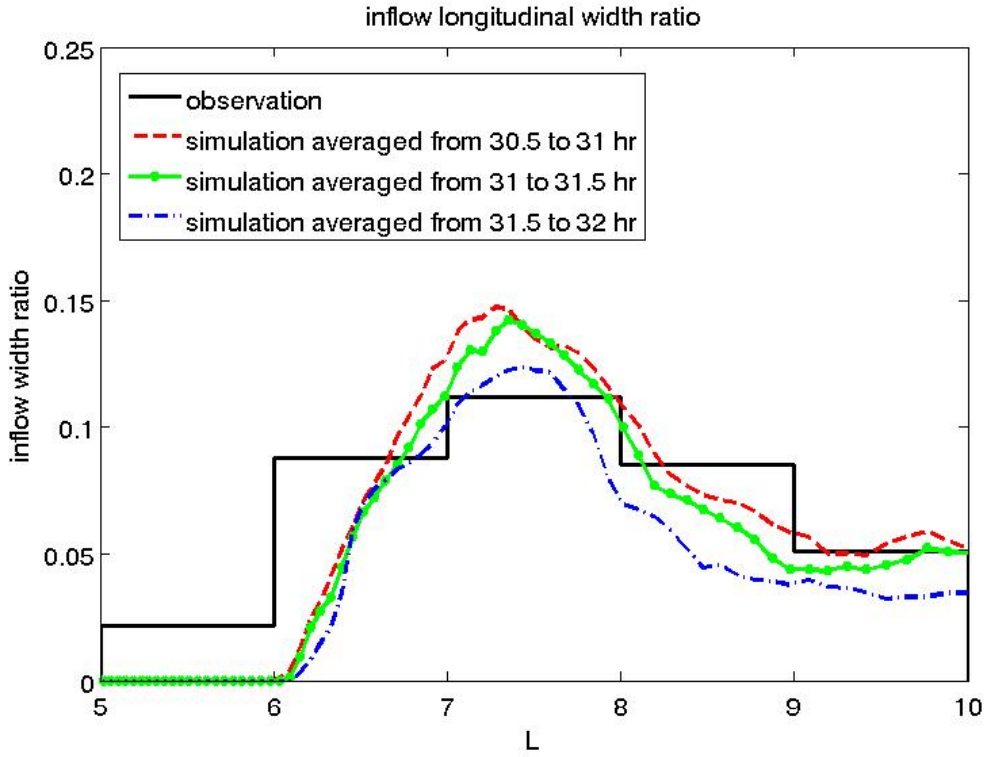

Figure 4.5 Fraction of the available longitude space occupied by inflow channels; simulation results averaged over three late time intervals compared with observed values reported by Chen et al. [2010]. (Simulation with 10X J06 source model and Σ_P = 3.0 S)

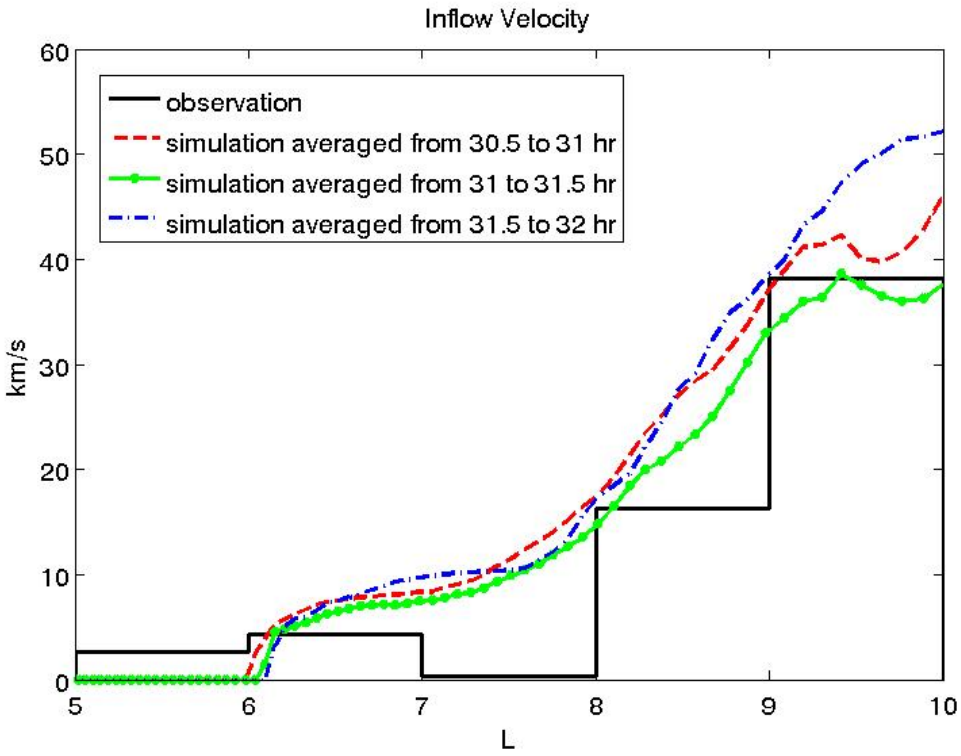

Figure 4.6 Longitudinally averaged inflow velocities; simulation results averaged over three late time intervals compared with values inferred from CAPS observations [Chen et al., 2010]. (Simulation with 10X J06 source model and Σ_P = 3.0 S)

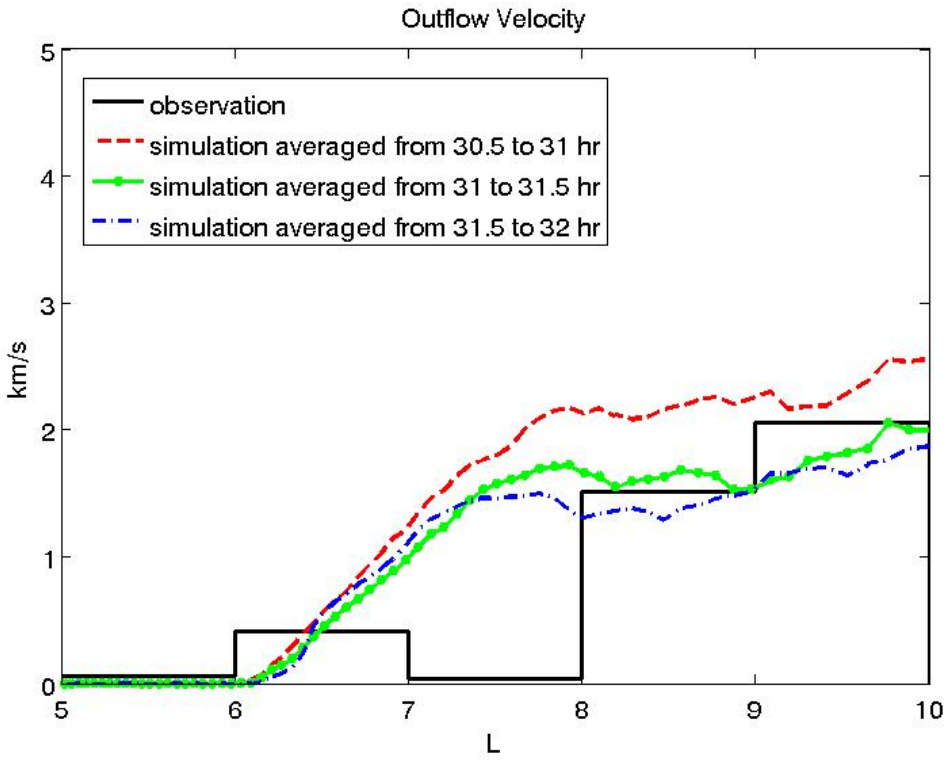

Figure 4.7 Longitudinally averaged outflow velocities; simulation results averaged over three late time intervals compared with observed values reported by Wilson et al. [2008] and averaged within radial bins by Chen et al. [2010]. (Simulation with 10X J06 source model and Σ_p = 3.0 S)

4.2. Two other source models

4.2.1. S10E3 and CJ10 source models

Smith et al. [2010] and *Cassidy and Johnson* [2010] proposed their own plasma source models. We have tried both of them in RCM-S. Although the simulations with the two more recent source models are not as good as those with 10X J06 source model, their results might be useful in improving the plasma source model in the future.

Smith et al. [2010] used CAPS and Cassini magnetospheric imaging instrument observations to update neutral particle lifetimes, and used the more recently processed versions of Cassini ion and neutral mass spectrometer (INMS) observations made during encounters E2, E3, and E5 to constrain a 3-D multispecies neutral particle model. They show that the neutral lifetimes have minima near $L = 9$, mostly caused by electron impact with warmer (>~ 10 eV) electrons [*Smith et al.,* 2010, Figure 2]. They also show that neutral densities vary greatly between different Enceladus encounters. We take their neutral densities based on E3, because the resulting plasma mass loading rate for that encounter is ~150 kg/s, which is closest to the estimation (~280 kg/s) of *Chen et al.* [2010]. For each neutral species (H_2O, OH and O), dividing the neutral densities [*Smith et al.,* 2010, Figure 6] by the neutral lifetimes [*Smith et al.,* 2010, Figure 2] and adding up the contributions of each species, we have the charge exchange rate and the ionization rate shown in Figure 4.8, which we call the S10E3 plasma source model. Figure 4.9 shows the ionization rate per unit equatorial area and per unit magnetic flux.

Cassidy and Johnson [2010] showed similar results. The neutral lifetimes also have minima near $L = 9$ [*Cassidy and Johnson*, 2010, Figure 3]. The charge exchange rate and the ionization rate from their results are shown in Figure 4.10, which we call the CJ10 plasma source model. The total mass loading rate is ~160 kg/s. Figure 4.11 shows the ionization rate per unit equatorial area and per unit magnetic flux.

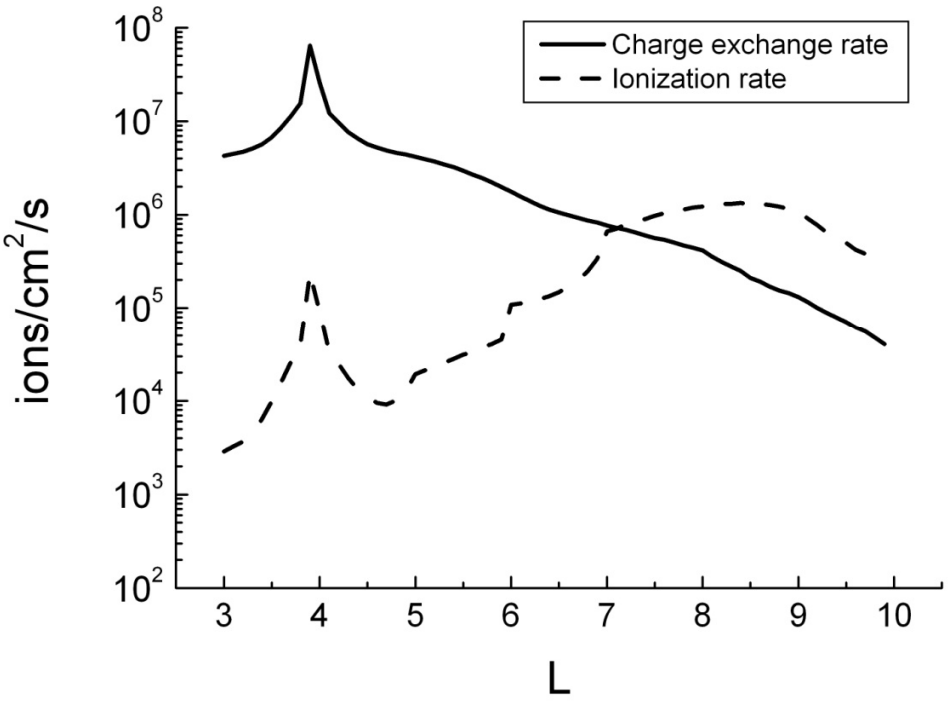

Figure 4.8 S10E3 plasma source model obtained from Smith et al. [2010]. Solid and dashed curves are charge exchange rate and ionization rate per unit equatorial area, respectively.

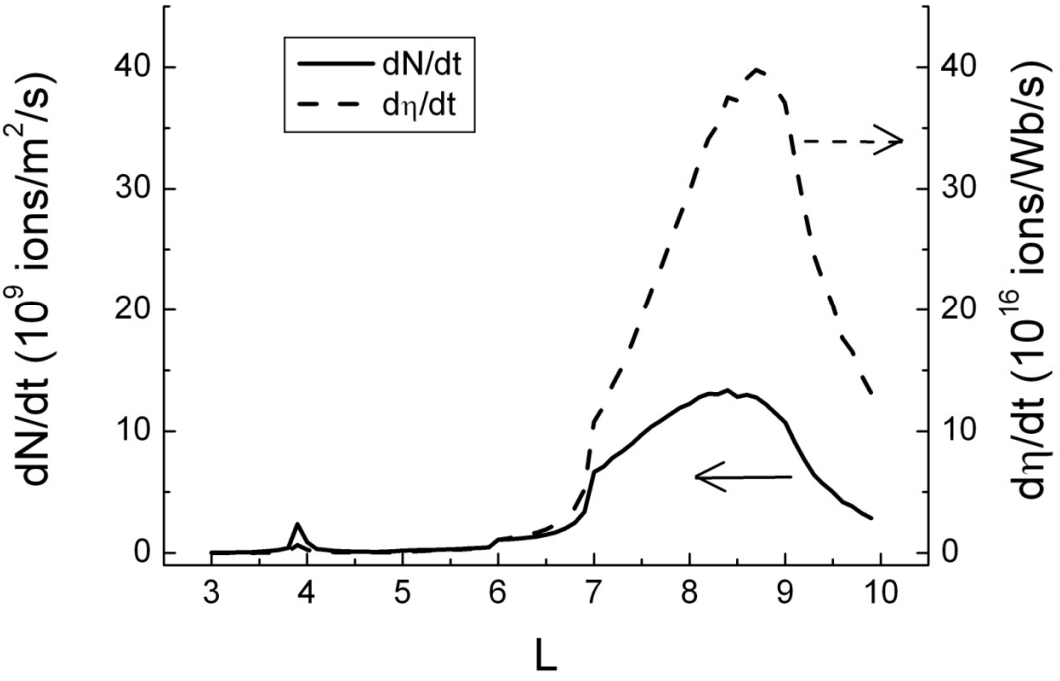

Figure 4.9 Ionization rate of S10E3 plasma source model. Solid curve is rate per unit equatorial area. Dashed curve is rate per unit magnetic flux.

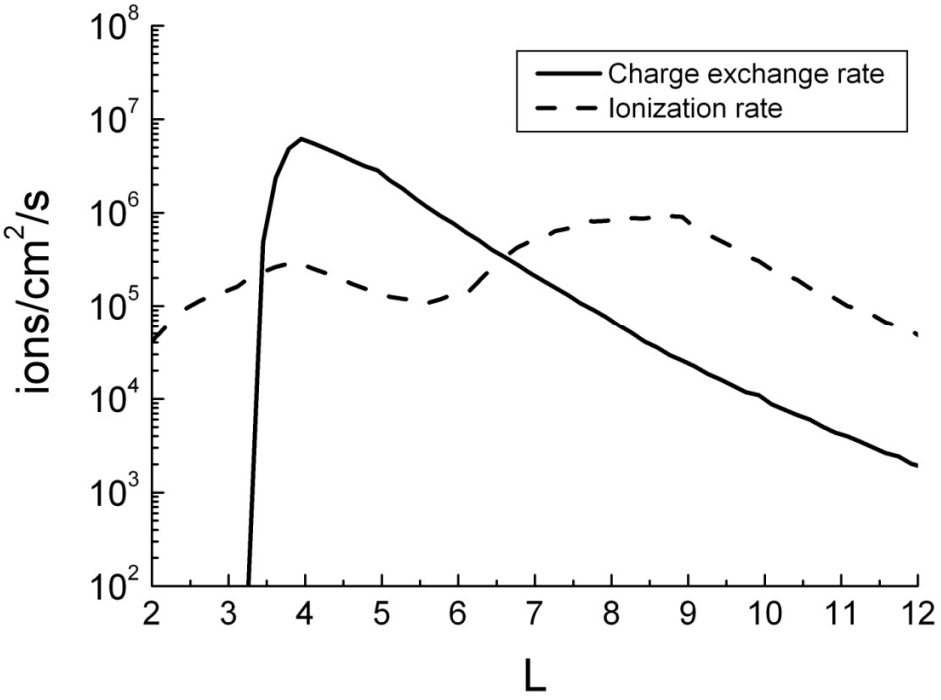

Figure 4.10 CJ10 plasma source model obtained from Cassidy and Johnson [2010]. Solid and dashed curves are charge exchange rate and ionization rate per unit equatorial area, respectively.

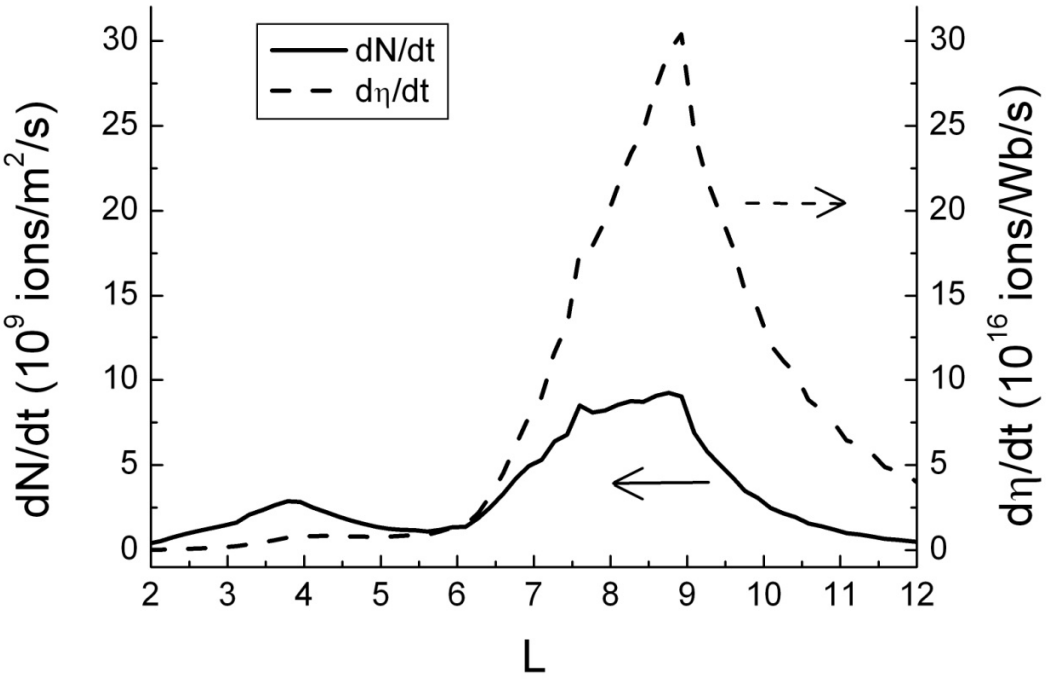

Figure 4.11 Ionization rate of CJ10 plasma source model. Solid curve is rate per unit equatorial area. Dashed curve is rate per unit magnetic flux.

The S10E3 and CJ10 source models are similar to each other, but both of them are different from the 10X J06 model. In the 10X J06 model, the ionization rate starts to dominate the charge exchange rate at L = 5.2 (Figure 4.1). These crossover points are at L = 7 in the S10E3 model (Figure 4.8) and at L = 6.7 in the CJ10 model (Figure 4.10). Looking at the ionization rate per unit magnetic flux, the second peak is located at L = 6.5 in the 10X J06 model (Figure 4.2). But in the S10E3 (Figure 4.9) and CJ10 (Figure 4.11) models, the second peaks of the ionization rate are further out at L = 8.8, and much larger. These discrepancies could cause different convection patterns in the simulation.

In the following simulations with S10E3 and CJ10 source models, the Pedersen conductance is scaled to $\Sigma_p = 2.0$ S.

4.2.2. Simulation results

Figure 4.12 shows the simulation with the S10E3 source model. Notice that the color bar is also scaled according to the total mass loading rate. In panel a, the plasma accumulates and forms a torus which is further out than that in Figure 4.3. The reason is obviously the larger and more distant second peak of the ionization rate of the S10E3 model. Panel b shows that outflow fingers appear in the region beyond $L = 8.8$, which is also the location of the second peak of the ionization rate. It is consistent with the fact that the Rayleigh-Taylor instability can only happen in the region where the direction of the driving force is opposite to the gradient of the density, as discussed in section 1.3.1. Panel c shows the early development of outflow fingers. Those fingers appear to be bent counterclockwise. They are actually not. In the rotating frame, both the heads and the roots of the fingers are lagged in the corotation direction and are therefore moving clockwise. However, the corotation lag of the fingers' heads is smaller than that of the fingers' roots, and this fact causes the visual delusion. The corotation lag of the fingers' heads is caused by both Coriolis and pickup effects, as discussed in Chapter 3.4.2. But the Coriolis effect is small because the radial velocities are small in the early developing stage. The pickup effect is also small in the region where both charge exchange rate and ionization rate are small. The corotation lag of the fingers' roots is caused by the pickup effect, which is large because of the large second peak of the ionization rate at $L = 8.8$. In the late development shown in panel d, the corotation lag of the fingers' heads exceeds

that of the fingers' roots because of the large radial velocities and the resulting large Coriolis effect. The simulation reaches a quasi-steady state at 14 hr, which is much earlier than the 30.5 hr in Figure 4.3. The reason is that the second peak of the ionization rate is much larger in the S10E3 model, and the convection pattern evolves much faster. Figure 4.13 shows the plasma mass flux at 14 hr.

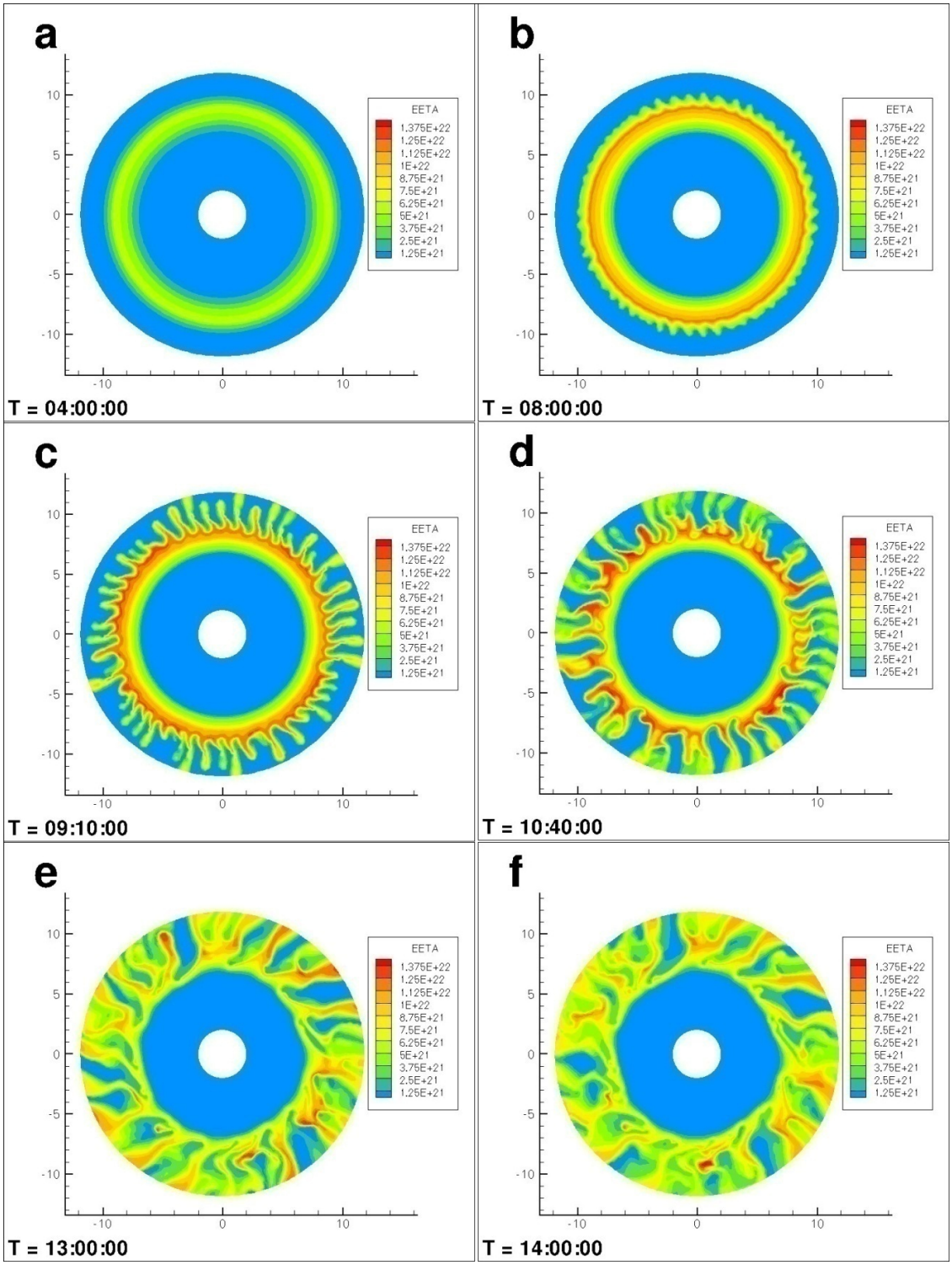
a
b
c
d
e
f
EETA
1.375E+22
1.25E+22
1.125E+22
1E+22
8.75E+21
7.5E+21
6.25E+21
5E+21
3.75E+21
2.5E+21
1.25E+21
T = 04:00:00
T = 08:00:00
T = 09:10:00
T = 10:40:00
T = 13:00:00
T = 14:00:00

Figure 4.12 Simulation with S10E3 plasma source model and Σ_P = 2.0 S. The location of the convection is further out and the growth rate is much larger than those of the simulation with 10X J06 model (Figure 4.3).

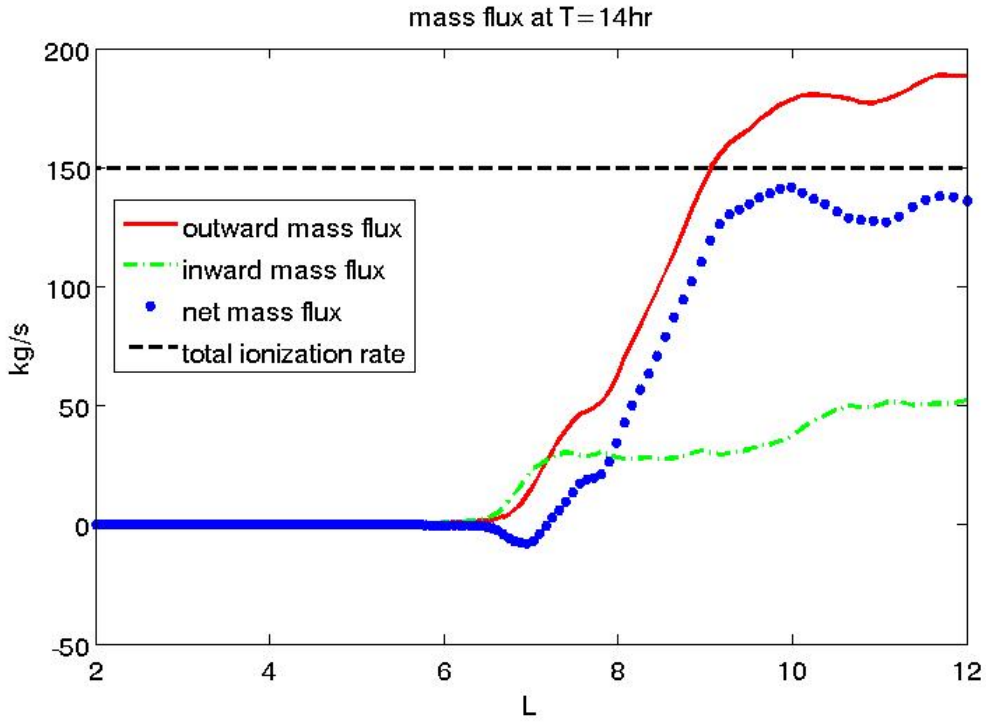

Figure 4.13 Radial plasma mass flux at T = 14 hr. The net plasma mass flux almost equals the total ionization rate (150 kg/s). (Simulation with S10E3 source model and Σ_P= 2.0 S)

Post-processing analysis also confirms the discrepancies between Figures 4.3 and 4.12. Figure 4.14 shows the inflow longitudinal width ratio. Figures 4.15 and 4.16 show the inflow and outflow velocities averaged over longitude. In these figures, the three colored lines represent three sets of simulated data averaged from 14 to 14.5 hr, from

14.5 to 15 hr, and from 15 to 15.5 hr, respectively. The simulated results do not match the observed results.

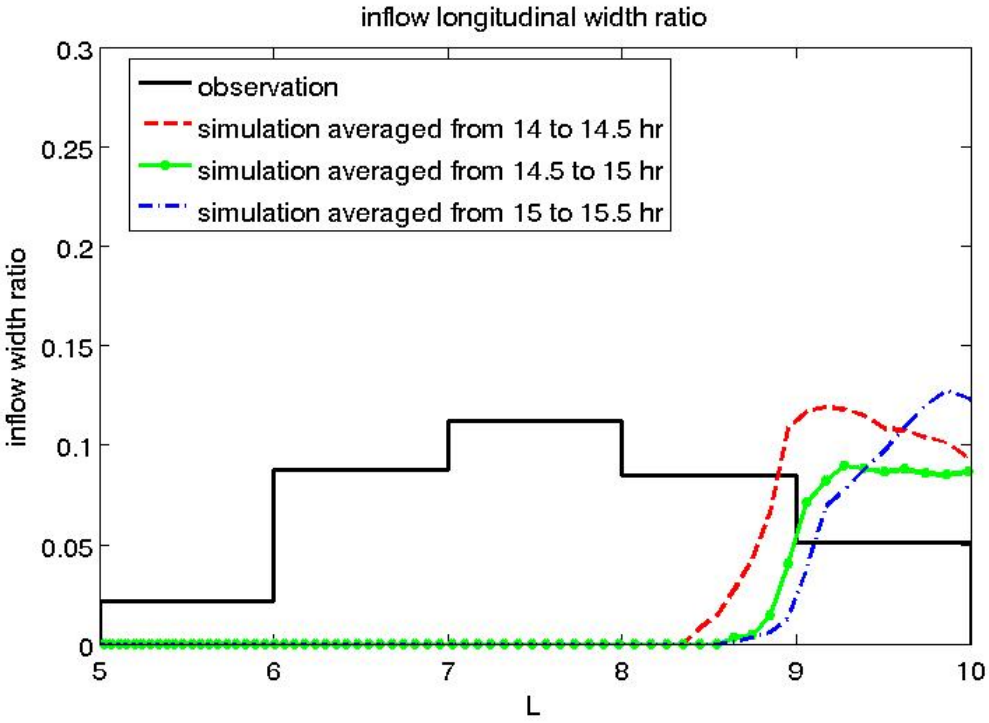

Figure 4.14 Fraction of the available longitude space occupied by inflow channels. (Simulation with S10E3 source model and $\Sigma_P = 2.0$ S)

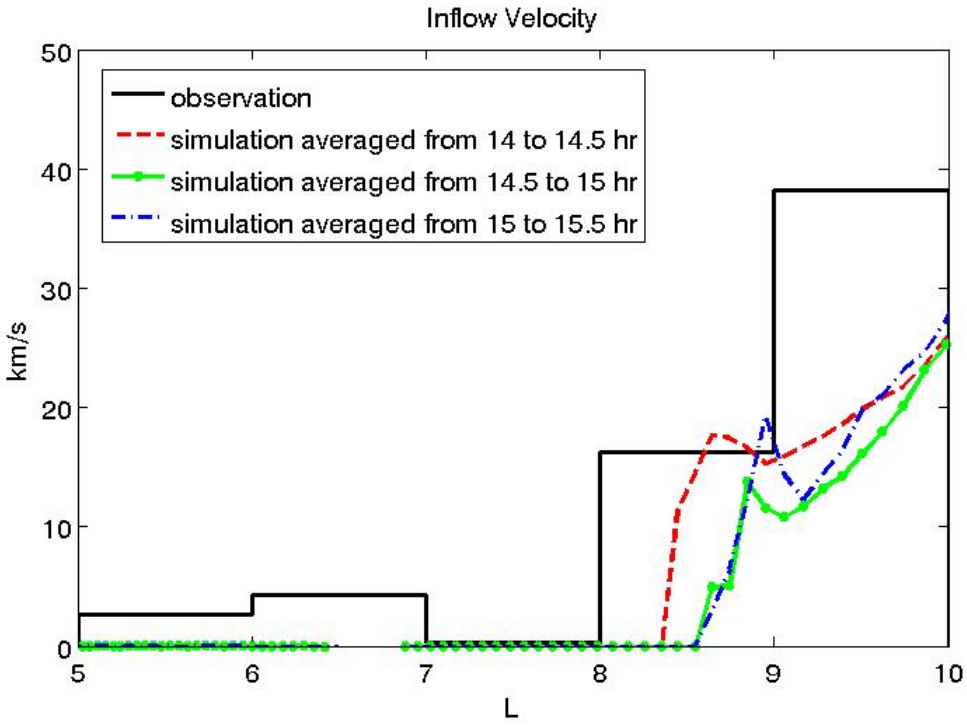

Figure 4.15 Longitudinally averaged inflow velocities. (Simulation with S10E3 source model and $\Sigma_P = 2.0$ S)

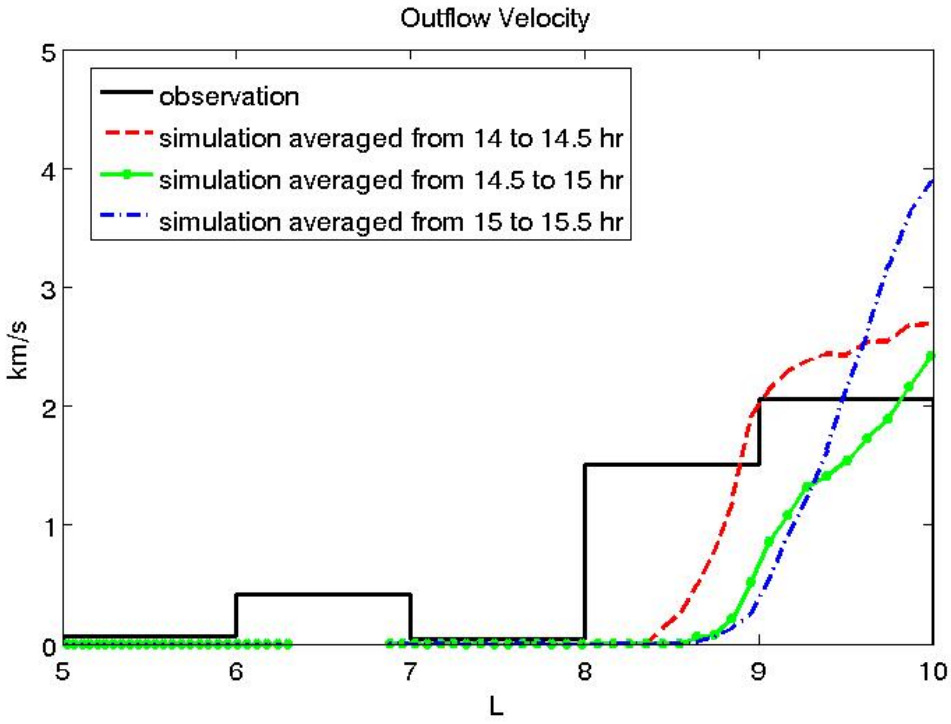

Figure 4.16 Longitudinally averaged outflow velocities. (Simulation with S10E3 source model and $\Sigma_P = 2.0$ S)

The CJ10 plasma source model is similar to the S10E3 source model. The simulation results are also similar. Figure 4.17 shows the simulation with the CJ10 source model, which reaches a quasi-steady state at 17 hr. Figure 4.18 shows the plasma mass flux at 17 hr. Figure 4.19 shows the inflow longitudinal width ratio. The three sets of simulated data are averaged from 17 to 17.5 hr, from 17.5 to 18 hr, and from 18 to 18.5 hr, respectively. Figures 4.20 and 4.21 show the inflow and outflow velocities averaged over longitude.

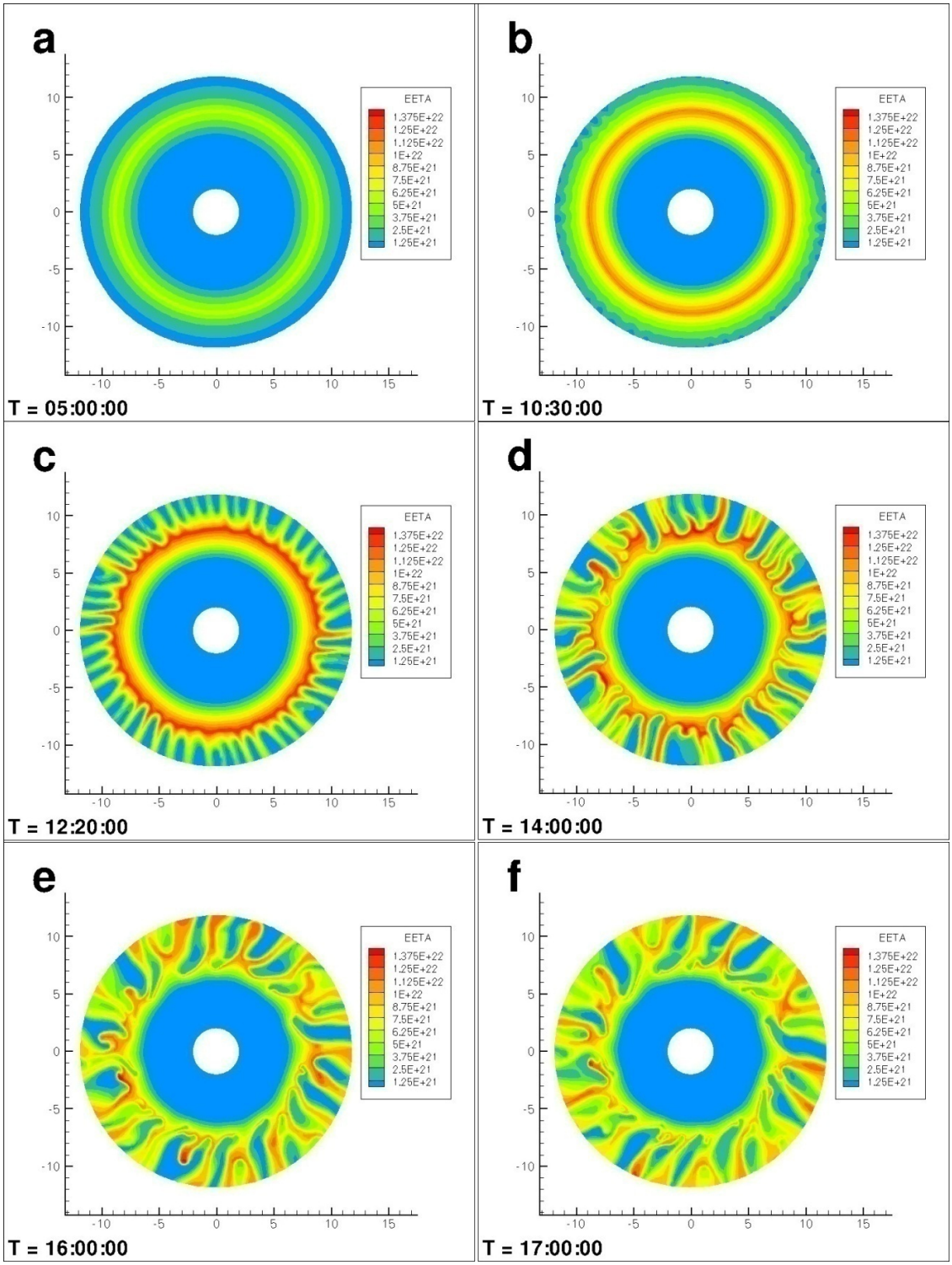

Figure 4.17 Simulation with CJ10 plasma source model and Σ_P = 2.0 S.

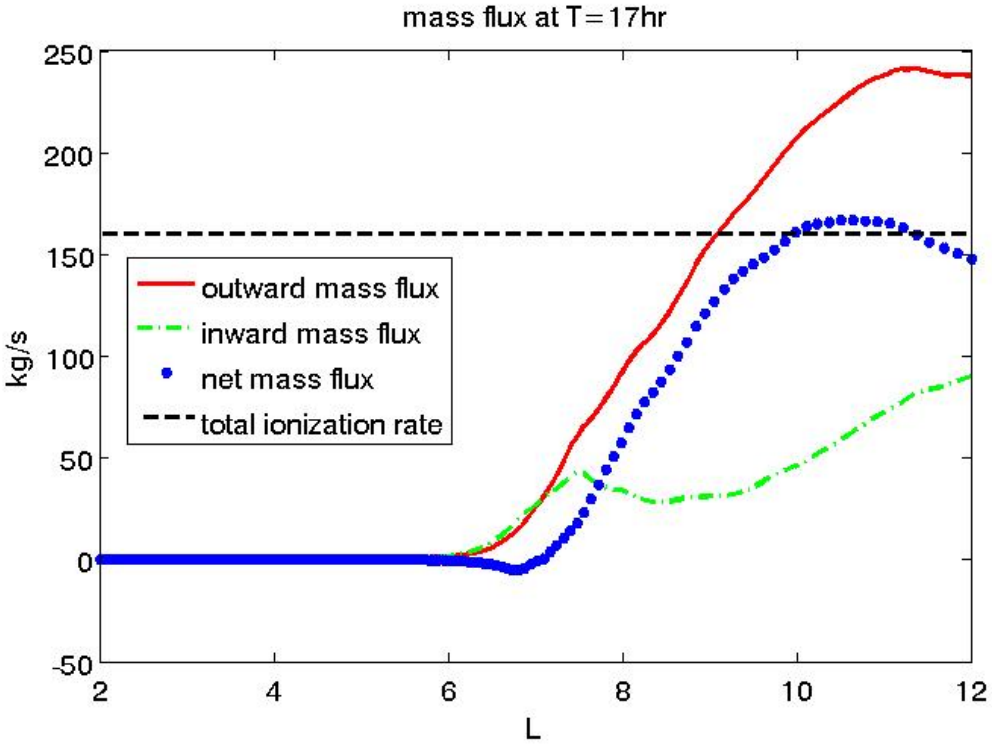

Figure 4.18 Radial plasma mass flux at T = 17 hr. The net plasma mass flux almost equals the total ionization rate (160 kg/s). (Simulation with CJ10 source model and Σ_P = 2.0 S)

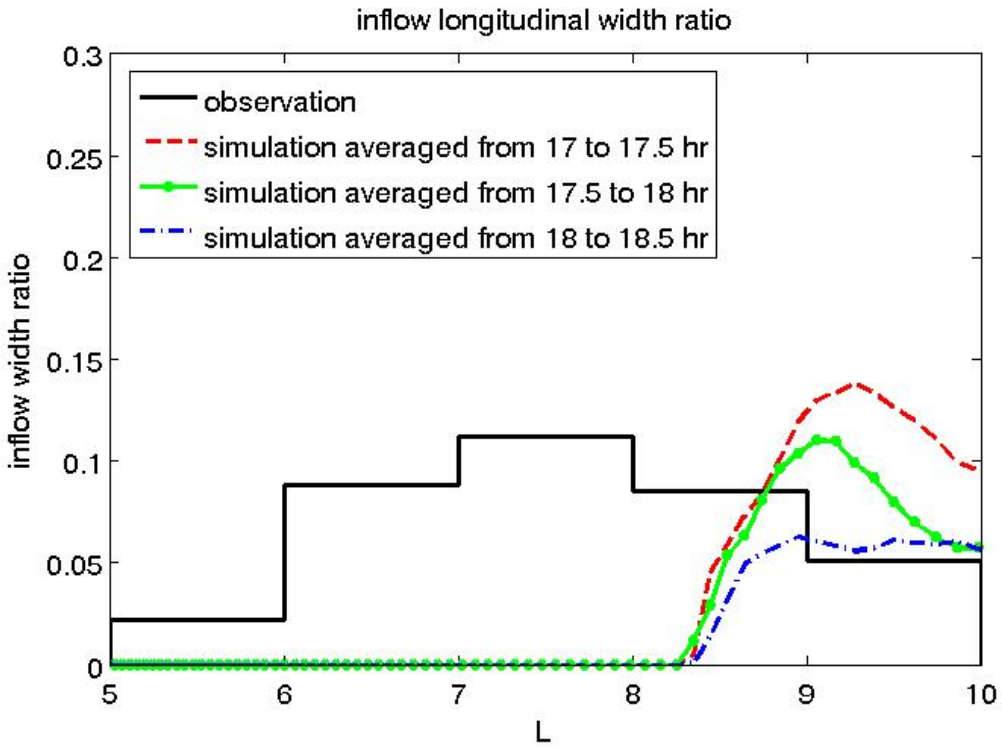

Figure 4.19 Fraction of the available longitude space occupied by inflow channels. (Simulation with CJ10 source model and $\Sigma_P = 2.0$ S)

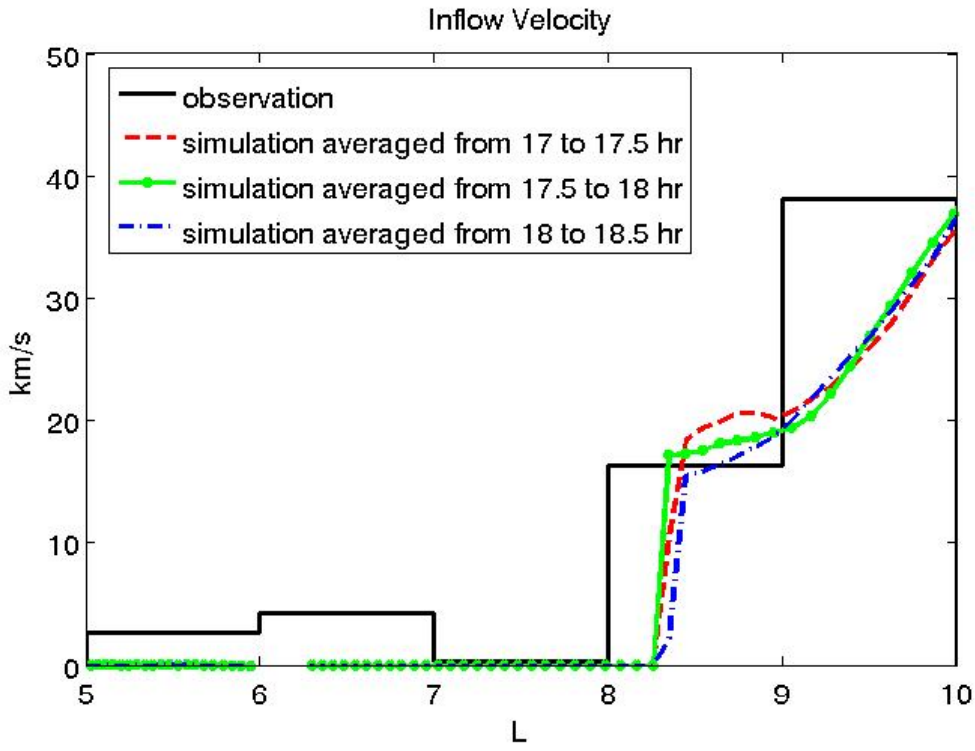

Figure 4.20 Longitudinally averaged inflow velocities. (Simulation with CJ10 source model and $\Sigma_P = 2.0$ S)

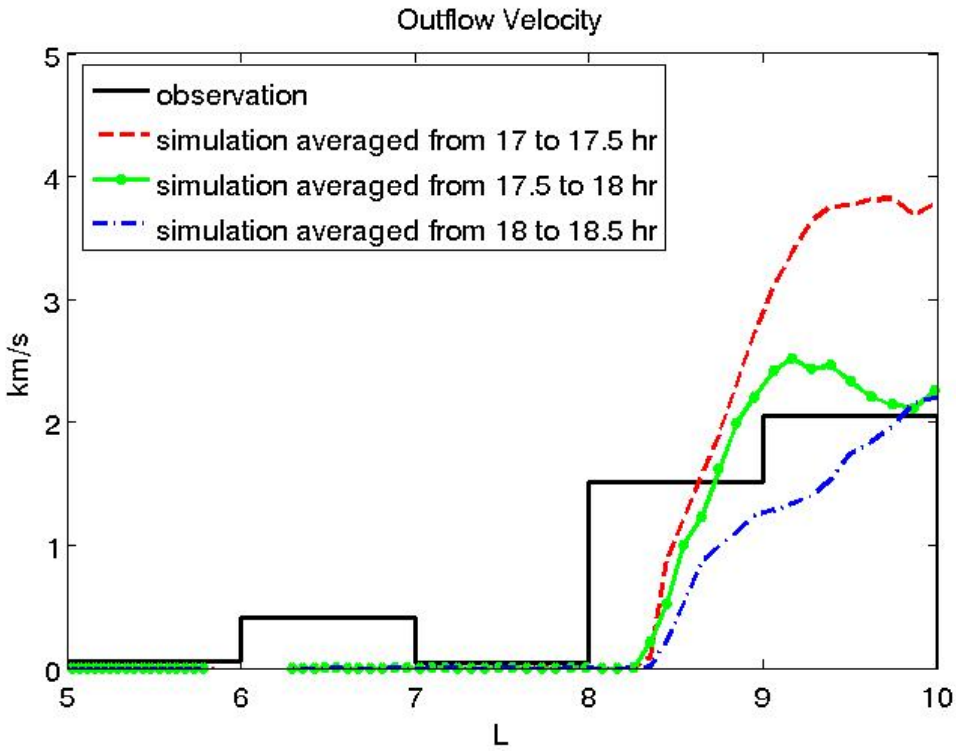

Figure 4.21 Longitudinally averaged outflow velocities. (Simulation with CJ10 source model and $\Sigma_P = 2.0$ S)

4.3. Summary

To agree with recent observational data from CAPS [*Chen et al.,* 2010], we scale the original J06 source model [*Johnson et al.,* 2006] upward by a factor 10. The Pedersen conductance is scaled upward by the same factor 10 to keep the simulated radial flow velocities within the observational bounds. The simulation results with the 10X J06 model are similar to those with the original J06 model, except for some details.

We also try two more recent plasma source models: S10E3 [*Smith et al.,* 2010] and CJ10 [*Cassidy and Johnson,* 2010]. They are similar to each other, but have obvious

discrepancies with the 10X J06 model. In the S10E3 and CJ10 models, the crossover points of the ionization rate and charge exchange rate are further out. The second peaks of the ionization rate are also further out and much larger. These simulation results show that the radial distribution of the plasma source plays a key role in the convection pattern. However, simulations with the S10E3 and CJ10 models do not match the observational results as well as those with the 10X J06 model. In the remainder of this thesis, all simulations use the 10X J06 source model.

Chapter 5

Effect of finite plasma pressure

5.1. Introduction

In Chapter 4, we scaled both the interior plasma source model and the ionospheric Pedersen conductance by a factor 10. However, the interior plasma temperature was set to 0, thus the associated effect of plasma pressure was not included. *Wilson et al.* [2008] used CAPS data to investigate positive ion velocity moments at near-equatorial latitudes, including ion velocities, temperatures and temperature anisotropies. They reported that the temperature of magnetospheric ions increases with radial distance from Saturn, and exhibits temperature anisotropies with $T_{\perp}/T_{\parallel}$ ratios ~3-8 in Saturn's inner magnetosphere. *Wilson et al.* [2009] extended the ion azimuthal velocity profile inward to 3 Rs.

The study described in this chapter extends the simulation study of plasma convection in Saturn's inner magnetosphere by including the effects of finite plasma pressure and the associated gradient-curvature drift by giving the cold plasma a finite

temperature. We also investigate the effects of variations of the ionospheric Pedersen conductance.

5.2. Representation of plasma pressure

In Saturn's inner magnetosphere, the W^+ (water group ion) temperature is anisotropic with $T_\perp / T_\square$ ratios ~3-8 [*Wilson et al.*, 2008]. Therefore, we consider the perpendicular temperature only. The finite perpendicular temperature produces an average force in the positive radial direction (near the equatorial plane) given by

$$\mathbf{F}_{\nabla B} = -\langle \mu \rangle \nabla B = \frac{3kT_\perp}{r_e}\hat{\mathbf{r}} \tag{5.1}$$

where $\langle \mu \rangle = kT_\perp / B$ is the average ion magnetic moment, k is Boltzmann's constant, $T_\perp$ is the W^+ perpendicular temperature, r_e is the radial distance from Saturn's center in the equatorial plane, and the aligned dipole approximation $|\nabla B|/B = 3/r_e$ is adopted (as in previous RCM-S simulations) for Saturn's magnetic field near the equatorial plane.

Figure 5.1 shows sample radial profiles of the W^+ perpendicular temperature. The dash-dotted red line is the W^+ temperature appropriate to pickup at the local rigid corotation speed. The dotted blue line is the W^+ temperature appropriate to local pickup at the observed sub-corotation speed [*Wilson et al.*, 2009]. The solid black line is the observed W^+ perpendicular temperature where available [*Wilson et al.*, 2008]. The

observed temperature (solid black line) is available in the region 5.5-10 Rs, and is smaller than the temperature appropriate to local pickup at the observed sub-corotation speed (dotted line), indicating that some of the observed W^+ ions were picked up, not locally, but closer to Saturn. We assume local pickup temperatures in the closer region 3-5.5 Rs for lack of observed temperature data there. The dashed green line is the W^+ temperature used in the simulation, which takes the value of temperature appropriate to local pickup at the observed sub-corotation speed (dotted blue line) in the region 3-5.5 Rs, and the observed temperature (solid black line) in the region 5.5-10 Rs. This profile is extrapolated smoothly inward and outward, respectively, to the regions $2 < L < 3$ and $10 < L < 12$ that are included in the simulations but not in the observations.

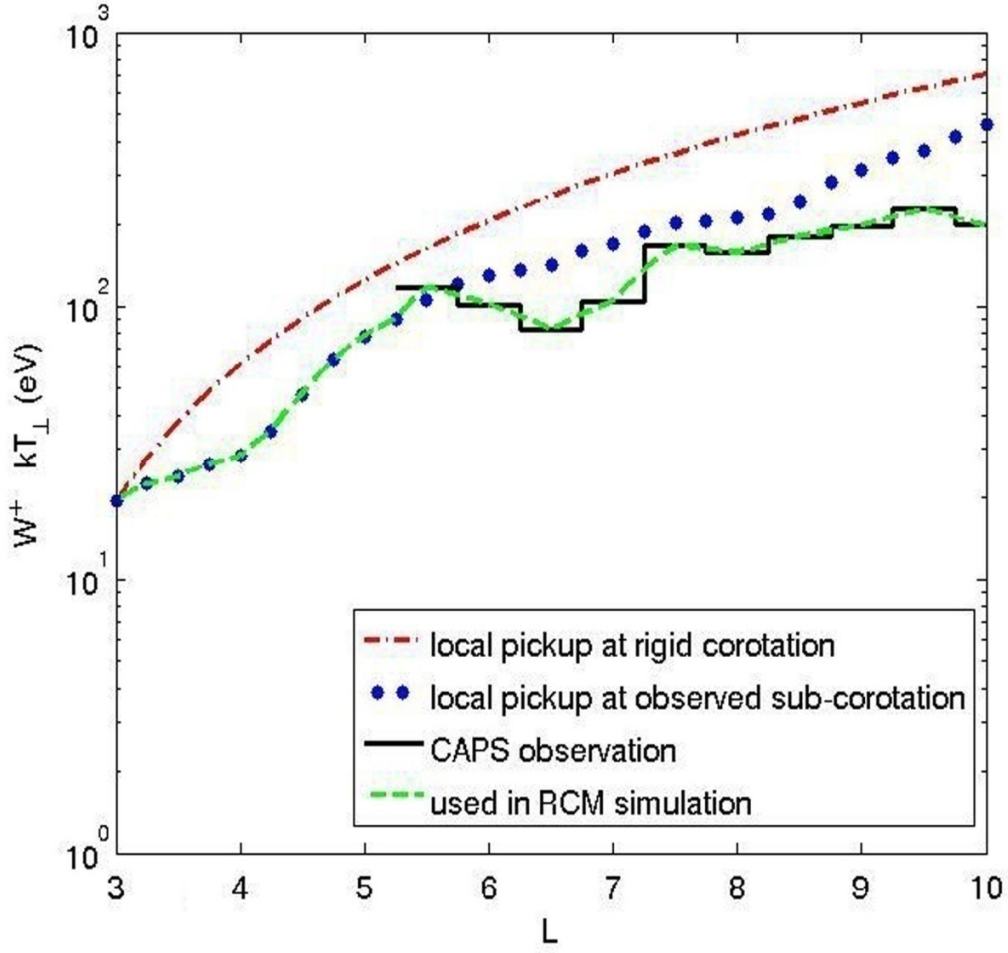

Figure 5.1 Water group ion (W+) perpendicular temperatures. The dash-dotted red line is appropriate to local pick-up at the rigid corotation speed, and the dotted blue line to local pickup at the observed sub-corotation speed [Wilson et al., 2009]. The solid black line is the observed perpendicular temperature [*Wilson et al*., 2008]. The dashed green line, used in the simulations, follows the dotted line in the range L = 3-5.5, and the solid line in the range L = 5.5-10.

Note that this radial profile is quite different from that expected for inward compression of plasma from an exterior source (as assumed, for example, in terrestrial applications of the RCM) because most of the ions' thermal energy here derives from rotational pick-up at, or inward of, the point of observation. It would be impractical to

attempt to model this heating process explicitly within the RCM simulation because it affects, and is affected by, the radial transport process that we are attempting to simulate. Instead we take the ion temperature as an empirical input in order to assess its effect on transport. The electron temperature is neglected because it is known to be much smaller than the ion temperature [*cf. Schippers et al.*, 2008; *Thomsen et al.*, 2010].

For comparison, the centrifugal force near the equatorial plane is

$$\mathbf{F}_C = m\Omega^2 r_e \hat{\mathbf{r}} \tag{5.2}$$

where m is the average mass of W^+ ions (taken to be 17 amu for the observed mixture of O^+, OH^+, H_2O^+, and H_3O^+), and Ω is the observed angular velocity of partial corotation. With the observed temperature data in Figure 5.1, we can easily calculate the ratio $F_{\nabla B}/F_C$, which varies about an average value ~ 0.5 in the region of interest (Figure 5.2). The $-\mu\nabla B$ force is in the same direction as the centrifugal force near the equatorial plane, and of a comparable magnitude. It therefore provides an additional driver of the magnetospheric convection system.

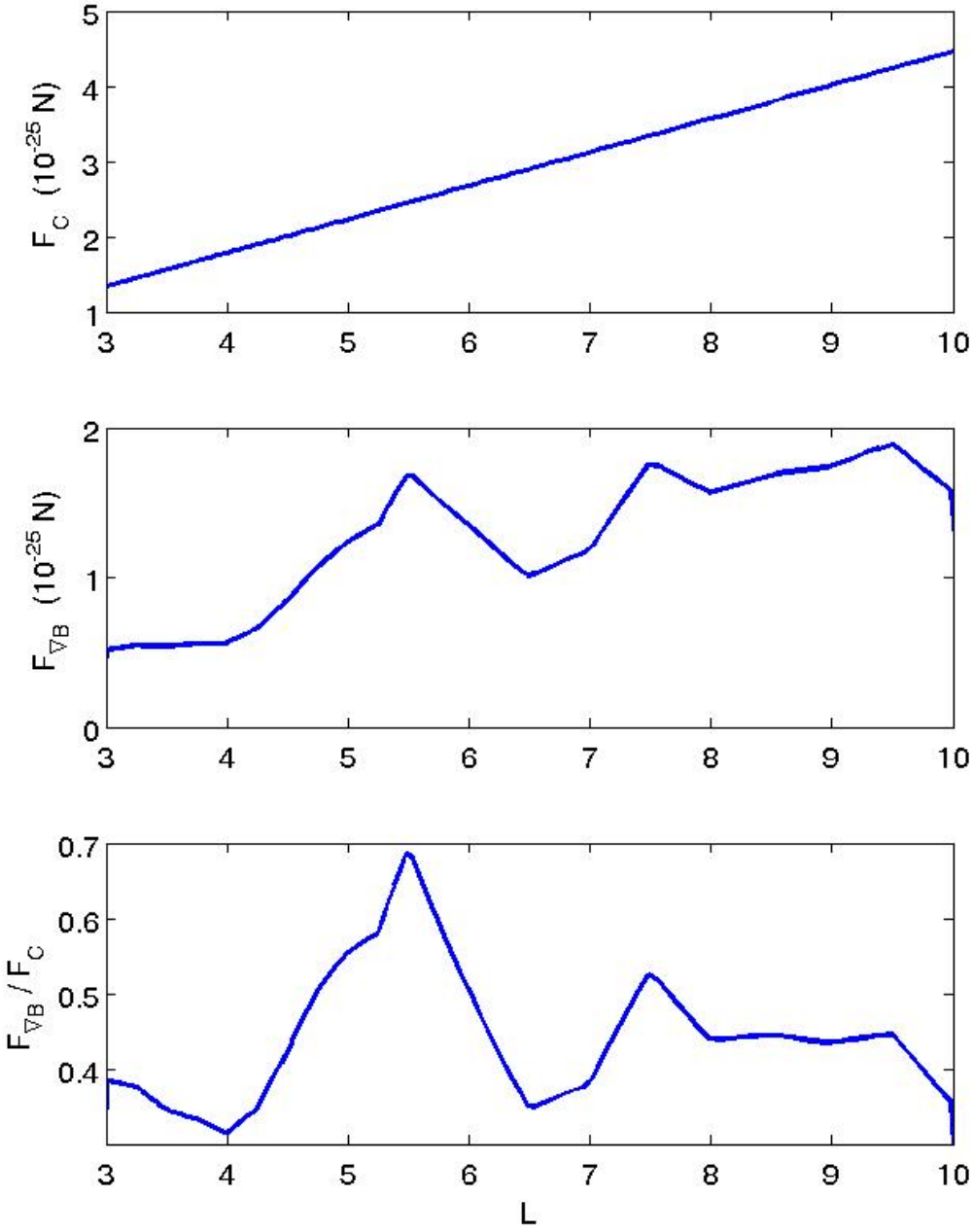

Figure 5.2 Radial profiles of centrifugal force, gradient force, and the ratio of these two forces in the region 3 < L <10.

As in previous RCM simulations for Jupiter [*e.g.*, *Wu et al.*, 2007] and for Saturn [*e.g.*, *Liu et al.*, 2010], we represent the magnetospheric plasma sheet as an equatorially-confined sheet. Also, as in all previous RCM simulations (including terrestrial ones), we represent the pressure-gradient force in terms of its associated guiding-center drift currents. In general, the pressure-gradient current is the sum of all guiding-center drift currents and the magnetization current, but the latter is identically divergence-free (being defined as the curl of the magnetization vector), so it does not contribute to the ionosphere-magnetosphere coupling currents that the RCM attempts to simulate.

Finally, to include the effects of finite plasma pressure, we update (2.13) by adding an extra term in (5.3a)

$$\mathbf{J}_{\perp e} = \frac{\mathbf{B}_e}{B_e} \times \left[-\eta \Omega^2 \mathbf{r}_e + \dot{\eta}_s \left(\boldsymbol{\Omega} \times \mathbf{r}_e - \mathbf{v}_n \right) - \frac{3\eta k T_\perp}{m r_e} \hat{\mathbf{r}} \right] \tag{5.3a}$$

$$\nabla_i \cdot \left[\overleftrightarrow{\Sigma}^* \cdot \left(\nabla_i \Phi \right) \right] = \frac{B_{ir}}{B_e} \nabla_e \cdot \mathbf{J}_{\perp e} \tag{5.3b}$$

$$\mathbf{E} + \mathbf{v} \times \mathbf{B} = 0 \tag{5.3c}$$

with

$$\overleftrightarrow{\Sigma}^* = \begin{pmatrix} (\Sigma_P + \Sigma^*_{\theta\theta}) / \sin I & -(\Sigma_H + \Sigma^*_H) \\ \Sigma_H + \Sigma^*_H & (\Sigma_P + \Sigma^*_{\varphi\varphi}) \sin I \end{pmatrix} \tag{5.3d}$$

$$\Sigma_H^* = -\frac{2\Omega\eta}{B_e} \tag{5.3e}$$

$$\Sigma_{\theta\theta}^* = \frac{\dot{\eta}_s}{B_e}\frac{\sin I}{2\cos\theta} \tag{5.3f}$$

$$\Sigma_{\varphi\varphi}^* = \frac{\dot{\eta}_s}{B_e}\frac{2\cos\theta}{\sin I} \tag{5.3g}$$

5.3. Model setup and simulation results

To illustrate the effects of finite plasma pressure, we compare three sets of RCM-S simulation results:

(A) No plasma pressure ($T_\perp = 0$; Σ_p = 3.0 S).

(B) Finite plasma pressure ($T_\perp$ given by dashed line in Figure 1, Σ_p = 3.0 S).

(C) Finite plasma pressure, Σ_p = 6.0 S.

In simulations A and B, the value Σ_P = 3.0 S is 10 times that assumed by *Liu et al.* [2010], as discussed in Chapter 4. In simulation C, Σ_p is increased to 6.0 S to constrain the larger radial velocities caused by the inclusion of plasma pressure, as also discussed above. The value 6.0 S used here is well within the bounds established by the observation-based aeronomical models of Moore et al. [2010]. All 3 simulations use the 10X J06 plasma source model,

The results of simulation A are shown and discussed in Chapter 4.1.2. Here we show the results of simulations B and C.

Figure 5.3 shows the results of simulation B. The appearance of outflow fingers in simulation B is at 19 hr (panel b), which is earlier than the 21.25 hr in simulation A (Figure 4.3, panel b). This confirms that the $-\mu\nabla B$ force provides an additional driving force, accelerating the evolution of the convection system. In further development (panels c and d), the heads of the outflow fingers are broader in simulation B than those in simulation A. The reason may be that the larger radial velocities (shown in Figures 5.7 and 5.8 below) produce larger Coriolis accelerations, and thus larger azimuthal velocities. Finally, simulation B reaches a quasi-steady state at 26.25 hr (panel f), also earlier than the 30.5 hr of simulation A (Figure 4.3, panel f). Figure 5.4 shows the plasma mass flux at 26.25 hr.

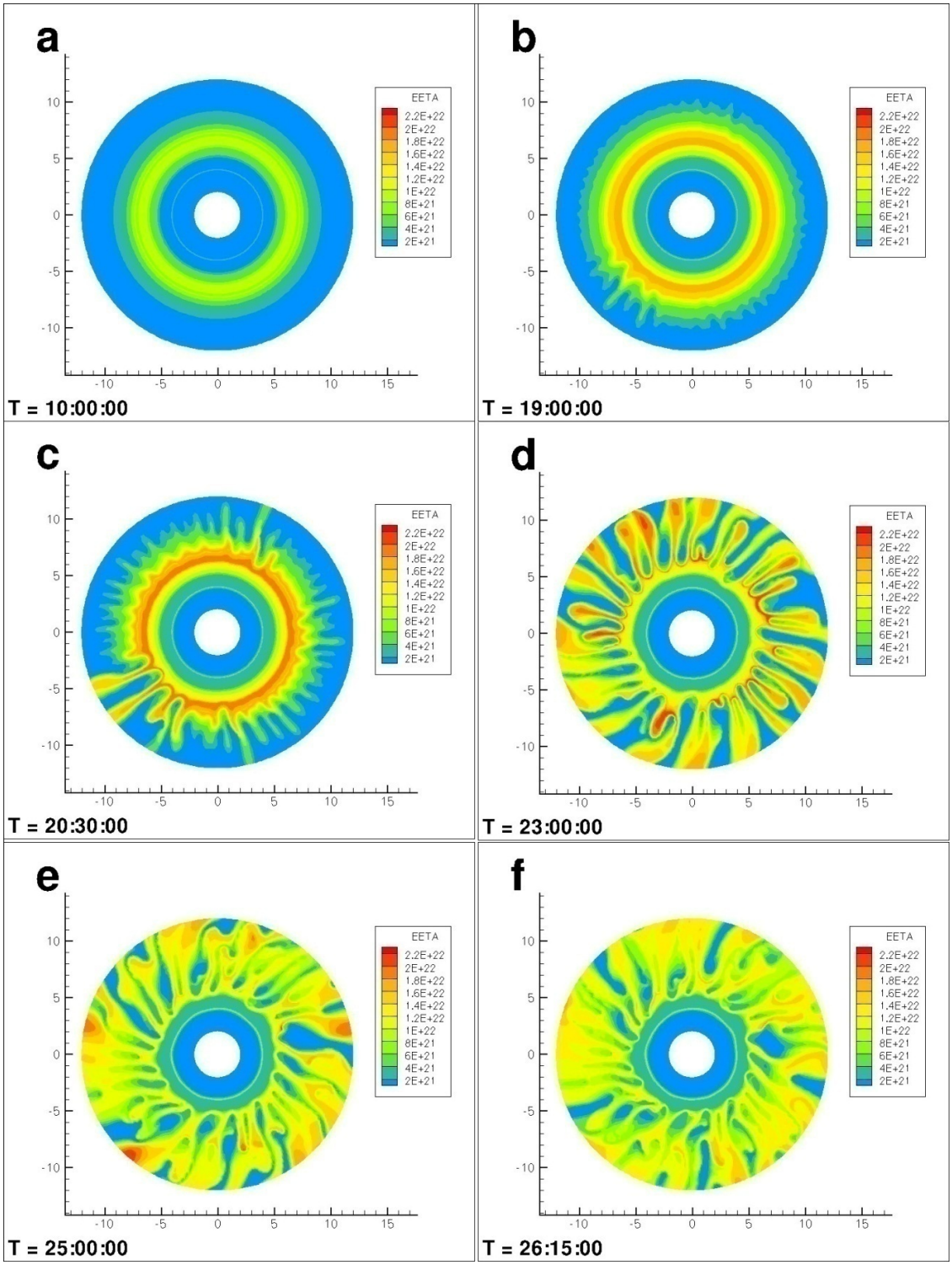

Figure 5.3 Simulation B with finite plasma pressure and Σ_P = 3.0 S.

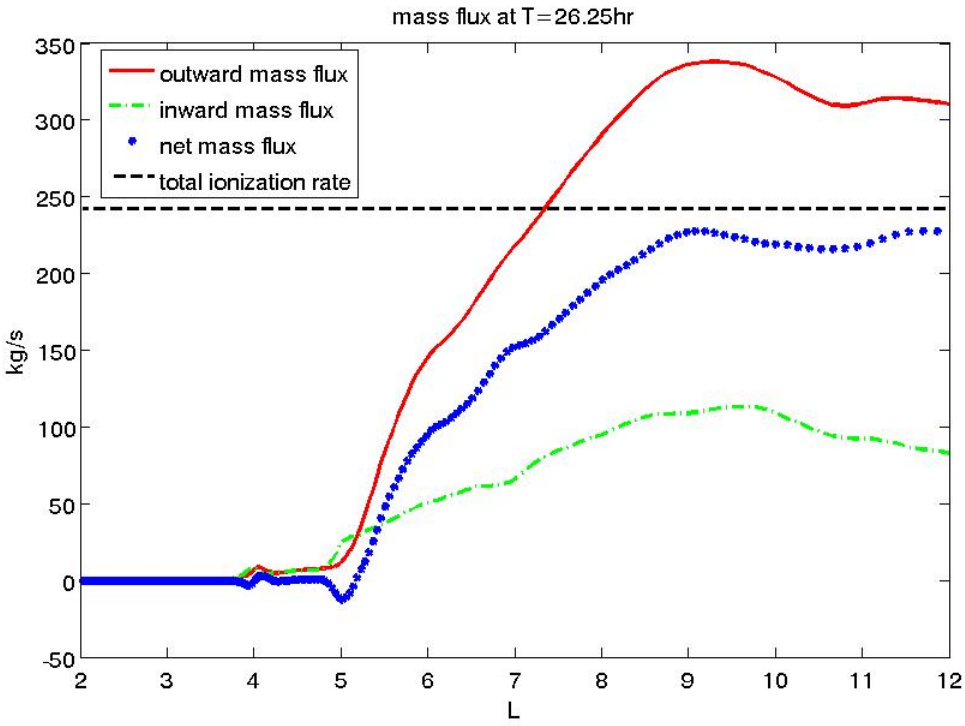

Figure 5.4 Radial plasma mass flux at T = 26.25 hr in simulation B.

Figure 5.5 shows the results of simulation C. The outflow fingers take the longest time, 29 hr (panel b), to appear, confirming that the interchange instability is suppressed by higher Pedersen conductance. The large red region shows that higher Pedersen conductance confines much more plasma (shown in Figure 5.11 below). In panels c and d, the heads of the outflow fingers are of the same size as those in simulation A, smaller than those in simulation B. This confirms that the radial velocities are reduced by the higher Pedersen conductance. Simulation C takes as long as 37.5 hr to reach a quasi-steady state. Figure 5.6 shows the plasma mass flux at 37.5 hr.

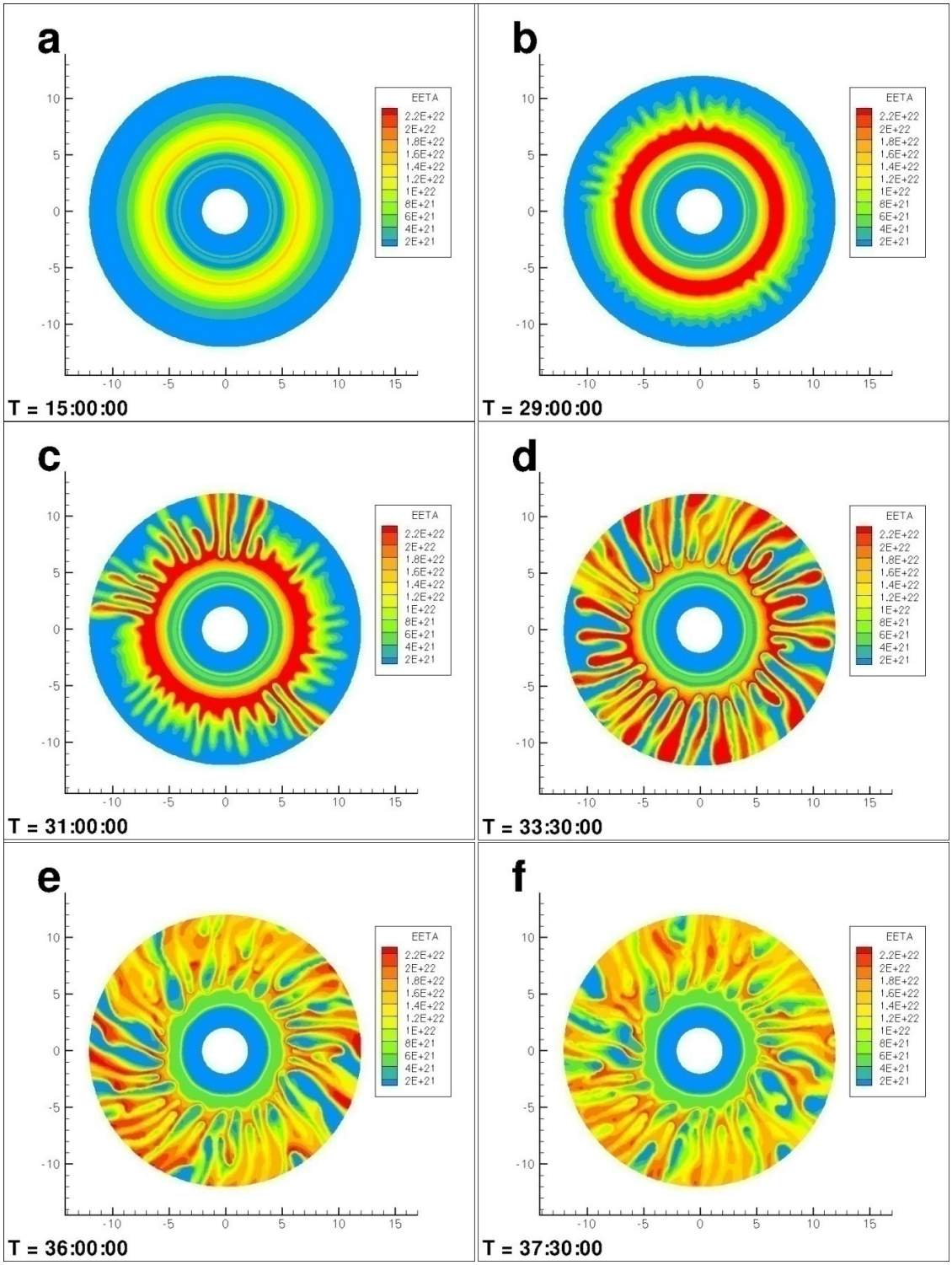

Figure 5.5 Simulation C with finite plasma pressure and Σ_P = 6.0 S.

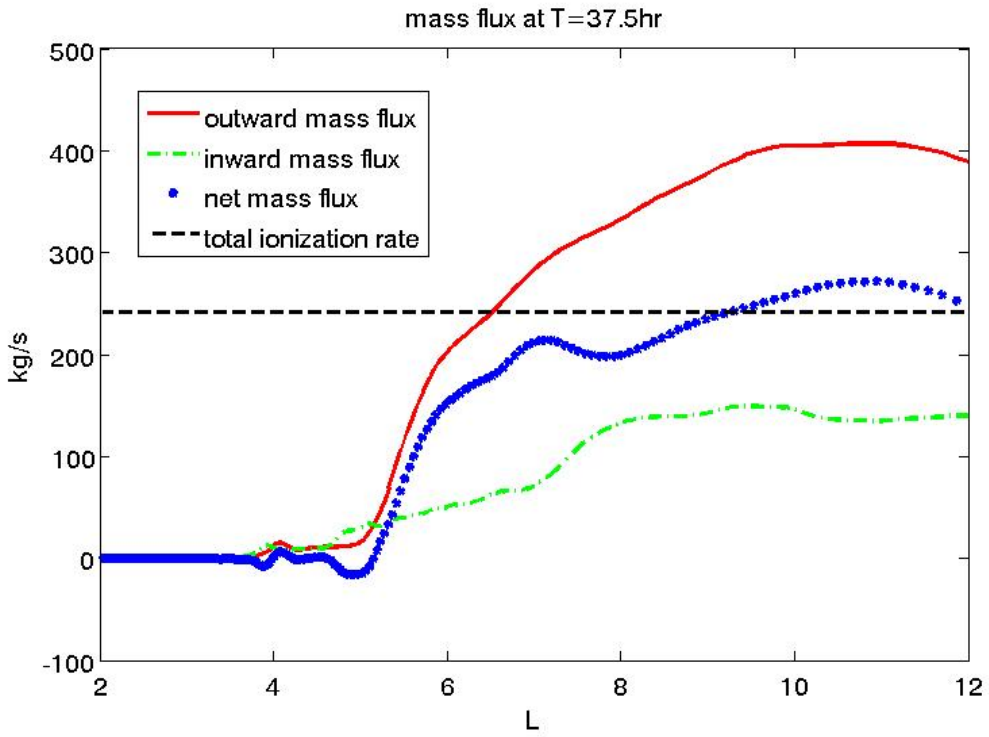

Figure 5.6 Radial plasma mass flux at T = 37.5 hr in simulation C.

5.4. Discussion

To clearly compare the three simulations A, B, and C, we plot their statistical analyses together. In Figures 5.7 - 5.11, the red line, the green line, and the blue line show statistical results of simulations A, B, and C, respectively. Those simulation results are averaged over 1/2 hour intervals during the quasi-steady state of each simulation. The black solid line (histogram) shows the CAPS observations reported by *Chen et al.* [2010].

Figures 5.7 and 5.8 show the longitudinally averaged inflow and outflow velocities. Simulation B has larger radial velocities, both inflow and outflow, than

simulation A. The obvious reason is the finite plasma pressure included in B but not A. The ratio of the radial velocities in simulation B to those in simulation A is about 1.5-1.8. This is consistent with the theoretical expectation based on the fact that the $-\mu\nabla B$ force is about 1/2 of the centrifugal force. (The convection system is nonlinear. Other factors, such as the Coriolis acceleration and the pickup current, also affect the convection pattern.) In simulation C, we impose a larger Pedersen conductance, and successfully reduce the radial velocities to within observational constraints.

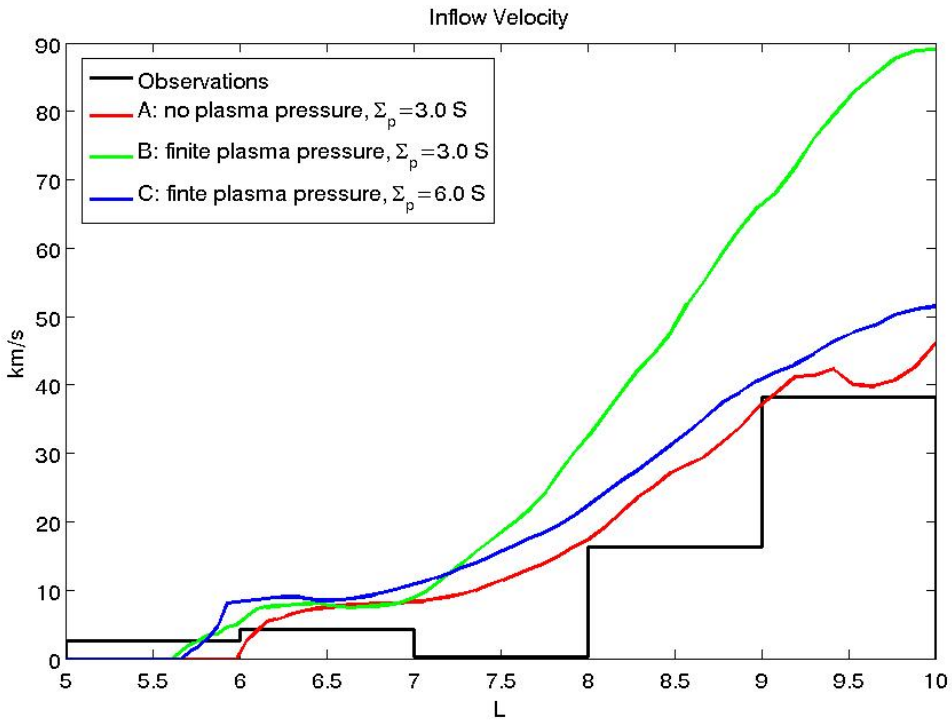

Figure 5.7 Longitudinally averaged inflow velocities of simulations A, B, and C. Simulation results averaged over 1/2 hr intervals during the quasi-steady state of each simulation.

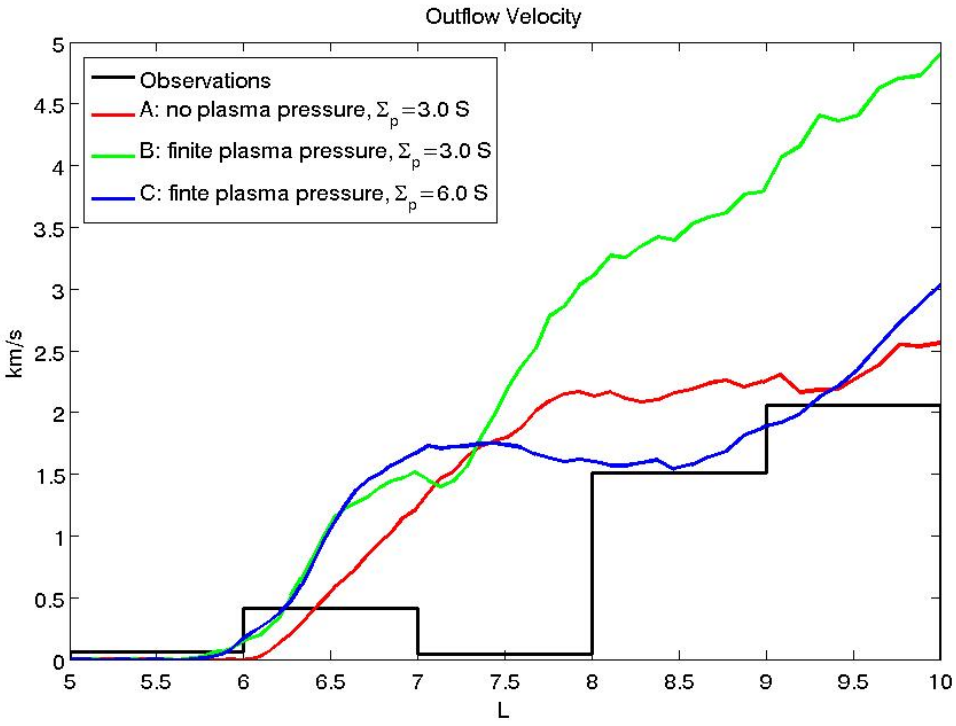

Figure 5.8 Longitudinally averaged outflow velocities of simulations A, B, and C.

Figure 5.9 shows the radial profile of the inflow longitudinal width ratio. Results of all three simulations are consistent with observations. The reason is that all three simulations use the same plasma source model: the 10X J06 model. Different plasma source models cause different convection patterns, and therefore large discrepancies in the inflow longitudinal width ratio, as discussed in Chapter 4.2.

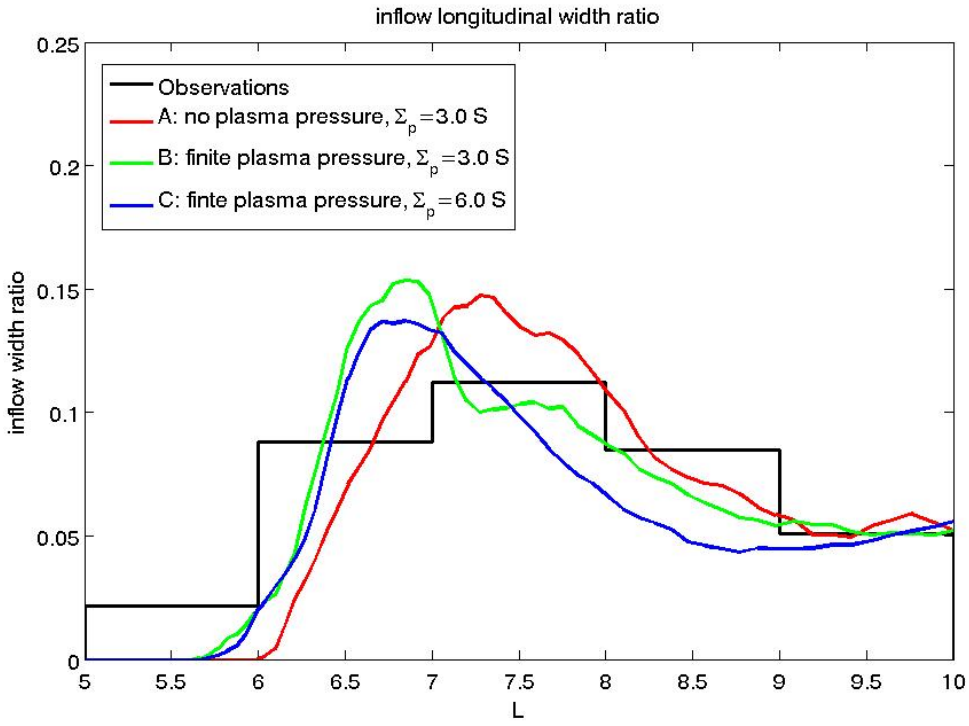

Figure 5.9 Inflow longitudinal width ratio of simulations A, B and C.

Figure 5.10 shows the outflow mass transport rate. At 10 Rs, close to the outer boundary of our simulations, the outflow mass transport rates of the simulations are in the range 190 – 260 kg/s. These values are roughly consistent with the imposed total mass loading rate of 240 kg/s. This confirms our identification of quasi-steady states, during which the total interior plasma source rate is roughly balanced by the outflow flux. The mass outflow rate inferred from observations is slightly larger, ~280 kg/s [*Chen et al.*, 2010].

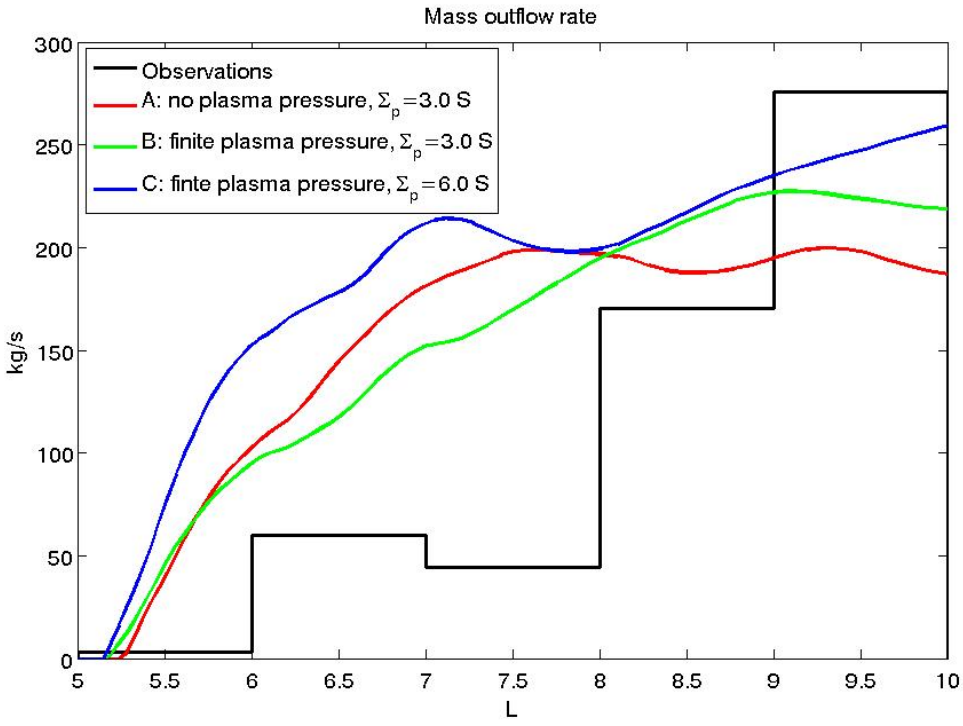

Figure 5.10 Outflow mass transport rate of simulations A, B, and C.

Figure 5.11 shows the flux tube plasma mass content η, averaged over longitude. The values of η in simulation C are larger than in simulations A and B, as also shown in Figure 5.5. The reason is probably that the higher ionospheric Pedersen conductance in simulation C suppresses the interchange instability and confines more plasma in the simulated region. Simulations A and B have the same Pedersen conductance. Because simulation B has the extra driving force (finite plasma pressure) and correspondingly larger outflow velocities, η in simulation B is smaller than in simulation A. However, even in simulation C, η is smaller than indicated by observations [*Chen et al.*, 2010, Figure 5]. This may suggest a higher mass loading rate and a higher ionospheric Pedersen conductance.

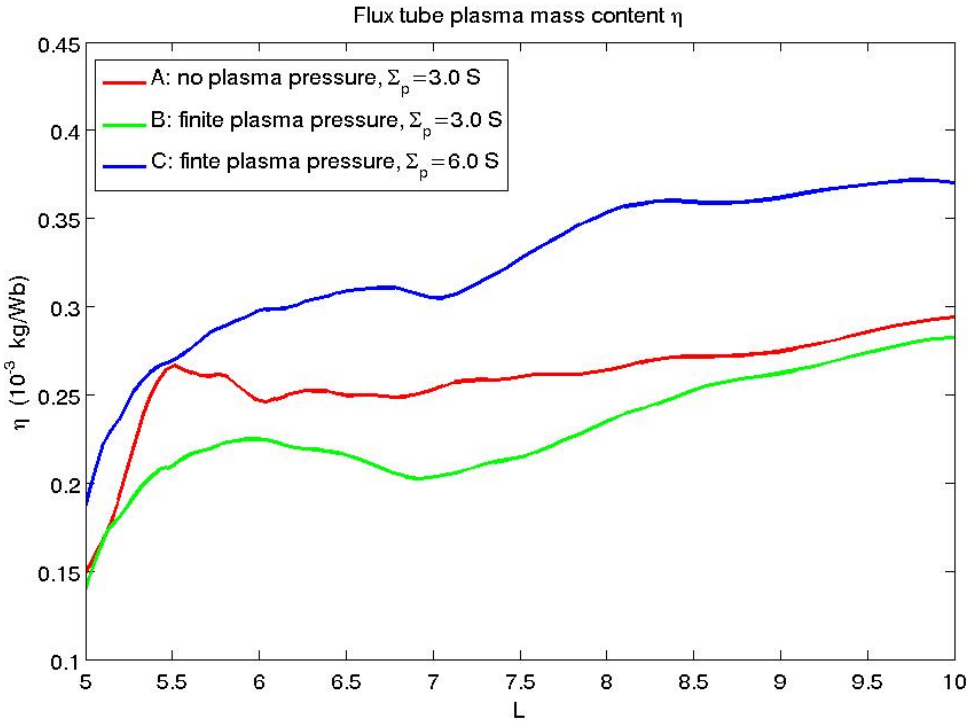

Figure 5.11 Flux tube plasma mass content of simulations A, B, and C.

5.5. Summary

We have generalized our previous RCM-S simulations by incorporating the effects of finite plasma pressure and the associated gradient-drift current. Observations have shown, as expected, that the ion temperature is anisotropic with $T_{\perp} > T_{\parallel}$. Our simulations confirm the theoretical expectation that the finite plasma pressure provides a $-\mu\nabla B$ force in the positive radial direction, which augments the driving force provided by the centrifugal force. The magnitude of the $-\mu\nabla B$ force is about 1/2 the magnitude of the centrifugal force, and thus provides a ~50% enhancement of the centrifugal instability growth rate. Our simulations also confirm that the ionospheric Pedersen conductance

constrains the radial velocities of plasma flow. This is consistent with the results of earlier analytical models [*e.g.*, *Huang and Hill*, 1991] which have, however, been restricted so far to simpler initial-value problems with no continuously active plasma source.

Chapter 6

Hot plasma and V-shape injection signature

6.1. Introduction

One feature of the rotation-driven convection in Saturn's magnetosphere is that wider, slower outflow channels of cooler, denser plasma alternate with narrower, faster inflow channels of hotter, more tenuous plasma. The earliest, and perhaps the most definitive, evidence is the ubiquitous injection-dispersion events that are observed on every pass of the Cassini spacecraft through the inner magnetosphere, $5 <\sim L <\sim 10$ [*André et al*., 2005; *Burch et al*., 2005; *Hill et al.,* 2005; *Mauk et al*., 2005, *Chen and Hill* 2008].

Figure 6.1 shows a cartoon of the injection event of hot and tenuous plasma and the dispersion signature. The hot plasma moves inward as a result of $\mathbf{E}\times\mathbf{B}$ drift. The additional adiabatic gradient and curvature drifts, proportional to particle energy and to charge sign, separate positive ions and electrons and form V-shaped signatures, shown in

Figure 6.2. The top and middle panels are electron and positive ion spectrograms, respectively. The ion signature is often invisible in the dispersion signature because ion fluxes are typically much smaller than electron fluxes. When visible, the ion leg of the dispersion signature is always the mirror image of the electron leg. Two legs intersect on the zero-energy axis and form a "V". On the x-axis, the energy-longitude V-shaped signatures are directly transformed into observable energy-time V-shaped signatures, because the V structures are swept past the spacecraft at the local plasma rotational speed, which is much larger than either the spacecraft speed relative to Saturn or the gradient-curvature drift speed [*Hill et al.,* 2005]. In Figure 6.2, the slopes of each V structure are different, which provide direct information of the age of each injection-dispersion event. Generally, event with large slope is in new age, vice versa.

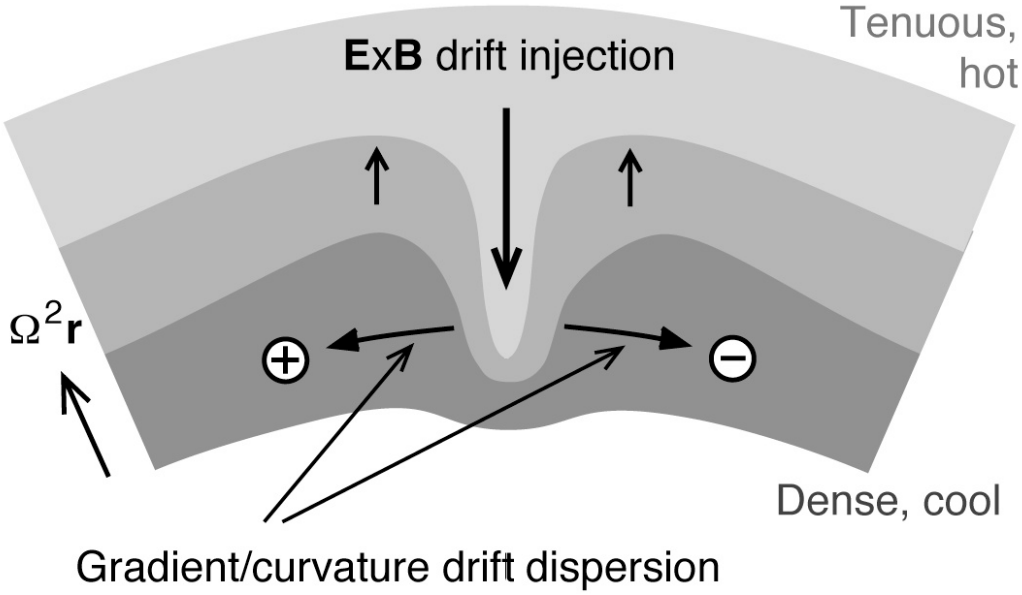

Figure 6.1 Schematic illustration of a localized injection of hot plasma from the outer magnetosphere, accompanied by adiabatic gradient and curvature drift, producing a V-

shaped dispersion signature on a linear energy-longitude spectrogram. Figure from *Hill et al.* [2005].

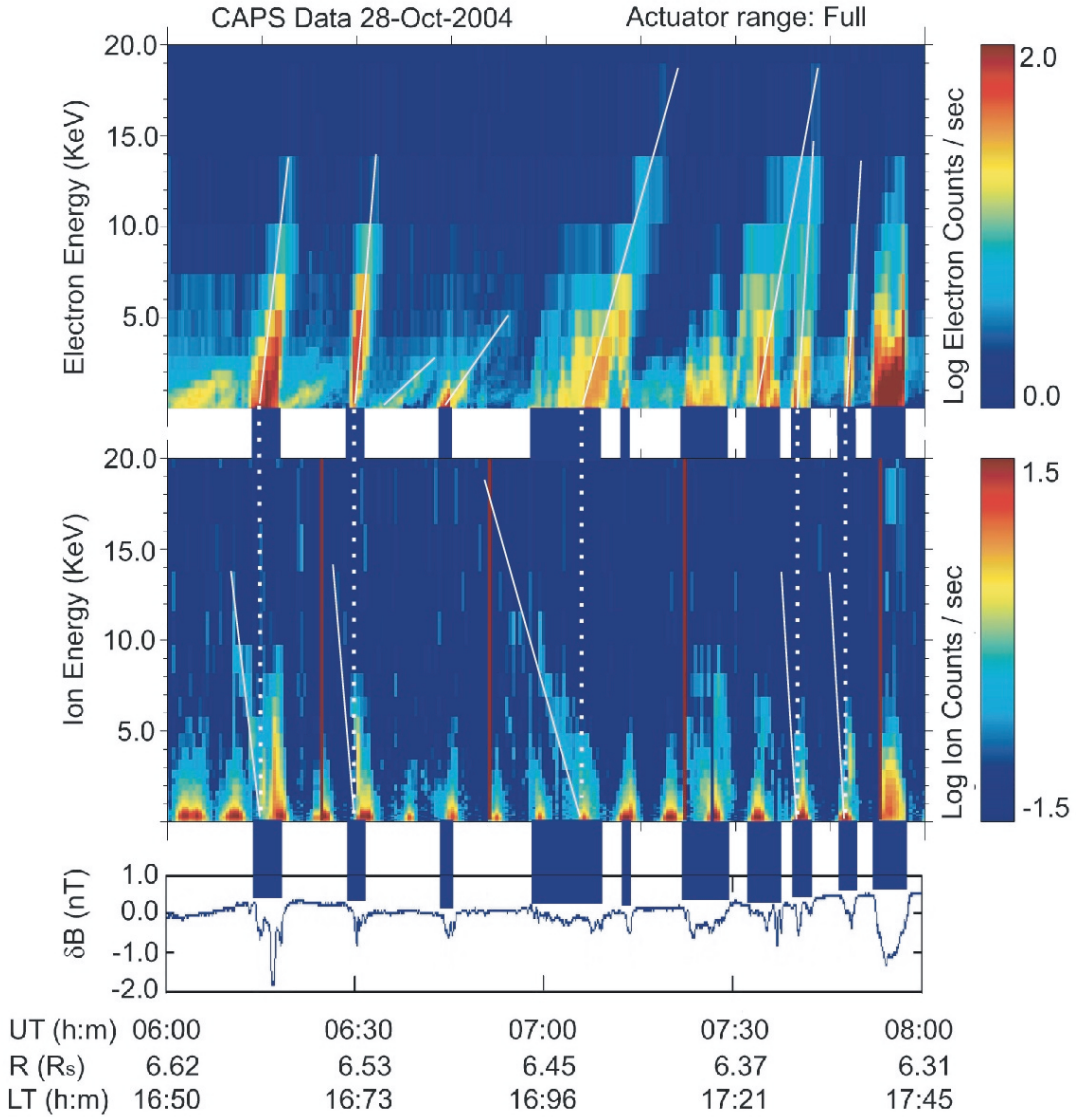

Figure 6.2 Linear energy-time spectrograms for electrons (top) and positive ions (middle) from the CAPS instruments on 28 October 2004 during the second Cassini orbit of Saturn. Figure from Hill et al. [2005].

Until now, our simulations have only included the cool plasma from the interior source. Inflow channels are empty in previous simulations. We can only calculate values such as the average inflow velocities and the fraction of the available longitude space occupied by inflow channels. In this chapter, we add hot plasma at the outer boundary and investigate the fine scale V structures of the injected energetic plasma.

6.2. Simulations with hot plasma

6.2.1. Hot plasma properties

Unlike the cool plasma from the interior source, which is anisotropic and confined in the plasma sheet near the equatorial plane [*Hill and Michel*, 1976], the hot plasma is isotropic and bouncing along the magnetic field lines between mirror points. The energy per particle is given by

$$E = \lambda(\int ds / B)^{-2/3} \tag{6.1}$$

where λ is the energy invariant, which is constant along a drift path, and $\int ds / B$ is the flux tube volume per unit magnetic flux. Notice that for cool plasma, $\int ds / B$ is simplified to $2H_s / B_e$, where H_s is the scale height shown in Figure 2.2 and B_e is the magnetic field at the equatorial plane. But for isotropic hot plasma in a dipole magnetic field, the flux tube volume is

$$\int ds / B = \frac{32L^4 R_s}{35B_{e0}} \sqrt{1-\frac{1}{L}}(1+\frac{1}{2L}+\frac{3}{8L^2}+\frac{5}{16L^3}) \tag{6.2}$$

where B_{e0} is the magnetic field at the equatorial plane near Saturn's surface. The gradient and curvature drift velocity of hot isotropic plasma is

$$\mathbf{v}_{GCe} = \frac{\lambda \hat{\mathbf{b}} \times \nabla_e (\int ds / B)^{-2/3}}{qB_e} \tag{6.3}$$

[*Wolf*, 1983]. This velocity is linear in the particle's energy, and therefore forms straight lines in a linear energy-longitude or energy-time spectrogram.

Besides the gradient and curvature drift, hot plasma is also affected by centrifugal force and Coriolis force. The pickup process is not important to the hot particle population, but only to the newly generated plasma from ionization and charge exchange processes. We update (5.3) by including the hot plasma and get (6.4)

$$\mathbf{J}_{\perp e} = \frac{\mathbf{B}_e}{B_e} \times \left[-\sum_i \eta_i \Omega^2 \mathbf{r}_e + \dot{\eta}_s \left(\mathbf{\Omega} \times \mathbf{r}_e - \mathbf{v}_n \right) - \frac{3\eta_{i=1} k T_\perp}{m r_e} \hat{\mathbf{r}} + \sum_{i>1} \frac{\lambda_i \eta_i}{m} \nabla_e \left(\int ds / B \right)^{-2/3} \right] \tag{6.4a}$$

$$\nabla_i \cdot \left[\vec{\Sigma}^* \cdot \left(\nabla_i \Phi \right) \right] = \frac{B_{ir}}{B_e} \nabla_e \cdot \mathbf{J}_{\perp e} \tag{6.4b}$$

$$\mathbf{E} + \mathbf{v} \times \mathbf{B} = 0 \tag{6.4c}$$

with

$$\vec{\Sigma}^* = \begin{pmatrix} (\Sigma_P + \Sigma^*_{\theta\theta}) / \sin I & -(\Sigma_H + \Sigma^*_H) \\ \Sigma_H + \Sigma^*_H & (\Sigma_P + \Sigma^*_{\varphi\varphi}) \sin I \end{pmatrix} \tag{6.4d}$$

$$\Sigma^*_H = -\sum_i \frac{2\Omega \eta_i}{B_e} \tag{6.4e}$$

$$\Sigma^*_{\theta\theta} = \frac{\dot{\eta}_s}{B_e} \frac{\sin I}{2\cos\theta} \tag{6.4f}$$

$$\Sigma^*_{\varphi\varphi} = \frac{\dot{\eta}_s}{B_e} \frac{2\cos\theta}{\sin I} \tag{6.4g}$$

where i is the energy channel index. In order to investigate the energy spectrogram, we need multiple channels to represent particles with different energies. Channel i = 1 is assigned to the cool plasma from the interior source, and channels i > 1 are assigned to hot plasma injected from the outer boundary.

6.2.2. Model setup

We assume the hot plasma velocity has a Maxwellian distribution

$$dn = f(v)d^3v = n_0(\frac{m}{2\pi kT})^{3/2}\exp(-\frac{mv^2}{2kT})d^3v \tag{6.5}$$

The corresponding energy distribution is

$$dn = f(E)dE = 2n_0(\frac{E}{\pi E_0^{\ 3}})^{1/2}\exp(-\frac{E}{E_0})dE \tag{6.6}$$

where n is particle density and E is particle energy. According to the CAPS observations, n_0 = 0.3 cm^{-3} and E_0 = 110 eV for W^+ at L = 12 [*Thomsen et al.*, 2010]. For electrons, *Schippers et al.* [2008] used two Maxwellian distributions to represent the energy distribution at L = 12.8. One is n_0 = 0.29 cm^{-3} and E_0 = 11 eV, and the other is n_0 = 0.08 cm^{-3} and E_0 = 819 eV. (*Schippers et al.* [2008] also used two kappa distributions which can represent the electron energy distribution better than two Maxwellian distributions. Because the study here focuses on the energy and gradient-curvature drift, the Maxwellian distribution is good enough. We may incorporate the kappa distribution in future work.) In the RCM-S the outer boundary is set at L = 40 to suppress the effects of the outer potential boundary condition within our region of interest ($2 < L < 12$). We need

to move the boundary conditions of the hot plasma adiabatically to $L = 40$ ($n_0 \sim L^{-4}$ and $E_0 \sim L^{-8/3}$), because the flux tube mass content η and the energy invariant λ are both assumed constant along the drift path. We also initially put the hot plasma in the region $12 < L < 40$ to avoid the long delay time for hot plasma to drift from $L = 40$ to L=12.

The rest of the setup is the same as for simulation C in Chapter 5. The cool plasma is derived from the 10X J06 source model. The Pedersen conductance is 6.0 S and the Hall conductance is 0.

6.2.3. Simulation results

Figures 6.3 - 6.8 show six stages of the simulation at the same times as simulation C in Chapter 5. We show five channels: the top panel shows the cool W^+ ions from the interior source, the two middle panels show hot W^+ with different energy invariants, and the two bottom panels show hot e^- with different invariants. Notice that the color bars of each panel are different. The cool plasma from the interior source is always dominant except within the inflow channels where it is excluded. The top panels of Figures 6.3 - 6.8 are similar to Figure 5.5 but differ in detail because of the electrodynamic effects of newly-added hot plasma from exterior sources. The effect of hot plasma is probably overestimated because we initially put hot plasma in the whole region $12 < L < 40$. We may add the hot plasma in a more realistic way in future work.

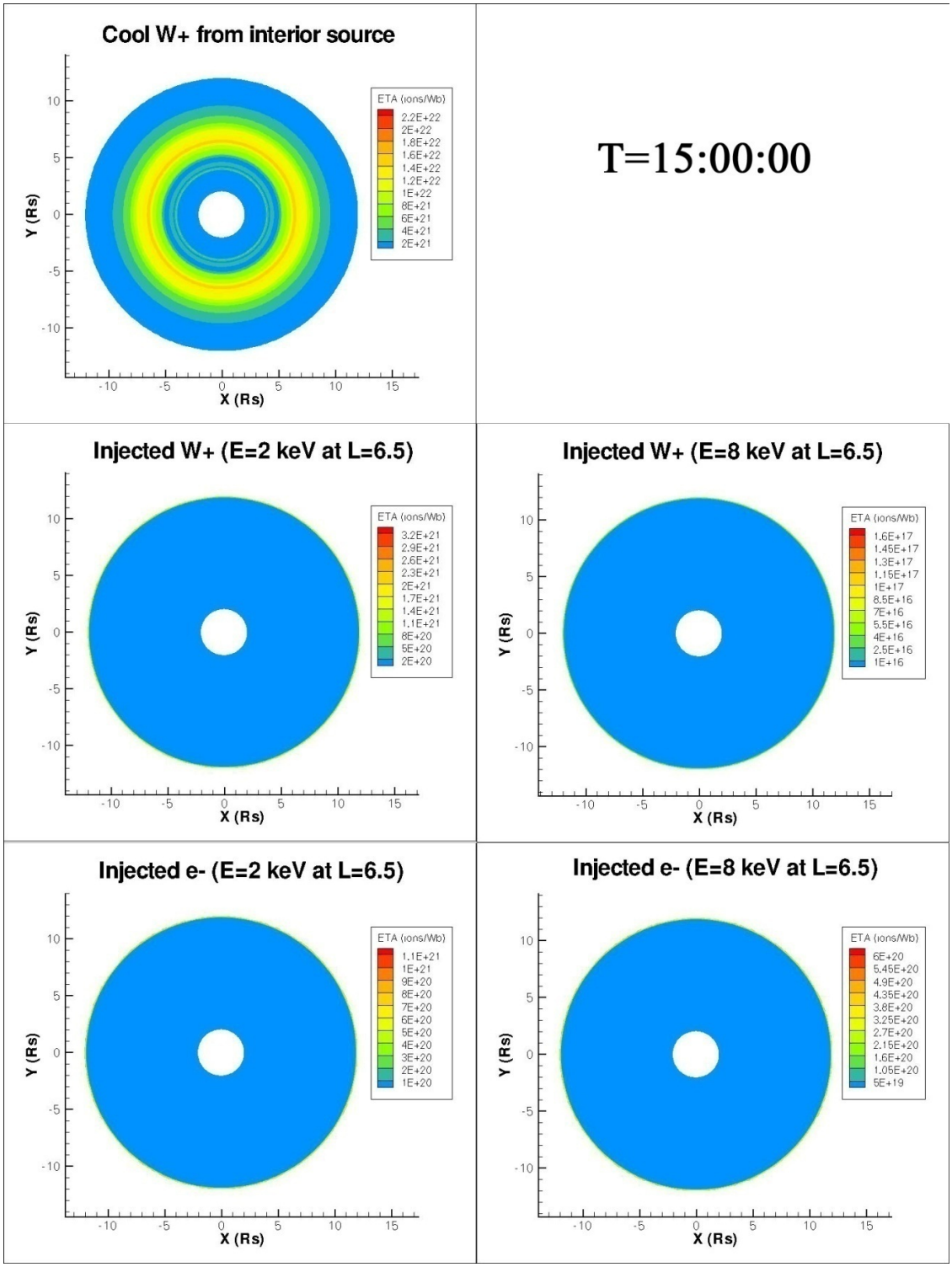

Figure 6.3 Simulation with hot plasma at T = 15:00:00. Top left: cool dense W+ from interior sources. Middle: low (left) and high (right) energy channels of hot W+ from

exterior sources. Bottom: low (left) and high (right) energy channels of hot e- from exterior source.

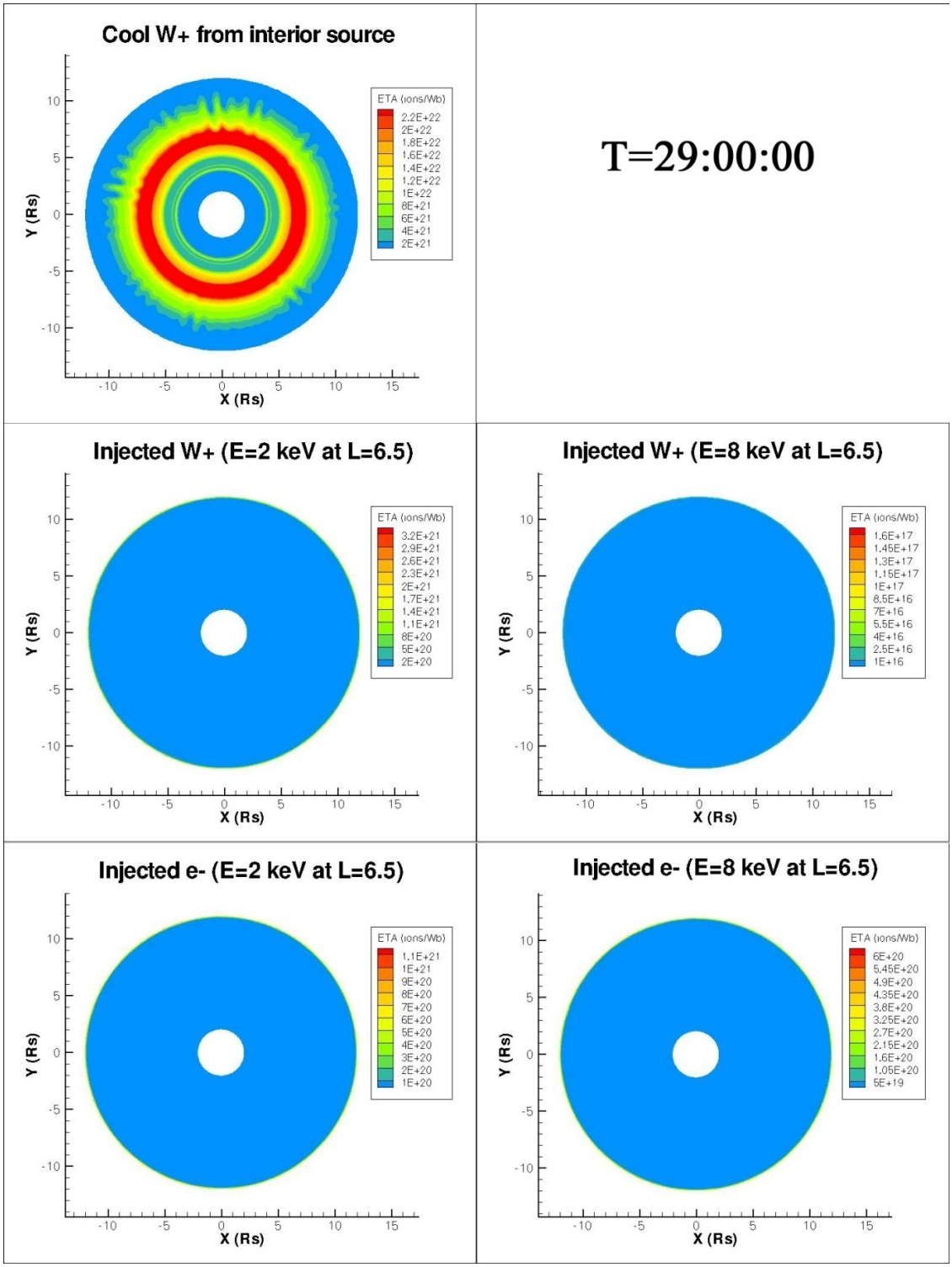

Figure 6.4 Same as Figure 6.3 but at T = 29:00:00.

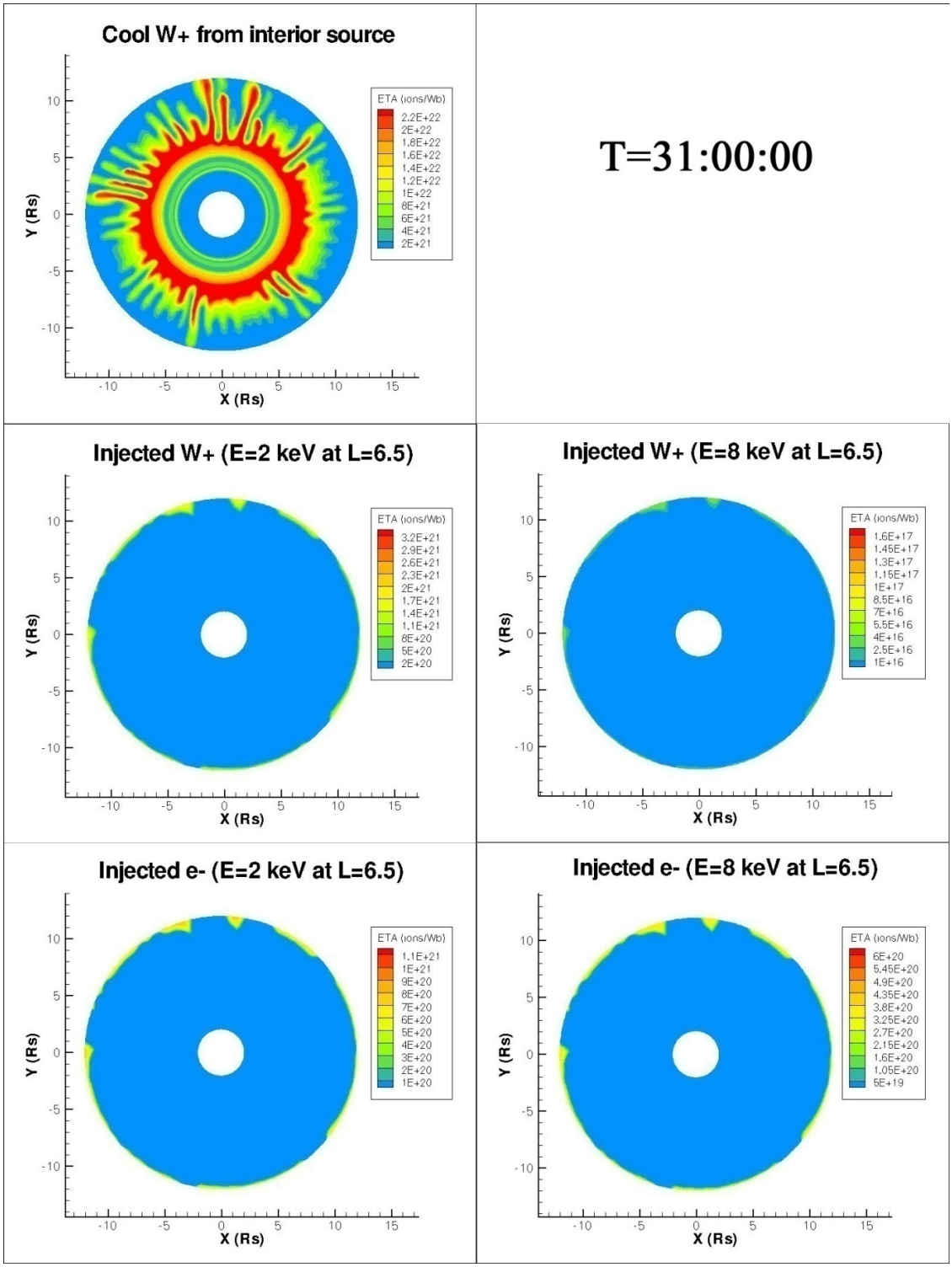

Figure 6.5 Same as Figure 6.3 but at T = 31:00:00.

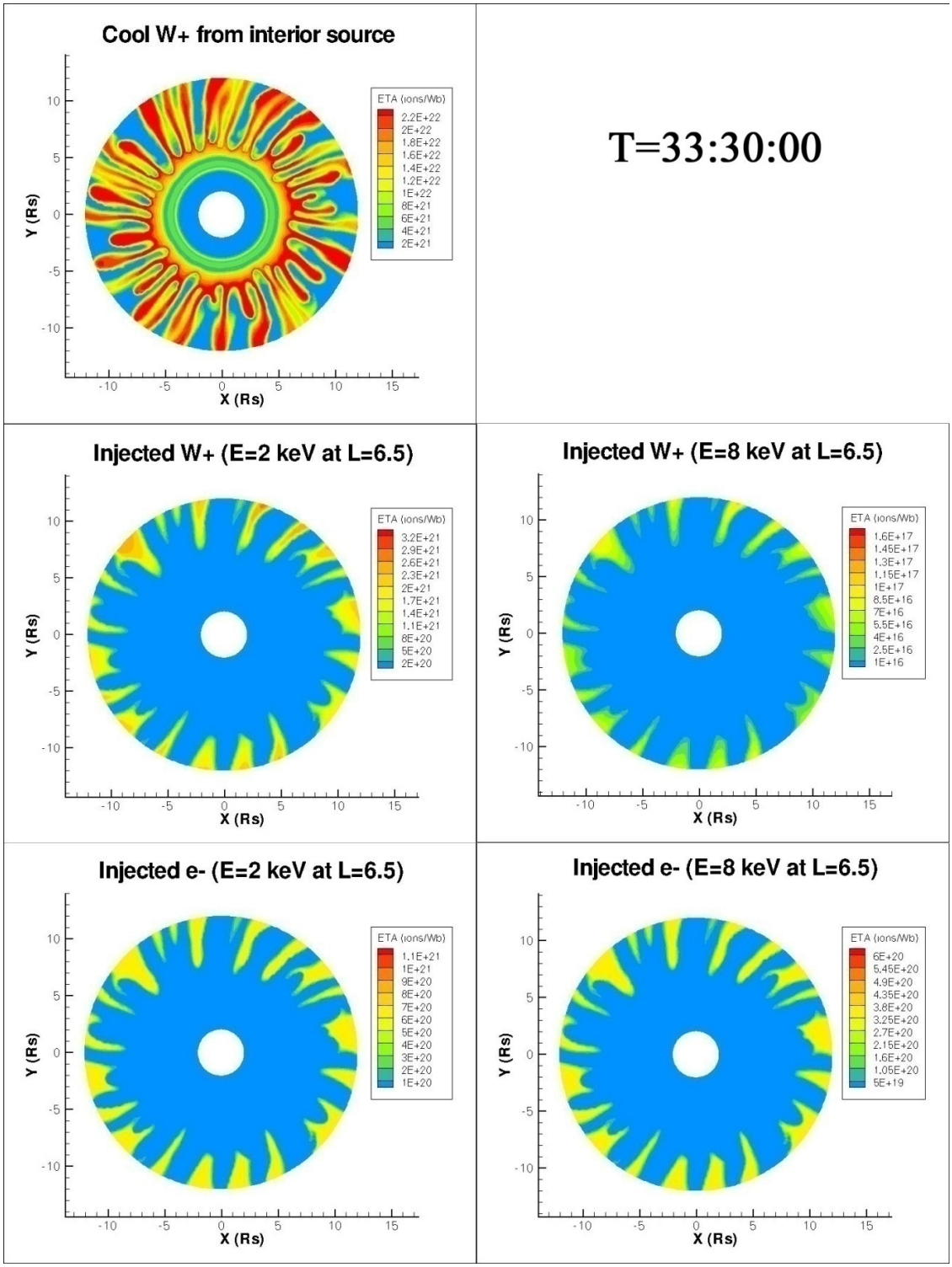

Figure 6.6 Same as Figure 6.3 but at T = 33:30:00.

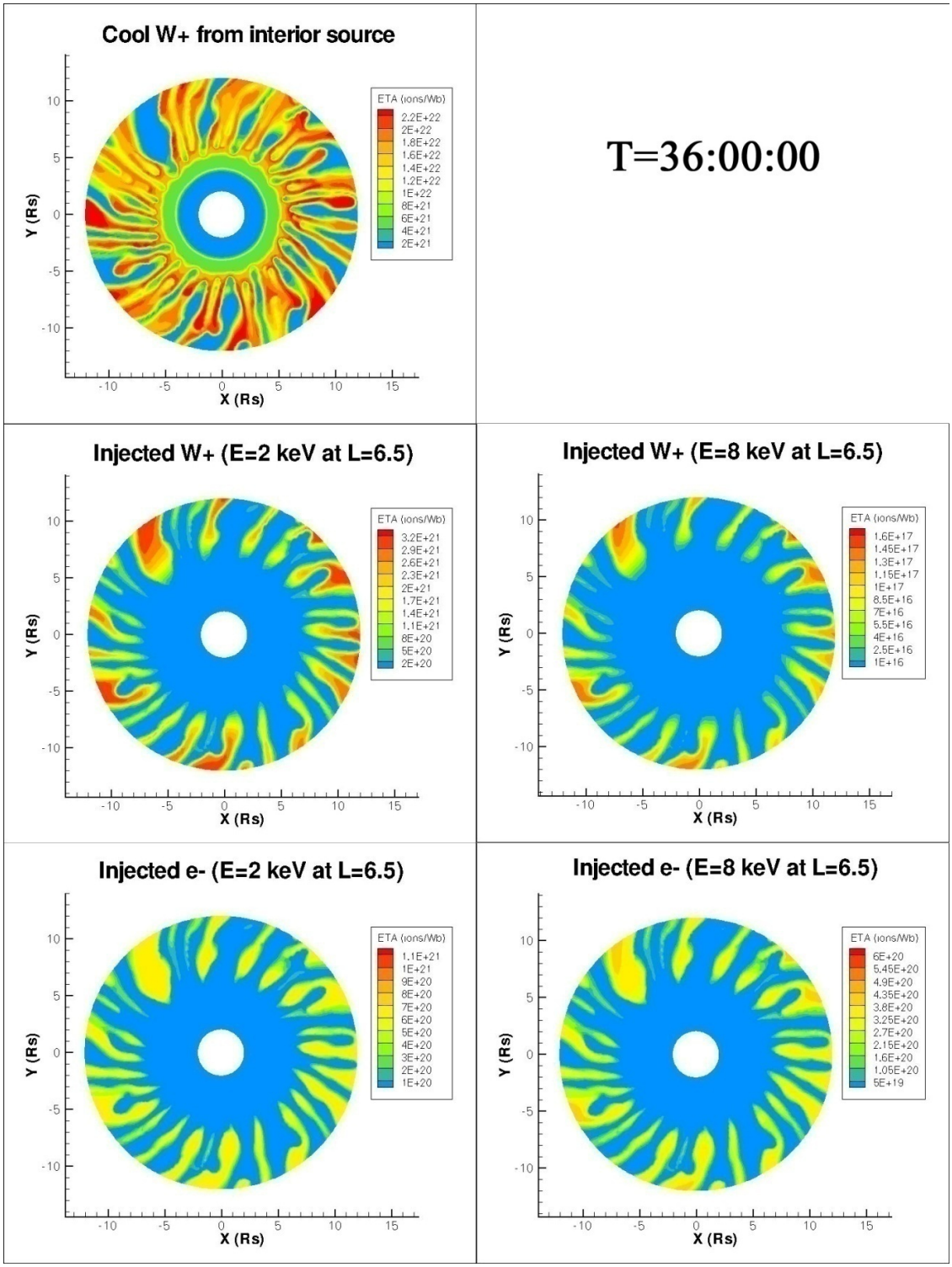

Figure 6.7 Same as Figure 6.3 but at T = 36:00:00.

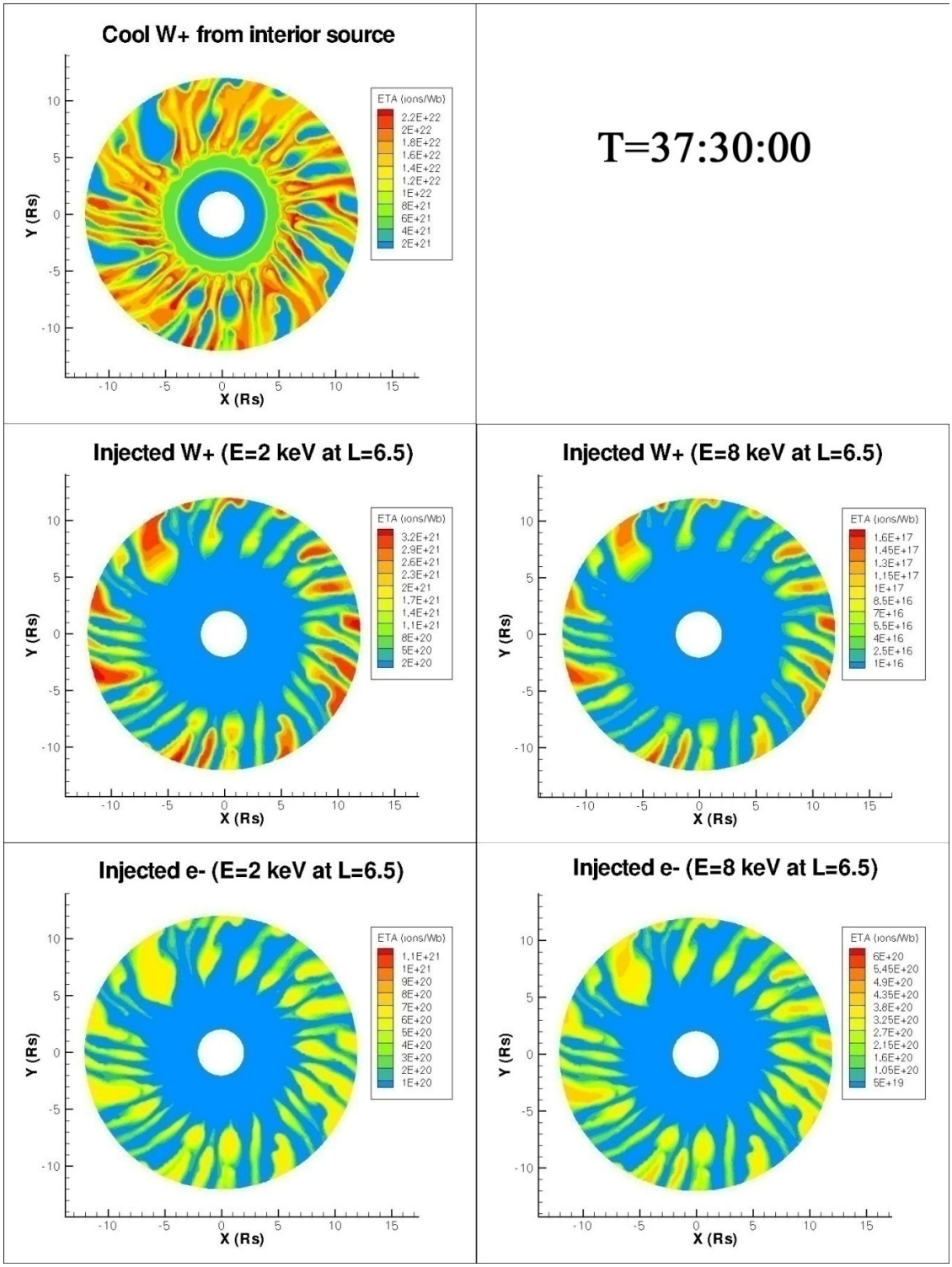

Figure 6.8 Same as Figure 6.3 but at T = 37:30:00.

6.3. Simulation of injection-dispersion signatures

6.3.1. Capture process

η distributions alone are not sufficient to simulate the energy spectrograms of injection-dispersion events. For this purpose we need to introduce a set of test particles, track their trajectories, and replicate the capture process of the hot plasma by the spacecraft Cassini. During the capture process, the V structures are swept past the spacecraft at the local plasma rotational speed, which is much larger than either the spacecraft speed relative to Saturn or the gradient-curvature drift speed [*Hill et al.,* 2005]. Therefore in the rotating frame, Cassini moves westward in the azimuthal direction at a more-or-less fixed radial distance. To directly compare with Figure 6.2, we assume Cassini's radial location is at $L = 6.5$ and its angular speed is Saturn's rotation speed

$$L_C = 6.5 \tag{6.7a}$$

$$\varphi_C = \varphi_{C0} - \Omega t \tag{6.7b}$$

where Ω is Saturn's rotation speed, and φ_{C0} is Cassini's initial longitude at $t = 0$.

A test particle is represented as

$$P(\lambda, \tau, L_0, \varphi_0) \tag{6.8}$$

where λ is the energy invariant of the test particle, and τ , L_0, and φ_0 are the initial time, radial position, and angular position of the injection. Figure 6.9 shows the capture process of an injection event. All four particles P_1 – P_4 are injected at the same L_0 and φ_0. P_1 and P_2 are high energy W^+, but injected at different times τ_1 and τ_2, respectively. P_3 and P_4 are high energy e^- injected at τ_1 and τ_2, respectively. We assume that Cassini (at L = 6.5) first captures P_1 at time T_1 (top panel), and finally captures P_4 at time T_2 (bottom panel). P_2 and P_3 are missed by the spacecraft. Between T_1 and T_2, hot plasma with lower energies is captured. The capture process indicates that a test particle stream of finite duration is needed to occupy a finite range of energy channels in the captured hot plasma. By trial and error we found that this required a test particle stream lasting at least a half hour.

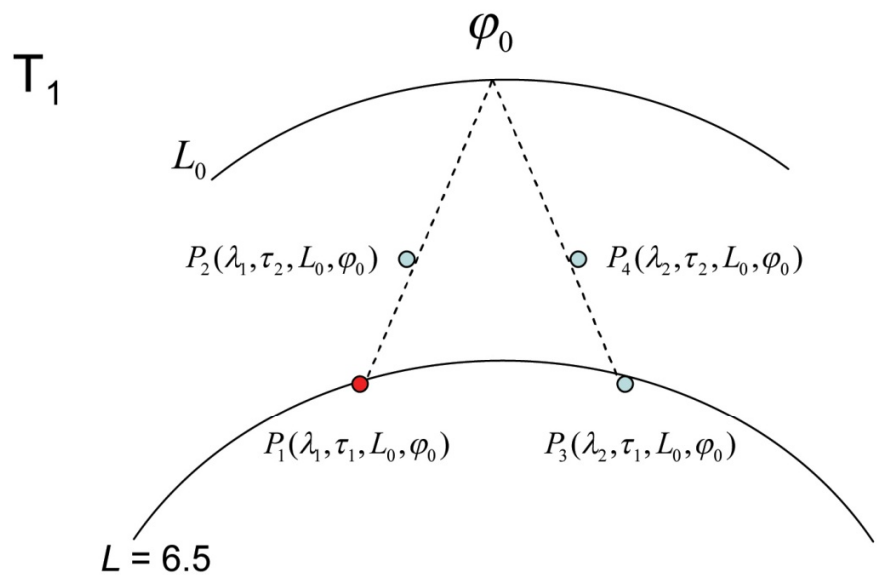
T1
φ_0
L_0
$P_2(\lambda_1,\tau_2,L_0,\varphi_0)$
$P_4(\lambda_2,\tau_2,L_0,\varphi_0)$
$P_1(\lambda_1,\tau_1,L_0,\varphi_0)$
$P_3(\lambda_2,\tau_1,L_0,\varphi_0)$
L = 6.5

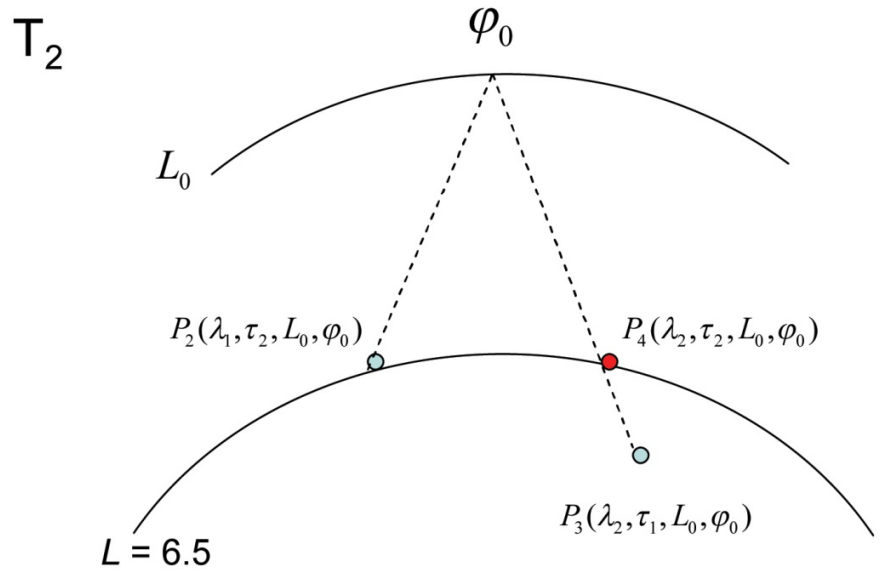
T2
φ_0
L_0
$P_2(\lambda_1,\tau_2,L_0,\varphi_0)$
$P_4(\lambda_2,\tau_2,L_0,\varphi_0)$
$P_3(\lambda_2,\tau_1,L_0,\varphi_0)$
L = 6.5

Figure 6.9 Schematic illustration of the capture process of a test particle stream by the spacecraft. Top panel: P_1 is captured at time T_1. Bottom panel: P_4 is captured at time T_2.

6.3.2. Injection-dispersion signatures

The task has two steps. (1) Find an injection event, for which the hot plasma can move inward and pass through L = 6.5, while their trajectories do not change too much during a half hour time interval. (2) Add the test particle stream and follow Cassini as it captures different energy particles at different times.

We add test particles in 8 channels (4 channels for each species W^+ and e^-). To compare with Figure 6.2, the energy invariants λ are chosen to correspond to 2, 4, 6, and 8 keV at L = 6.5. According to Figures 6.3 – 6.8, the hot plasma starts to be injected from L = 12 at some time between 29 hrs and 31 hrs. Therefore, the initial times of injection τ are taken to be at every 10 minutes from 30 hrs to 32 hrs. The initial radial positions of injection are all at L_0 = 12, and the initial angular positions φ_0 are spaced at every 5 degrees of longitude. Among the 936 events simulated (comprising 7488 injected particles), it is rare to find an injection event for which all energy channels can pass through L = 6.5. The more energy an injected particle has, the farther it drifts in the azimuthal direction. In most cases, the high energy particles drift into an adjacent outflow sector before completing their inward $\mathbf{E}\times\mathbf{B}$ drift, a real effect that limits their inward excursion, and affects the simulated energy-time dispersion signature that we are constructing. In the case of Figure 6.2 and our current simulation, if an injected particle cannot drift inward and pass through L = 6.5, it cannot be captured by the spacecraft.

Among these injection events, the one with the best results is τ = 31:20:00, L_0 = 12, and φ_0 = 140°. Figure 6.10 shows the 8 trajectories of this event. In panel a, the solid black curve represents L = 6.5, the position where the spacecraft Cassini is assumed to be. Panel b is a magnified view of the dashed rectangle area in panel a. It shows clearly the energy-longitude drift dispersion that produces the observed energy-time signatures. Figure 6.11 shows trajectories of test particles injected at the same position, but after a half hour at τ = 31:50:00. Trajectories in Figure 6.11 are similar to those in Figure 6.10.

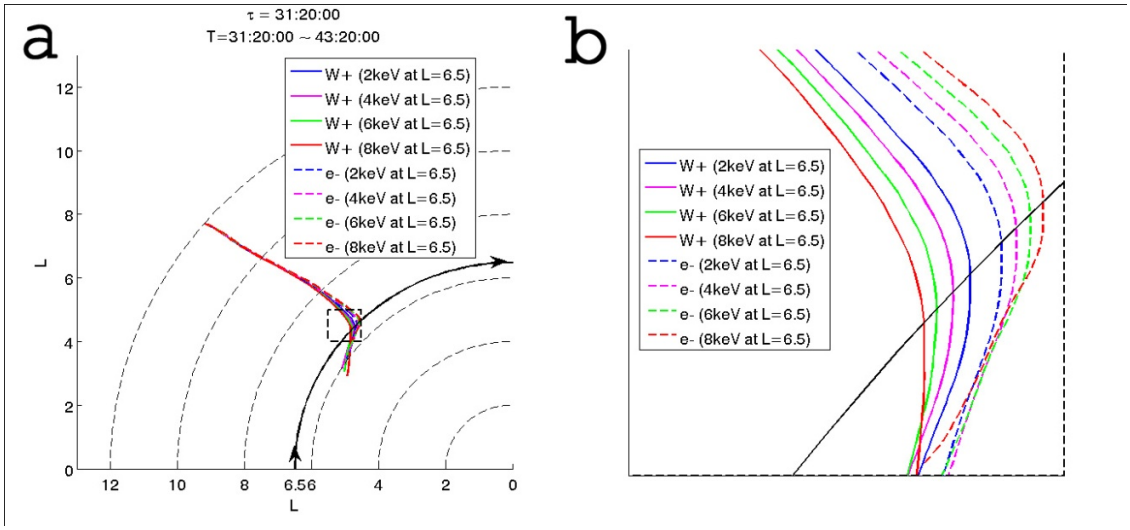

Figure 6.10 Panel a: trajectories of 8 hot plasma channels. Hot plasma is injected at τ = 31:20:00, L_0 = 12, and φ_0 = 140°. Panel b: magnified view of the dashed rectangle area in panel a.

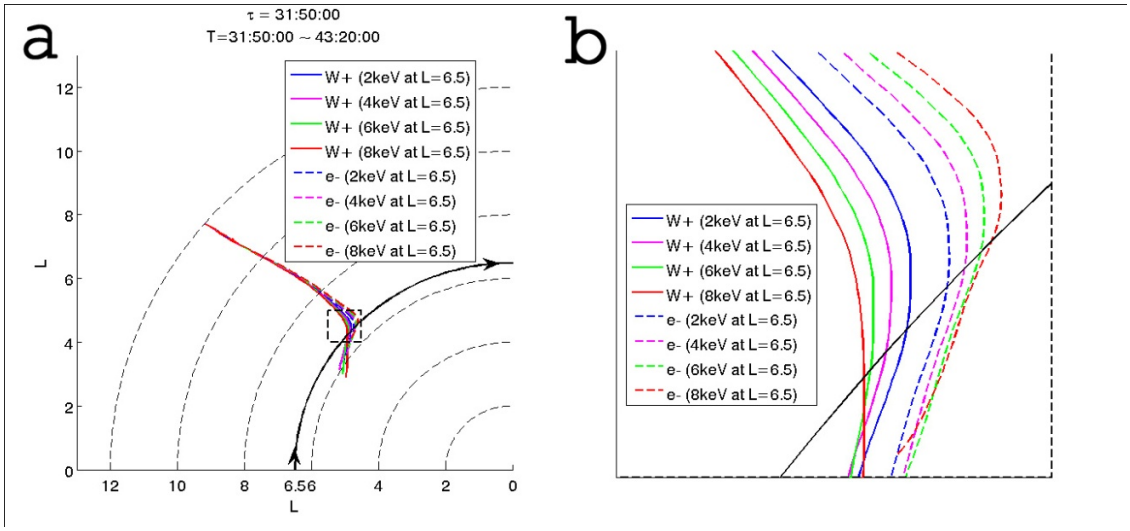

Figure 6.11 Same as Figure 6.10, but the hot plasma is injected a half hour later at τ = 31:50:00.

The next step is to inject a test particle stream at L_0 = 12, φ_0 = 140° from τ = 31:20:00 to τ = 31:50:00, and then follow Cassini's position as it captures injected test particles. When a test particle is captured, we record the longitudinal position, the simulation time, and the energy of the particle. Figure 6.12 shows the energy-longitude and energy-time spectrogram of our simulation.

Notice that the x-axis of longitude φ has a reverse direction. The four solid circles are four channels of hot W^+ drifting eastward, and the four diamonds are four channels of hot e^- drifting westward. Particles with higher energy drift further in longitude. The solid and dashed lines are linear fits to the four stars and four circles, respectively. The point of intersection of the two lines is right on the zero energy axis, as it should be, because plasma with zero energy (either W^+ or e^-) has no gradient-curvature drift and thus no longitudinal dispersion. This point indicates the position (~136.7°) and

time (~38:38:00) of the capture of plasma with zero energy (if there is any). Remember that the hot plasma is added at $\varphi_0 = 140^o$. This longitudinal displacement is caused by the $\mathbf{E} \times \mathbf{B}$ drift for all channels of hot plasma, which also can be found in the hot plasma trajectories in Figures 6.10 and 6.11. The fit equations indicate that the V-shaped signature is not perfectly symmetric, which is consistent with the discussion about the capture process. Different test particles are captured at different positions and times, and their initial injection times are also different. The $\mathbf{E} \times \mathbf{B}$ drift history is slightly different for each test particle, because the convection pattern is changing every moment. The slopes of the two fit lines are 3.6 and 3.7 keV/degree, which is ~2 keV/min of UT, almost equal to the slopes of the left two V-shaped signatures in Figure 6.2.

Figure 6.13 is a comparison of energy spectrograms between the injection event in the simulation and the left most one in the observed results (Figure 6.2). In panel a, the V-shape signature from simulation results is split into 2 parts: W^+ and e^-. The time interval is scaled to half hour. Panel b is a half hour interval cut from the left side of Figure 6.2. The slopes in 2 panels are almost the same, indicating that the 2 injection-dispersion events are in the same age.

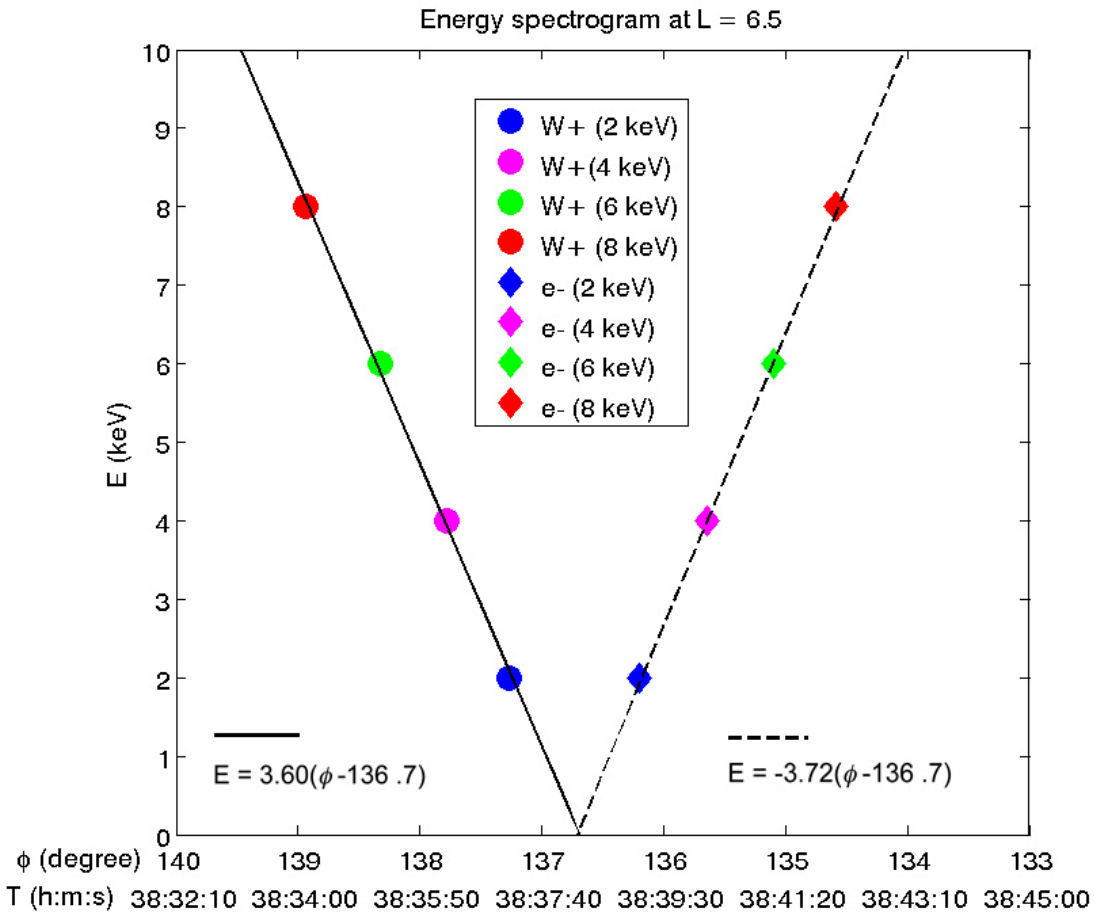

Figure 6.12 Linear energy-longitude and energy-time spectrogram of injected hot plasma from the RCM-S simulations.

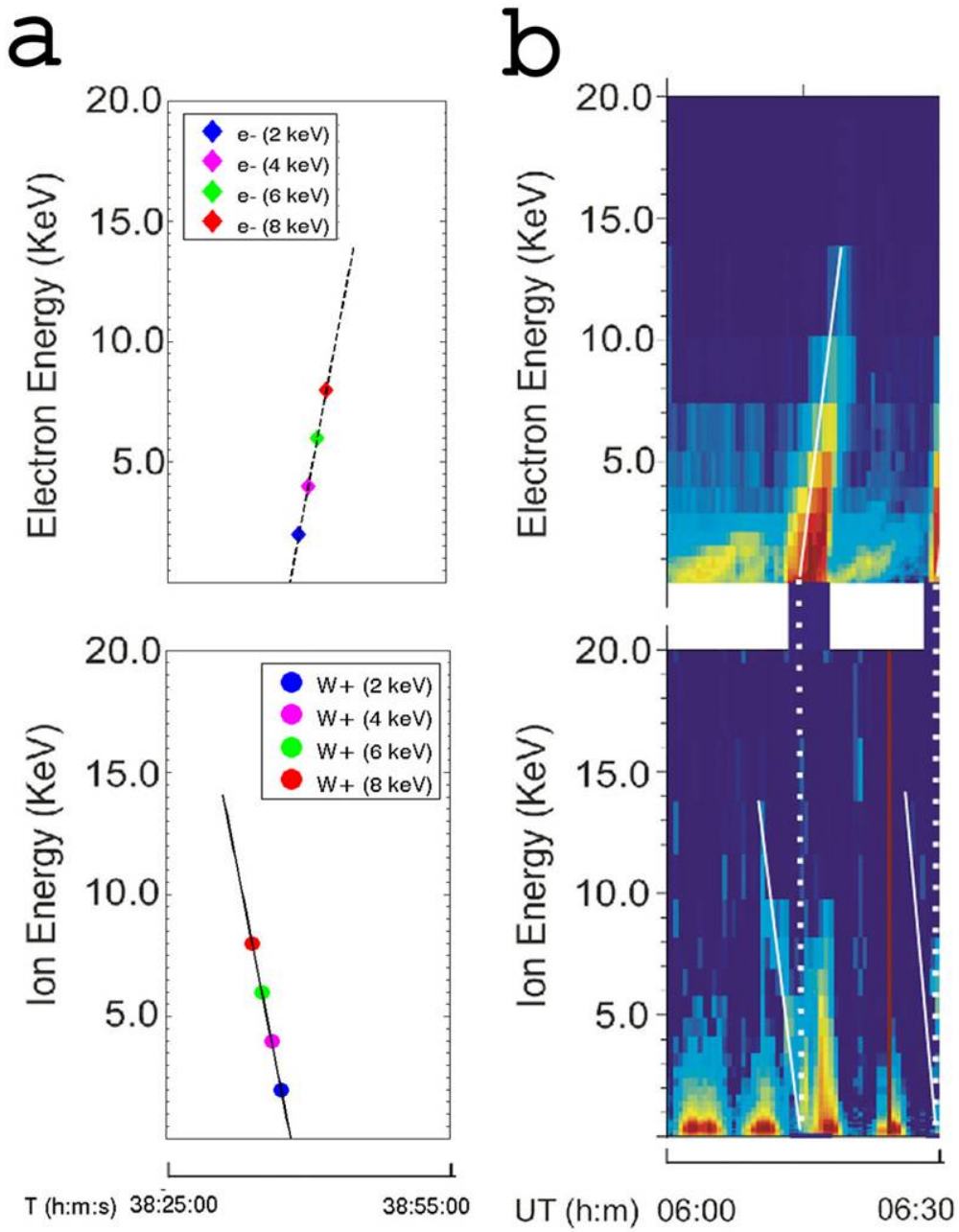

Figure 6.13 Comparison of energy spectrograms between the injection event in the simulation and the left most one in the observed results (Figure 6.2).

6.4. Summary

The injection-dispersion events have been widely accepted as evidence for rotationally driven interchange convection at Saturn. We have included the hot tenuous plasma and the relative gradient-curvature drift in the RCM-S to simulate the fine scale V-shaped signatures.

The deep injection event is a rare occurrence, because the high-energy hot plasma often drifts into an adjacent outflow sector before completing the inward $\mathbf{E}\times\mathbf{B}$ drift. The capture process of hot plasma by Cassini apparently requires a test particle stream that lasts at least a half hour. We analyzed the trajectories of 936 injection events (7488 injected test particles) to find the most favorable position and time of injection. Then we replicated the capture process that happens in the real world. The energy-longitude and energy-time spectrogram from our simulation shows a clear V-shape. The peak of the V is right on the zero energy axis, consistent with the fact that plasma with zero energy has no longitudinal dispersion. The slight asymmetry of the V-shaped signature is consistent with the fact that different hot particles are captured at different positions and times, and their initial injection times are also different. The slopes of the V shape of our simulation are almost equal to the slopes of the left most V shape of observations in Figure 6.2, indicating that the 2 injection events are in the same age.

In future work, we hope to simulate a larger set of injection events, and statistically compare the simulated results with observations.

Chapter 7

Conclusions

Saturn's magnetosphere is unique in the solar system. The rotation-driven convection makes it different from Earth. The continuously active distributed cool plasma source makes it different from Jupiter. Saturn's magnetospheric convection pattern consists of wider, slower outflow channels of cooler, denser plasma alternating with narrower, faster inflow channels of hotter, more tenuous plasma. The earliest, and the most definitive, evidence is the ubiquitous injection-dispersion events that are observed on every pass of the Cassini spacecraft through the inner magnetosphere, which is also the final objective of this project.

This thesis shows a step-by-step effort to achieve the final objective. The numerical model RCM-S, adapted from its original Earth version RCM, is used to simulate the plasma convection. In the initial simulation, only cool plasma is considered, and its temperature is assumed to be zero. The simulation results confirm the convection pattern in Saturn's inner magnetosphere, and quantitatively agree with observed results

from CAPS in many aspects, such as inflow longitudinal width ratio, inflow and outflow radial velocities, and azimuthal corotation lag.

More work was then done to develop and improve RCM-S. Three cool plasma source models have been tested. The one giving the best simulation results is also modified (scaled up by 10 times) to keep consistent with more recent observed data. The finite temperature and associated cool plasma pressure has been included, which turn out to be an extra driving force of the magnetospheric convection system. The effect of ionospheric Pedersen conductance, which constrains the radial velocities of plasma flow and the growth rate of the convection pattern, has been investigated. Many improvements can be made in future work. For example, the distortion of the otherwise dipolar magnetic field and the asymmetry of ionospheric Pedersen conductance can be included to investigate the effects of local time asymmetry on the development of the centrifugal interchange instability.

Finally, hot plasma was added in the simulations. Because the cool plasma from the interior source is much denser than the hot plasma, the basic convection pattern does not change much after including the tenuous hot plasma. In an injection event, particles in different energy channels are captured by the spacecraft Cassini at different times and positions; therefore test particle streams are necessary to reproduce the capture process. The energy spectrograms of captured water group ions and electrons form a V-shape signature of the injection-dispersion event. The slope of the V from simulation results is almost the same as that of the left most V-shape in observed results (Figure 6.2), which means those two injection events could have the same age.

The final result of this project is just the starting point of a new project. Because deep injection events are very rare, a straightforward continuing objective will be finding more deep injection events and comparing simulated V-shape signatures with more observed ones.

Bibliography

André, N., M. K. Dougherty, C. T. Russell, J. S. Leisner, and K. K. Khurana (2005), Dynamics of the Saturnian inner magnetosphere: first inferences from the Cassini magnetometers about small-scale plasma transport in the magnetosphere, *Geophys. Res. Lett.*, 32, L14S06, doi:10.1029/2005GL022643.

Brice, N. M., Ioannidis, G. A. (1970), The magnetospheres of Jupiter and Earth, *Icarus*, 13, pp. 173-183.

Burch, J. L., J. Goldstein, T. W. Hill, D. T. Young, F. J. Crary, A. J. Coates, N. André, W. S. Kurth, and E. C. Sittler (2005), Properties of local plasma injections in Saturn's magnetosphere, *Geophys. Res. Lett.*, *32*, L14S02, doi: 10.1029/2005GL022611.

Cassidy, T.A., and R. E. Johnson (2010), Collisional spreading of Enceladus' neutral cloud, *Icarus*, doi: 10.1016/j.icarus.2010.04.010.

Chen, Y., and T. W. Hill (2008), Statistical analysis of injection/dispersion events in Saturn's inner magnetosphere, *J. Geophys. Res.*, *113*, A07215, doi: 10.1029/2008JA013166.

Chen, Y., T. W. Hill, A. M. Rymer, and R. J. Wilson (2010), Rate of radial transport of plasma in Saturn's inner magnetosphere, *J. Geophys. Res., 115*, A10211, doi:10.1029/2010JA015412.

Dungey, J. W. (1961), Interplanetary magnetic field and the auroral zones, *Phys. Rev. Lett.*, 6, pp. 47-48.

Gold, T. (1959), Motions in the magnetosphere of the Earth, *J. Geophys. Res.*, Vol. 64, No. 9, pp. 1219-1224

Goldreich, P., and A. J. Farmer (2007), Spontaneous axisymmetry breaking of the external magnetic field of Saturn, *J. Geophys. Res.*, *112*, A0525, doi:10.1029/2006JA012163.

Gurnett, D. A., A. M. Persoon, W. S. Kurth, J. B. Groene, T. F. Averkamp, M. K. Dougherty, and D. J. Southwood (2007), The variable rotation period of the inner region of Saturn's plasma disk, *ScienceExpress*, doi: 10.1126/science.1138562

Hill, T. W., A. J. Dessler, and F. C. Michel (1974), Configuration of the Jovian magnetosphere, *Geophys. Res. Lett.*, Vol. 1, No. 1, pp. 3-6.

Hill, T. W., and F. C. Michel (1976), Heavy ions from Galilean satellites and the centrifugal distortion of the Jovian magnetosphere, *J. Geophys. Res.*, *81*(A25), 4561–4565.

Hill, T. W. (1979), Inertial limit on corotation, *J. Geophys. Res.*, *84*(A11), 6554–6558.

Hill, T. W. (1980), Corotation lag in Jupiter's magnetosphere: Comparison of observation and theory, *Science*, *207*, 301–302, doi: 10.1126/science.207.4428.301.

Hill, T. W., A. J. Dessler, and L. J. Maher (1981), Corotating magnetospheric convection, *J. Geophys. Res.*, **86**, 9020, l98l.

Hill, T. W. (1983), Rotationally-induced Birkeland current systems, in *Magnetospheric Currents*, (T. A. Potemra, ed.) *Geophysical Monograph* **28**, pp. 340-349, American Geophysical Union, Washington, D.C.

Hill, T. W. (1984), Saturn's E ring, *Adv. Space Res*. Vol. 4, No. 9, pp. 149-157.

Hill, T. W., Dessler, A. J. (1991), Plasma motions in planetary magnetospheres, *Science*, Vol. 252, No. 5004, pp. 410-415.

Hill, T. W., A. M. Rymer, J. L. Burch, E. J. Crary, D. T. Young, M. F. Thomsen, D. Delapp, N. André, A. J. Coates, and G. R. Lewis (2005), Evidence for rotationally driven plasma transport in Saturn's magnetosphere, *Geophys. Res. Lett. 32,* L14S10, doi: 10.1029/2005GL022620.

Hill, T. W. (2006), Effect of the acceleration current on the centrifugal interchange instability, *J. Geophys. Res*., *111*, A03214, doi:10.1029/2005JA011338

Hill, T. W. (2009), Speed limit for centrifugally driven convection, *AGU 2009 Fall Meeting*, SM31D-08.

Huang, T. S., and T. W. Hill (1991), Drift-wave instability in the Io plasma torus, *J. Geophys. Res.*, 96, 14075-14083.

Johnson, R. E., H. T. Smith, O. J. Tucker, M. Liu, M. H. Burger, E. C. Sittler, R. L. Tokar, (2006), The Enceladus and OH tori at Saturn, *Astrophys. J., 644*, L137, doi: 10.1086/505750.

Liu, X., T. W. Hill, R. A. Wolf, S. Sazykin, R. W. Spiro, and H. Wu (2010), Numerical simulation of plasma transport in Saturn's inner magnetosphere using the Rice Convection Model, *J. Geophys. Res., 115*, A12254, doi: 10.1029/2010JA015859.

Liu, X., and T. W. Hill (2012), Effects of finite plasma pressure on centrifugally driven convection in Saturn's inner magnetosphere, *J. Geophys. Res., 117*, A07216, doi:10.1029/2012JA017827.

Lyon, J. G. (2000), The solar wind-magnetosphere-ionosphere system, *Science*, Vol. 288, No. 5473, pp. 1987-1991, doi: 10.1126/science.288.5473.1987.

Mauk, B. H., et al. (2005), Energetic particle injections in Saturn's magnetosphere, *Geophys. Res. Lett.*, *32*, L14S05, doi: 10.1029/2005GL022485.

Mauk, B. H., D. C. Hamilton, T. W. Hill, G. B. Hospodarsky, R. E. Johnson, C. Paranicas, E. Roussos, C. T. Russell, D. E. Shemansky, E. C. Sittler Jr., and R. M. Thorne (2009), Fundamental plasma processes in Saturn's magnetosphere, in *Saturn from Cassini-Huygens*, edited by M. K. Dougherty, L. W. Esposito, and S. M. Krimigis, chapt. 11, pp. 281-331, doi: 10.1007/978-1-4020-9217-6_11.

Moore, L., I. Mueller-Wodarg, M. Galand, A. Kliore, and M. Mendillo (2010), Latitudinal variations in Saturn's ionosphere: Cassini measurements and model comparisons, *J. Geophys. Res.,* doi:10.1029/2010JA015692.

Pontius, D. H., and T. W. Hill (1982), Departure from corotation of the Io plasma torus: Local plasma production, *Geophys. Res. Lett.*, *9*(12), 1321–1324.

Pontius, D. H., Jr. (1997), Coriolis influences on the interchange instability, *Geophys. Res. Lett., 24*(23), 2961-2964.

Pontius, D. H., Jr., and T. W. Hill (2006), Enceladus: A significant plasma source for Saturn's magnetosphere, *J. Geophys. Res.*, 111, A09214, doi: 10.1029/2006JA011674.

Pontius, D. H., Jr., and T. W. Hill (2009), Plasma mass loading from the extended neutral gas torus of Enceladus as inferred from the observed plasma corotation lag, *Geophys. Res. Lett.*, *36*, L23103, doi: 10.1029/2009GL041030.

Rayleigh, Lord (John William Strutt) (1883), Investigation of the character of the equilibrium of an incompressible heavy fluid of variable density, *Proceedings of the London Mathematical Society*, Vol. 14, pp. 170-177, doi: 10.1112/plms/s1-14.1.170

Saur, J., B. H. Mauk, A. Kaßner, and F. M. Neubauer (2004), A model for the azimuthal plasma velocity in Saturn's magnetosphere, *J. Geophys. Res.*, *109*, A05217, doi: 10.1029/2003JA010207.

Schippers, P., M. Blanc, N. André, I. Dandouras, G. R. Lewis, L. K. Gilbert, A. M. Persoon, N. Krupp, D. A. Gurnett, A. J. Coates, S. M. Krimigis, D. T. Young, and M. K. Dougherty (2008), Multi-instrument analysis of electron populations in Saturn's magnetosphere, *J. Geophys. Res.*, *113*, A07208, doi:10.1029/2008JA013098.

Shemansky, D. E., P. Matheson, D. T. Hall, H.-Y. Hu, and T. M. Tripp (1993), Detection of the hydroxyl radical in the Saturn magnetosphere, *Nature*, *363*, 329.

Siscoe, G. L., and D. Summers (1981), Centrifugally driven diffusion of Iogenic plasma, *J. Geophys. Res.*, *86*, 8471-8479.

Sittler, E. C., *et al*. (2005), Preliminary results on Saturn's inner plasmasphere as observed by Cassini: Comparison with Voyager, *Geophys. Res. Lett.*, *32*, L14S07, doi:10.1029/2005GL002653.

Smith, H. T., R. E. Johnson, M. E. Perry, D. G. Mitchell, R. L. McNutt, and D. T. Young (2010), Enceladus plume variability and the neutral gas densities in Saturn's magnetosphere, *J. Geophys. Res., 115*, A10252, doi:10.1029/2009JA015184.

Sonnerup, B. U. Ö., and M. J. Laird (1963), On magnetospheric interchange instability, *J. Geophys. Res.*, Vol. 68, No. 1, pp. 131-139.

Taylor, Geoffrey (1950), The instability of liquid surfaces when accelerated in a direction perpendicular to their planes, *Proceedings of the Royal Society of London. Series A, Mathematical and Physical Sciences*, Vol. 201, No. 1065, pp. 192-196, doi: 10.1098/rspa.1950.0052

Thomsen, M. F., D. B. Reisenfeld, D. M. Delapp, R. L. Tokar, D. T. Young, F. J. Crary, E. C. Sittler, M. A. McGraw, and J. D. Williams (2010), Survey of ion plasma parameters in Saturn's magnetosphere, *J. Geophys. Res.*, *115*, A10220, doi:10.1029/2010JA015267.

Toffoletto, F., S. Sazykin, R. W. Spiro, and R. A. Wolf (2003), Inner magnetospheric modeling with the Rice Convection Model, *Space Sci. Rev.*, *107*, 175–196.

Vasyliūnas, V. M. (1970), Mathematical models of magnetospheric convection and its coupling to the ionosphere, in *Particles and Fields in the Magnetosphere*, edited by B. M. MacCormac, pp. 395–453, Springer, New York.

Vasyliūnas, V. M. (1978), A mechanism for plasma convection in the inner Jovian magnetosphere (abstract), STP Symposium, Book of Abstracts, Innsbruck, Austria, June 1978.

Vasyliūnas, V. M. (1983), Plasma distribution and flow, in *Physics of the Jovian Magnetosphere,* A. J. Dessler, ed., Cambridge University Press, chapt. 11, pp. 395-453.

Vasyliūnas, V. M. (1994), Role of the plasma acceleration time in the dynamics of the Jovian magnetosphere, *Geophys. Res. Lett., 21*(6), 401-404.

Wilson, R. J., R. L. Tokar, M. G. Henderson, T. W. Hill, M. F. Thomsen, and D. H. Pontius (2008), Cassini plasma spectrometer thermal ion measurements in Saturn's inner magnetosphere, *J. Geophys. Res.*, *113*, A12218, doi:10.1029/2008JA013486.

Wilson, R. J., R. L. Tokar, and M. G. Henderson (2009), Thermal ion flow in Saturn's inner magnetosphere measured by the Cassini plasma spectrometer: A signature of the Enceladus torus, *Geophys. Res. Lett.*, *36*, L23104, doi: 10.1029/2009GL040225.

Wolf, R. A. (1983), The quasi-static (slow-flow) region of magnetosphere, in *Solar-Terrestrial Physics*, edited by R. L. Carovillano and J. M. Forbes, pp. 303–368, Springer, New York.

Wolf, R. A., R. W. Spiro, S. Sazykin, F. R. Toffoletto, P. Le Sager, and T. S. Huang (2006), Use of Euler potentials for describing magnetosphere-ionosphere coupling, *J. Geophys. Res.*, *111*, A07315, doi:10.1029/2005JA011558.

Wu, H., T. W. Hill, R. A. Wolf, and R. W. Spiro (2007), Numerical simulation of fine structure in the Io plasma torus produced by the centrifugal interchange instability, *J. Geophys. Res.*, *112*, A02206, doi:10.1029/2006JA012032.

Yang, Y. S., R. A. Wolf, R. W. Spiro, T. W. Hill, and A. J. Dessler (1994), Numerical simulation of torus-driven plasma transport in the Jovian magnetosphere, *J. Geophys. Res.*, *99*(A5), 8755–8770.

Young, D. T., et al. (2005), Composition and dynamics of plasma in Saturn's magnetosphere, *Science, 307*, 1262-1266, doi: 10.1126/science.1106151.

Appendix A: Magnetospheric current

We begin with the MHD momentum equation, written in the frame of reference that corotates with the planet:

$$\rho \frac{d\mathbf{v}}{dt} = \mathbf{j} \times \mathbf{B} - \nabla p + \rho \Omega^2 \mathbf{r}_e - 2\rho \boldsymbol{\Omega} \times \mathbf{v} - \dot{\rho}_s (\boldsymbol{\Omega} \times \mathbf{r}_e + \mathbf{v} - \mathbf{v}_n) \tag{A1}$$

where ρ is the mass density of the plasma, p is its pressure, $\mathbf{v}$ is its bulk flow velocity with respect to the corotating frame, $\mathbf{r}_e$ is the vector displacement from the rotation axis $\boldsymbol{\Omega}$ (assumed to be coincident with the magnetic dipole axis), $\dot{\rho}_s$ is the rate of plasma mass loading per unit volume due to both charge exchange and new ionization, and $\mathbf{v}_n$ is the Kepler orbital velocity of the neutral molecules before ionization or charge exchange. The five terms on the right are, respectively, the bulk Lorentz force, the pressure-gradient force, the centrifugal force of corotation, the Coriolis force, and the rate of addition (per unit volume) of new plasma momentum due to chemical reactions. The centrifugal and Coriolis forces are often called "pseudo-forces" because, when the equation, and $\mathbf{v}$ itself, are transformed to the inertial (nonrotating) frame, these two terms become part of the acceleration term (left side). (The other terms on the right are invariant to this frame transformation.) It is, however, a great mathematical convenience, in a rapidly rotating magnetosphere, to calculate $\mathbf{v}$ relative to the corotating frame and, accordingly, to include the centrifugal and Coriolis terms as explicit forces on the right side of the equation.

We now set the left side of (A1) equal to zero, i.e., we neglect the acceleration as measured in the corotating frame, compared to the much larger centripetal and Coriolis accelerations that would be measured in the inertial frame, which are included explicitly in the third and fourth terms on the right side of (A1). This is a reasonable approximation when the convection speed $|\mathbf{v}|$ measured in the corotating frame is $<\sim \Omega r_e$ and $|d\mathbf{v}/dt| <\sim \Omega^2 r_e$ [*Hill*, 1983, 2006], conditions that are satisfied in our simulation results reported here. There is a non-zero acceleration (in the corotating frame) associated with the observed corotation lag [*Wilson et al.*, 2008, 2009], and the lag itself is significant compared to Ωr, but the associated acceleration (in the corotating frame) is insignificant compared to $\Omega^2 r$ because $v_r \partial \mathrm{v}_\varphi / \partial_r << \Omega v_\varphi$.. We also neglect the pressure-gradient force (the "cold plasma" approximation), not because it is necessarily negligible in Saturn's inner magnetosphere, but because we want to investigate the novel effects produced by the rotationally driven terms. (We will re-instate the pressure term in Chapter 5.) With these two approximations, we take the cross product of **B** with (A1), and integrate the resulting equation across the equatorially confined plasma sheet, to obtain

$$\mathbf{J}_\perp = \eta \Omega^2 r_e \hat{\boldsymbol{\varphi}} + \dot{\eta}_s (\Omega r_e - v_n)\hat{\mathbf{r}} + 2\eta\Omega\mathbf{v} + \dot{\eta}_s \mathbf{B}_e \times \mathbf{v} / B_e \qquad \text{(A2)}$$

where $\mathbf{J}_\perp$ is the equatorial plasma-sheet current perpendicular to **B**, integrated along **B** across the sheet thickness, (r,θ,φ) is a spherical coordinate system aligned with the magnetic and spin axes, and

$$\eta = \int \rho ds / B\,, \quad \dot{\eta}_s = \int \dot{\rho}_s ds / B \tag{A3}$$

are the mass content per unit magnetic flux, and the local source thereof. (A2) is equivalent to (2.1) of the text. Note the different units of upper-case **J** and lower-case **j**:

$$\mathbf{J} = \int \mathbf{j} ds \tag{A4}$$

In (A2) the "pick-up current" (proportional to $\dot{\eta}_s$) has been split into two pieces, one that is independent of **v** (the second term on the right side) and one that is not (the fourth term). This is because, as noted in the text, numerical instabilities arise (not unexpectedly) when **v** from the previous time step is used to calculate $\mathbf{J}_\perp$ for the present time step, which will in turn be used to calculate **v** for the present time step, and thence to advance η to the next time step. To surmount this numerical (and logical) difficulty we have devised mathematically equivalent ways to implicitly incorporate the value of **v** appropriate to the present time step in our calculation of $\mathbf{J}_\perp$. This involves the addition of an artificial (negative) contribution to the ionospheric Hall conductance (Appendix B) to incorporate the Coriolis current (the third term on the right side of (A2)), and an artificial (positive) contribution to the ionospheric Pedersen conductance (Appendix C) to

incorporate the velocity-dependent part of the pick-up current (the fourth term on the right side of (A2)).

Appendix B: Coriolis current

The third term on the right side of (A2):

$$\mathbf{J}_C \equiv 2\eta\Omega\mathbf{v} \tag{B1}$$

(the "Coriolis current") has a divergence

$$\begin{aligned} \nabla\cdot\mathbf{J}_C &= \frac{1}{r_e}\frac{\partial}{\partial r_e}\left(r_e J_{C,r}\right) + \frac{1}{r_e}\frac{\partial}{\partial\varphi}\left(J_{C,\varphi}\right) \\ &= \frac{2\Omega}{r_e}\left[\frac{\partial}{\partial r_e}\left(r_e\eta v_r\right) + \frac{\partial}{\partial\varphi}\left(\eta v_\varphi\right)\right] \end{aligned} \tag{B2}$$

where (r_e,φ,z) is a cylindrical coordinate system aligned with (r,θ,φ). If Φ is the electrostatic potential (taken to be a field-line invariant), then

$$\mathbf{v} = \frac{\mathbf{E}\times\mathbf{B}}{B^2} = \frac{\mathbf{B}\times\nabla\Phi}{B^2} \tag{B3}$$

and (B2) becomes

$$\nabla \cdot \mathbf{J}_C = \frac{2\Omega}{r_e}\left[\frac{\partial}{\partial r_e}\left(\frac{\eta}{B_e}\right)\frac{\partial \Phi}{\partial \varphi} - \frac{\partial}{\partial \varphi}\left(\frac{\eta}{B_e}\right)\frac{\partial \Phi}{\partial r_e}\right] \tag{B4}$$

using the fact that $\mathbf{B} = -B_e\hat{\mathbf{z}}$ at the equatorial plane. (The two mixed-derivative terms, proportional to $\partial^2\Phi/\partial r_e \partial\varphi$, conveniently cancel.)

For mapping between the equatorial current sheet and the planetary ionosphere, it is convenient to express **B** in terms of Euler potentials (α, β):

$$\mathbf{B} = \nabla\alpha \times \nabla\beta \tag{B5}$$

where, for a spin-aligned dipole field,

$$\alpha = \frac{M\sin^2\theta}{r}, \quad \beta = \varphi \tag{B6}$$

both of which are field-line invariants by (B5). (M is the planetary dipole magnetic moment.) In the equatorial plane, $\sin\theta = 1$, $\alpha = M/r_e$, and

$$\frac{\partial}{\partial r_e} = -\frac{M}{r_e^2}\frac{\partial}{\partial \alpha}, \qquad \frac{\partial}{\partial \varphi} = \frac{\partial}{\partial \beta} \tag{B7}$$

Then (B4) can be written in the equivalent form

$$\nabla \cdot \mathbf{J}_C = -B_e\left[\frac{\partial}{\partial \alpha}\left(\frac{2\Omega\eta}{B_e}\right)\frac{\partial \Phi}{\partial \beta} - \frac{\partial}{\partial \beta}\left(\frac{2\Omega\eta}{B_e}\right)\frac{\partial \Phi}{\partial \alpha}\right] \tag{B8}$$

where $B_e = M/r_e^3$.

This equatorial plasma-sheet current divergence requires a corresponding contribution to the Birkeland (magnetic-field-aligned) current density $j_{\|e}$ flowing into the equatorial plane (from both hemispheres)

$$\delta_C j_{\|e} = \nabla \cdot \mathbf{J}_C \tag{B9}$$

to maintain $\nabla \cdot \mathbf{j} = 0$. The δ_C symbol is appended to emphasize that this is not the total Birkeland current density entering the equatorial current sheet, only the portion of it that is needed to close the divergence of $\mathbf{J}_C$. This equatorial Birkeland current density

contribution implies a radial component of the Birkeland current density contribution just above the ionosphere

$$\delta_C j_{\parallel ir} = \frac{B_{ir}}{B_e}\delta_C j_{\parallel e} = -B_{ir}\left[\frac{\partial}{\partial\alpha}\left(\frac{2\Omega\eta}{B_e}\right)\frac{\partial\Phi}{\partial\beta} - \frac{\partial}{\partial\beta}\left(\frac{2\Omega\eta}{B_e}\right)\frac{\partial\Phi}{\partial\alpha}\right] \tag{B10}$$

as required by the continuity of $j_\parallel/B$ along **B**.

In Saturn's ionosphere ($r = R_S$), a field-line-integrated Hall conductance Σ_H (defined in (D8) below) produces a height-integrated horizontal current density

$$\mathbf{J}_H = \Sigma_H \hat{\mathbf{r}} \times \mathbf{E} = \Sigma_H \nabla_i \Phi \times \hat{\mathbf{r}} \tag{B11}$$

where

$$\nabla_i = \frac{\hat{\boldsymbol{\theta}}}{r}\frac{\partial}{\partial\theta} + \frac{\hat{\boldsymbol{\varphi}}}{r\sin\theta}\frac{\partial}{\partial\varphi} \tag{B12}$$

is the horizontal gradient operator on the spherical shell representing the ionosphere. The form of (B11) is generally valid, independent of latitude (see Appendix D), provided that

Σ_H is defined as the field-line-integrated conductivity (as in the RCM-S), not simply the height-integrated conductivity. The divergence of the Hall current (B11) is

$$\nabla \cdot \mathbf{J}_H = \frac{1}{R_S^{\,2} \sin\theta}\left(\frac{\partial \Sigma_H}{\partial \theta}\frac{\partial \Phi}{\partial \varphi} - \frac{\partial \Sigma_H}{\partial \varphi}\frac{\partial \Phi}{\partial \theta} \right) \tag{B13}$$

where, again, the two mixed derivative terms, proportional to $\partial^2\Phi/\partial\theta\partial\varphi$, cancel conveniently. In the ionosphere (B6) gives

$$\alpha = \frac{M \sin^2\theta}{R_S}, \qquad \frac{\partial}{\partial \theta} = \frac{2M \cos\theta \sin\theta}{R_S}\frac{\partial}{\partial \alpha} \tag{B14}$$

so (B13) can be written in the equivalent form

$$\nabla \cdot \mathbf{J}_H = B_{ir}\left(\frac{\partial \Sigma_H}{\partial \alpha}\frac{\partial \Phi}{\partial \beta} - \frac{\partial \Sigma_H}{\partial \beta}\frac{\partial \Phi}{\partial \alpha} \right) \tag{B15}$$

where $B_{ir} = 2M\cos\theta/R_S^3$.

The divergence of the horizontal ionospheric Hall current (B15) requires a corresponding contribution to the radial component of the Birkeland current density above the ionosphere

$$\delta_H j_{\parallel ir} = -\nabla \cdot \mathbf{J}_H \tag{B16}$$

(The different signs on the right sides of (B9) and (B16) result from the fact that **B** points out of the northern hemisphere ionosphere but into the equatorial plasma sheet from the north; recall that the RCM-S combines the northern and southern ionospheres into a single northern ionosphere having the combined (in parallel) conductance of both. The Birkeland current density $j_{\parallel}$ includes the sign of $\mathbf{j}\cdot\mathbf{B}$.)

Combining (B15) and (B16) gives

$$\delta_H j_{\parallel ir} = -B_{ir}\left(\frac{\partial \Sigma_H}{\partial \alpha}\frac{\partial \Phi}{\partial \beta} - \frac{\partial \Sigma_H}{\partial \beta}\frac{\partial \Phi}{\partial \alpha}\right) \tag{B17}$$

Comparing (B10) with (B17), we see that the effect of including the Coriolis current term on the right side of (2.1) in the text is mathematically equivalent to omitting that term on the right side but instead adding an effective contribution to the Hall conductance Σ_H

$$\Sigma_H^* = -\frac{2\Omega\eta}{B_e} \tag{B18}$$

on the left side of (2.5). This is the approach taken here. This mathematical device enables us to include the Coriolis effect while avoiding the numerical instability that would result from invoking $\mathbf{v}(t\text{-}\Delta t)$ at time t. (If there is a non-zero physical Hall conductance Σ_H in the ionosphere, the effective contribution (B18) can simply be added to it; in the simulations reported here, the physical Σ_H is set to zero.) The correspondence between the equatorial Coriolis current and the effective ionospheric Hall current can be understood qualitatively by noting that the former is in the direction of $+\mathbf{v}$ while the latter is in the direction of $-\mathbf{v}\cdot\mathrm{Sign}(\Sigma_H)$.

Appendix C: Velocity-dependent part of pick-up current

The fourth term on the right side of (A2) is

$$\delta_{\mathbf{v}}\mathbf{J}_{pu} \equiv \dot{\eta}_s \mathbf{B}_e \times \mathbf{v} / B_e = -\frac{\dot{\eta}_s}{B_e}\nabla_e \Phi \tag{C1}$$

where ∇_e is the gradient operator in the equatorial plane. The symbol $\delta_{\mathbf{v}}$ has been appended to emphasize that this is not the whole pick-up current, just the part of it that depends on **v**. This (partial) current has a divergence

$$\nabla_e \cdot \left(\delta_{\mathbf{v}}\mathbf{J}_{pu}\right) = -\frac{1}{r_e}\left[\frac{\partial}{\partial r_e}\left(r_e \frac{\dot{\eta}_s}{B_e}\frac{\partial \Phi}{\partial r_e}\right) + \frac{1}{r_e}\frac{\partial}{\partial \varphi}\left(\frac{\dot{\eta}_s}{B_e}\frac{\partial \Phi}{\partial \varphi}\right)\right] \tag{C2}$$

Using (B7) we can transform this equation to Euler coordinates (α, β):

$$\nabla_e \cdot \left(\delta_{\mathbf{v}}\mathbf{J}_{pu}\right) = -B_e\left[\frac{\partial}{\partial \alpha}\left(\frac{\dot{\eta}_s}{B_e}\alpha\frac{\partial \Phi}{\partial \alpha}\right) + \frac{\partial}{\partial \beta}\left(\frac{\dot{\eta}_s}{B_e}\frac{1}{\alpha}\frac{\partial \Phi}{\partial \beta}\right)\right] \tag{C3}$$

As argued above between (B8) and (B10), this divergence requires a radial component of the Birkeland current density contribution just above the northern ionosphere

$$\delta_{pu.\mathbf{v}} j_{\|ir} = \frac{B_{ir}}{B_e} \delta_{pu.\mathbf{v}} j_{\|e} = -B_{ir} \left[\frac{\partial}{\partial \alpha} \left(\frac{\dot{\eta}_s}{B_e} \alpha \frac{\partial \Phi}{\partial \alpha} \right) + \frac{\partial}{\partial \beta} \left(\frac{\dot{\eta}_s}{B_e} \frac{1}{\alpha} \frac{\partial \Phi}{\partial \beta} \right) \right]$$

(C4)

In Saturn's ionosphere ($r = R_S$), a field-line-integrated Pedersen conductance $\Sigma_P = \int \sigma_P ds$ produces a height-integrated current density

$$\mathbf{J}_P = \ddot{\Sigma}_{\mathrm{P}} \cdot \mathbf{E} = -\ddot{\Sigma}_{\mathrm{P}} \cdot \nabla_i \Phi \qquad \text{(C5)}$$

[*Wolf et al.*, 2006], where ∇_i is defined in (B12) above and

$$\ddot{\Sigma}_{\mathrm{P}} = \begin{pmatrix} \Sigma_{P\theta\theta} & 0 \\ 0 & \Sigma_{P\varphi\varphi} \end{pmatrix} = \begin{pmatrix} \Sigma_P / \sin I & 0 \\ 0 & \Sigma_P \sin I \end{pmatrix} \qquad \text{(C6)}$$

where I is the field-line inclination angle at $r = R_S$:

$$\sin I \equiv |B_r|/B = \frac{\cos\theta}{\sqrt{1-\frac{3}{4}\sin^2\theta}} = \sqrt{\frac{1-1/L}{1-3/4L}} \tag{C7}$$

for the aligned dipole field used here. (C6) assumes that sin$I$ is approximately constant through the conducting portion of the field line, which is certainly valid for field lines having $L \geq 2$. The divergence of the Pedersen current (C5) is

$$\begin{aligned} \nabla \cdot \mathbf{J}_P &= \frac{1}{R_S \sin\theta}\left[\frac{\partial}{\partial\theta}\left(J_{P\theta}\sin\theta\right) + \frac{\partial J_{P\varphi}}{\partial\varphi}\right] \\ &= -\frac{1}{R_S{}^2 \sin\theta}\left[\frac{\partial}{\partial\theta}\left(\frac{\Sigma_P}{\sin I}\sin\theta\frac{\partial\Phi}{\partial\theta}\right) + \frac{1}{\sin\theta}\frac{\partial}{\partial\varphi}\left(\Sigma_P \sin I\frac{\partial\Phi}{\partial\varphi}\right)\right] \end{aligned} \tag{C8}$$

(C8) assumes that sinθ is approximately constant through the conducting portion of the field line, which is again certainly valid for field lines having $L \geq 2$. Using (B14) we can transform (C8) to Euler coordinates:

$$\nabla \cdot \mathbf{J}_P = -B_{ir}\left[\frac{\partial}{\partial\alpha}\left(2\alpha\frac{\Sigma_P}{\sin I}\cos\theta\frac{\partial\Phi}{\partial\alpha}\right) + \frac{\partial}{\partial\beta}\left(\frac{\Sigma_P \sin I}{2\alpha\cos\theta}\frac{\partial\Phi}{\partial\beta}\right)\right] \tag{C9}$$

As in (B16) above, a positive divergence of the Pedersen current requires a negative (downward) Birkeland current density entering the northern ionosphere:

$$\delta_P j_{\parallel ir} \;=\; -\nabla\cdot\mathbf{J}_P \;=\; B_{ir}\left|\frac{\partial}{\partial\alpha}\left(2\alpha\frac{\Sigma_P}{\sin I}\cos\theta\frac{\partial\Phi}{\partial\alpha}\right)+\;\frac{\partial}{\partial\beta}\left(\frac{\Sigma_P\sin I}{2\alpha\cos\theta}\frac{\partial\Phi}{\partial\beta}\right)\right| \qquad \text{(C10)}$$

Comparing (C4) and (C10) we see that the effect of including the velocity-dependent term of the pick-up current on the right side of (2.1) in the text is mathematically equivalent to omitting that term but instead adding an effective contribution

$$\vec{\Sigma}_P^{\,*}=\begin{pmatrix}\Sigma^*_{\alpha\alpha} & \Sigma^*_{\alpha\beta}\\ \Sigma^*_{\beta\alpha} & \Sigma^*_{\beta\beta}\end{pmatrix}=\begin{pmatrix}\Sigma^*_{\theta\theta} & \Sigma^*_{\theta\varphi}\\ \Sigma^*_{\varphi\theta} & \Sigma^*_{\varphi\varphi}\end{pmatrix}=\frac{\dot{\eta}_s}{B_e}\begin{pmatrix}\dfrac{\sin I}{2\cos\theta} & 0\\ 0 & \dfrac{2\cos\theta}{\sin I}\end{pmatrix} \qquad \text{(C11)}$$

to the physical Pedersen conductance Σ_P of the ionosphere on the left side of (2.5). This is the approach taken here, to avoid the numerical instability that would result from invoking $\mathbf{v}(t\text{-}\Delta t)$ at time t. Note that the $\alpha\alpha$ (or $\theta\theta$) contribution is smaller in magnitude than the $\beta\beta$ (or $\varphi\varphi$) contribution since $2\cos\theta/\sin I > 1$ in the high-latitude region of interest. The correspondence between the velocity-dependent part of the magnetospheric

pick-up current and the effective ionospheric Pedersen current can be understood qualitatively by noting that both are in the direction of **E**.

Appendix D: Justification of equation (B11)

Let J_β be the ionospheric conduction current per unit α crossing a β = constant surface, where α, β are the Euler coordinates defined in (B6). By geometry, it is given by

$$J_\beta = \int \left[\frac{\mathbf{j} \cdot \nabla \beta}{|\nabla \beta|} \frac{1}{|\nabla \alpha| \sin(\alpha, \beta)} \right] ds = \int \left[\frac{\mathbf{j} \cdot \nabla \beta}{B} \right] ds \tag{D1}$$

where **j** is the physical current density (amps/m^2), ds is the element of length along **B**, and the integral is along the portion of the field line that traverses the conducting layer of the ionosphere. The factor sin(α, β) is the sine of the angle between $\nabla\alpha$ and $\nabla\beta$; it is ≡ 1 for the dipole field described by (B6). Similarly, we can write

$$J_\alpha = \int \frac{\mathbf{j} \cdot \nabla \alpha}{B} ds \tag{D2}$$

Wolf et al. [2006] derive full expressions for J_α and J_β including both Hall and Pedersen currents and wind-driven terms. Equation (13) of that paper implies that

$$\mathbf{j}_H \cdot \nabla \alpha = B \sigma_H \frac{\partial \Phi}{\partial \beta}, \; \mathbf{j}_H \cdot \nabla \beta = -B \sigma_H \frac{\partial \Phi}{\partial \alpha} \tag{D3}$$

where $\mathbf{j}_H$ is the Hall current density and σ_H is the Hall conductivity (S/m) of the ionosphere. Substituting (D3) in (D1) and (D2) gives

$$J_{H\alpha} = \frac{\partial \Phi}{\partial \beta} \int \sigma_H ds,\; J_{H\beta} = -\frac{\partial \Phi}{\partial \alpha} \int \sigma_H ds \tag{D4}$$

where $J_{H\alpha}$ and $J_{H\beta}$ are defined as Hall currents in the $\nabla\alpha$ direction per unit β and in the $\nabla\beta$ direction per unit α, respectively.

Define a spherical reference surface just below the conducting regions of the ionosphere, and define surface currents on this reference sphere that carry the same current between flux tubes as the real 3D conduction current does. The surface current density (amp/m), as computed by the RCM-S, is given by

$$\mathbf{J}_H = J_{H\alpha} \frac{1}{r \sin\theta} \left(\frac{\partial \beta}{\partial \phi} \right) \hat{\theta} + J_{H\beta} \frac{1}{r} \left(\frac{\partial \alpha}{\partial \theta} \right)_r \hat{\phi} \tag{D5}$$

Substituting (D4) in (D5) gives

$$\mathbf{J}_H = \left(\int \sigma_H ds \right) \left[\frac{\partial \Phi}{\partial \beta} \frac{1}{r \sin\theta} \frac{\partial \beta}{\partial \phi} \hat{\theta} - \frac{\partial \Phi}{\partial \alpha} \frac{1}{r} \frac{\partial \alpha}{\partial \theta} \hat{\phi} \right] = \left(\int \sigma_H ds \right) \left[\frac{\partial \Phi}{\partial \phi} \frac{1}{r \sin\theta} \hat{\theta} - \frac{\partial \Phi}{\partial \theta} \frac{1}{r} \hat{\phi} \right] \tag{D6}$$

which can be rewritten as

$$\mathbf{J}_H = \left(\int \sigma_H ds \right) \nabla_i \Phi \times \hat{\mathbf{r}} \tag{D7}$$

Equation (D7) is the same as equation (B11) if we define

$$\Sigma_H = \int \sigma_H ds \tag{D8}$$